

THE POTENTIAL OF DUST
POLARIZATION MEASUREMENTS:
ON THE OBSERVABILITY OF MAGNETIC
FIELD STRUCTURES IN STAR-FORMING
REGIONS

Dissertation

zur Erlangung des Doktorgrades
der Mathematisch-Naturwissenschaftlichen Fakultät
der Christian-Albrechts-Universität zu Kiel

vorgelegt von

Stefan Reißl

Kiel, Januar 2016

THE POTENTIAL OF DUST
POLARIZATION MEASUREMENTS:
ON THE OBSERVABILITY OF MAGNETIC
FIELD STRUCTURES IN STAR-FORMING
REGIONS

Dissertation

zur Erlangung des Doktorgrades
der Mathematisch-Naturwissenschaftlichen Fakultät
der Christian-Albrechts-Universität zu Kiel

vorgelegt von

Stefan Reißl

Kiel, Januar 2016

Referent: Prof. Dr. Sebastian Wolf

Koreferent: Prof. Dr. Robert F. Wimmer-Schweingruber

Datum der mündlichen Prfung: 22. März 2016

Abstract

This work aims to evaluate the potential of continuum polarization measurements to determine the underlying magnetic field morphology involved in different stages of the star formation process.

Magnetic fields are crucial for the formation and evolution of stars and planets. In addition, dust grains play also a central role from the thermodynamics of collapsing molecular clouds to the polarization of light. Dust grains partially align with the direction of the magnetic field. As a result, previously depolarized light will gain polarization perpendicular and parallel, respectively, to the magnetic field lines. This makes multi-wavelength polarization measurements on multiple scales a promising tool to complete our picture about the fundamental physics of the star formation process. Revealing the underlying magnetic field morphology with the help of polarization measurements requires continuum dust radiative transfer calculations in arbitrary 3D geometries taking the impact of partially aligned dust grains into account. In this thesis, we follow the approach to post-process complex magnetic field, temperature, and density distributions as well as velocity fields resulting from analytical models and MHD simulations of collapsing molecular clouds to create synthetic polarization maps.

To constrain the role of magnetic fields during star formation we newly developed the 3D radiative transfer code *POLARIS* suitable for dust heating and multi-wavelength polarization simulations. The code solves the radiative transfer problem combined with the polarization effects of dichroic extinction, thermal re-emission, and scattering acting on stellar light and background radiation.

The physical principles accounting for dust grain alignment are still a matter of debate. To predict the impact of imperfectly aligned dust grains on polarization measurements we combine radiative transfer and polarization algorithms with state of the art dust grain alignment theories. The optical properties of the dust materials are pre-calculated by approximating the shape of the dust grains with a distinct number of dipoles on the basis of the laboratory data of astro-silicate and graphite.

This approach allows to constrain the impact of grain alignment on the resulting polarization pattern and, subsequently, to determine the magnetic field morphology. We apply the *POLARIS* code to models of different stages of star formation. We start with a spher-

rical density model in combination with an analytically modeled magnetic field and focus on the question, if projection effects and low inclination angles allow to distinguish between different field morphologies. Then, we determine the potential of polarization measurements to trace the magnetic field morphology in circumstellar disks. Here, we compare theoretical predictions and observational data with synthetic polarization maps. Later, we create polarization maps emerging from a cloud model and analyze the unique patterns associated with different grain alignment theories. Finally, we post-process a MHD collapse simulation. Here, we are following the question about the potential of multi-wavelength polarization measurements to probe distinct characteristic parts of a larger connected magnetic field structure.

Zusammenfassung

Magnetische Felder stellen einen entscheidenden Einfluss in verschiedenen Stadien der Sternentstehung dar. Die genaue Bedeutung magnetischer Felder konnte jedoch noch nicht abschließend geklärt werden. Der wichtigste Grund hierfür ist, dass sich diese Felder der direkten Beobachtung entziehen. Informationen über die Feldstärke und die Morphologie der Feldlinien können nur auf indirekte Weise durch die Beobachtung von polarisiertem Licht gewonnen werden.

Jedoch kann über den Staub die magnetische Feldmorphologie beobachtet werden. Dabei wird angenommen, dass sich rotierende, nicht sphärische Staubteilchen entlang des magnetischen Feldes ausrichten. Diese ausgerichteten Staubteilchen führen nun zu einer Polarisation des beobachtbaren Lichtes. Durch Polarisationsmessungen lassen sich daher Rückschlüsse auf die Magnetfeldmorphologie ziehen. Die Interpretation von Beobachtungsdaten wird allerdings dadurch erschwert, dass eine umfassende Theorie der Staubkornausrichtung gegenwärtig noch nicht verfügbar ist.

Die Zielsetzung dieser Doktorarbeit ist es nun das Potential von Kontinuumpolarisationsmessungen zur Bestimmung der Magnetfeldmorphologie in Sternentstehungsgebieten zu evaluieren. Der Ansatz hierbei ist das Erzeugen von künstlichen Intensitäts- und Polarisationskarten mit Hilfe von Strahlungstransportsimulationen ausgehend von Modellen. Diese Modelle entsprechen astrophysikalischen Systemen in verschiedenen Stadien der Sternentstehung und resultieren sowohl aus analytischen Modellierungen als auch aus selbstkonsistenten magneto-hydrodynamischen Simulationen.

Die Herausforderung bei diesem Ansatz stellt die Lösung der Strahlungstransportgleichung unter Berücksichtigung verschiedener Polarisations- und Staubkornausrichtungsmechanismen dar. Diesem Problem wird durch Zuhilfenahme der Monte-Carlo Methode, einem numerischen Verfahren basierend auf Zufallszahlen und Wahrscheinlichkeitsverteilungen, begegnet. Implementiert wurde dieses Verfahren in einem eigens für diese Arbeit entwickelten Computerprogramm *POLARIS*. Strahlungstransportsimulationen können dadurch unter Berücksichtigung der Heizprozesse und der Polarisationsmechanismen, die mit ausgerichteten Staubteilchen einhergehen, in den komplexen, räumlichen Dichte- und Magnetfeldverteilungen durchgeführt werden. Außerdem gehen in diese Simulationen auch die optischen Eigenschaften von Staubteilchen, wie sie

im interstellaren Medium vermutet werden, mit ein. Zusätzlich werden in den Strahlungstransportsimulationen die aktuellen Theorien der Staubkornausrichtung, wie der Ausrichtung durch Gasströme, der Ausrichtung durch anisotrope Strahlung sowie der Ausrichtung durch paramagnetische Dissipation, separat berücksichtigt.

Eine der grundlegenden Fragen ist, wie sich Projektionseffekte auf die Beobachtbarkeit komplexer, räumlicher Felder auswirken. In dieser Arbeit wird deshalb mit Studien von magnetischen Feldern in analytischen und sphärischen Dichteverteilungen begonnen. Die Staubtemperatur wird dabei unter Berücksichtigung des interstellaren Strahlungsfeldes errechnet. Auf diese Weise werden die Bedingungen für die Beobachtbarkeit und die eindeutige Unterscheidbarkeit für verschiedene magnetische Feldstrukturen ermittelt.

Theoretische Vorhersagen und Beobachtungen widersprechen sich nun darin, ob von circumstellaren Scheiben ein detektierbares Polarisationsignal ausgeht. Die Studien werden daher mit einer analytischen Modellierung von circumstellaren Scheiben fortgesetzt. Hierbei wird untersucht, ob die Staubkornausrichtung durch anisotrope Strahlung in solch einer Umgebung effizient ist und ob sich durch ausgerichtete Staubteilchen die magnetische Feldstruktur in diesen Scheiben eindeutig bestimmen lässt.

Die Frage nach dem dominanten Ausrichtungsmechanismus von Staubteilchen konnte bisher noch nicht abschließend geklärt werden. Aus diesem Grund werden Polarisationskarten einer Molekülwolke erstellt, um die Einflüsse verschiedener Ausrichtungstheorien separat zu untersuchen. Die Analyse der simulierten Polarisationskarten erlaubt die Eigenheiten einer jeden Ausrichtungstheorie zu identifizieren und zu unterscheiden. Abschließend wird das Potential von Multiwellenlängen-Polarisationsmessungen ermittelt, inwiefern sich diese eignen, spezifische Teile einer größeren Magnetfeldstruktur getrennt zu identifizieren. Als Ausgangspunkte für diese Strahlungstransportsimulationen werden hierbei komplexe räumliche Dichte-, Temperatur- und Magnetfeldstrukturen einer magneto-hydrodynamischen Kollaps-Simulation mit verwendet. In dieser Kollaps-Simulation haben sich einerseits zwei Ausflüsse mit eingebettetem toroidal gewundenen Magnetfeld und andererseits sechs Sterne gebildet. Mit den daraus resultierenden Polarisationskarten wird konkret der Frage nachgegangen, unter welchen Bedingungen sich die toroidale Feldkomponente in den Ausflüssen getrennt von dem umgebenden Medium identifizieren lässt. Die Beobachtbarkeit der Magnetfeldstruktur erfolgt dabei wellenlängenabhängig unter der Berücksichtigung der verschiedenen Ausrichtungsmechanismen, der Inklination der Ausflüsse und den verschiedenen Staubparametern.

Table of Contents

Abstract	vii
Zusammenfassung	ix
Contents	xi
List of Figures	xv
List of Tables	xxi
1 Introduction	1
1.1 Why dust?	2
1.2 The problem of partially aligned dust grains	2
1.3 The potential of synthetic polarization maps	4
2 Radiative transfer (RT): Basic concepts and numerical solutions	7
2.1 Theory of radiative transfer	7
2.1.1 The radiative transfer problem	7
2.1.2 Local Thermodynamic Equilibrium (LTE)	9
2.1.3 The Stokes Vector	10
2.2 The Monte-Carlo Method (MC)	11
2.2.1 Error estimation of MC simulations	12
2.2.2 Sampling of optical depth	12
2.2.3 The radiation field	13
2.2.4 Scattering on spherical particles	14
2.2.4.1 Isotropic scattering	16
2.2.4.2 Anisotropic scattering	16
2.2.5 Dust grain heating	17
2.2.5.1 Immediate re-emission method	17
2.2.5.2 Continuous absorption technique	18

2.3	The discrete dipole approximation (DDA)	19
3	The alignment of dust in the ISM	23
3.1	The interstellar medium (ISM)	23
3.2	The interstellar radiation field (ISRF)	24
3.3	Interstellar dust	25
3.3.1	Mechanisms of dust grain alignment	26
3.3.1.1	The Davis Greenstein (DG) effect	26
3.3.1.2	The Barnett effect	28
3.3.2	Dust grain alignment theories	29
3.3.2.1	Imperfect Davis Greenstein (IDG) alignment	29
3.3.2.2	Magneto-mechanical (GOLD) alignment	32
3.3.2.3	Imperfect internal alignment (II)	34
3.3.2.4	Radiative torque (RAT) alignment	35
3.4	Discussion	38
4	The <i>POLARIS</i> MC RT code	41
4.1	Major features and specifications	41
4.2	The octree grid	42
4.3	Radiation emitting sources	44
4.4	Optimization techniques	46
4.4.1	The modified random walk (MRW)	47
4.4.2	Forced first scattering	48
4.4.3	Ray-tracing	48
4.4.4	Peel-off technique	49
4.4.5	Wavelength range selection	49
4.5	Radiative transfer with non-spherical dust grains	50
4.5.1	RT equation for polarization	50
4.5.2	Grain alignment: Analytical solutions and approximations	54
4.5.2.1	Analytical solution of II alignment	55
4.5.2.2	Analytical solution of IDG alignment	57
4.5.2.3	Analytical solution of GOLD alignment	58
4.5.2.4	Approximation of RAT alignment	59
4.5.3	Combined effects of dust grain alignment	60
4.5.4	Limitations on magnetic field strength and velocity stream	61
4.5.5	Scattering on partially aligned dust grains	62
4.5.6	Radiative heating of non-spherical dust grains	64
4.6	Dust grain database	65

5	Synthetic polarization maps of star-forming regions	69
5.1	Benchmark and test setups	69
5.1.1	Offset dust heating	69
5.1.2	Choice of grain alignment and scattering phase function	71
5.1.3	Comparison between the MC RT codes <i>MC3D</i> and <i>POLARIS</i>	73
5.2	Analytical models	76
5.2.1	Bok globules	76
5.2.1.1	The model setup	76
5.2.1.2	Results	80
5.2.1.3	Discussion	84
5.2.2	Circumstellar disks	87
5.2.2.1	Model setup	87
5.2.2.2	Results	88
5.2.2.3	Discussion	91
5.2.3	Cloud model	92
5.2.3.1	Model setup	92
5.2.3.2	Results	93
5.2.3.3	Discussion	96
5.3	MHD outflow simulation	100
5.3.1	Post-processing of the MHD outflow data	102
5.3.2	The choice of dust grain alignment theory	103
5.3.2.1	Polarization pattern resulting from GOLD alignment	103
5.3.2.2	Polarization pattern resulting from RAT and IDG alignment	104
5.3.2.3	Polarization calculations with combined grain alignment	105
5.3.2.4	Comparison	105
5.3.2.5	Impact of inclination angle	107
5.3.2.6	Line of sight analysis	110
5.3.2.7	Grain size dependency	113
5.3.2.8	Discussion	115
6	Conclusive remarks	117
6.1	Summary and Conclusions	117
6.2	Outlook	120
	Bibliography	136
	Acknowledgments	137

List of Figures

2.1	<i>Representation of the same electric field vector in three different coordinate systems.</i> Here, the quantity χ is the orientation angle as observed on the plane of the sky.	10
2.2	<i>Geometrical configuration of scattering on spherical particles.</i> The scattered light is redirected along the scattering plane by an angle of ψ . In order to apply the Müller matrix $\hat{M}(\psi)$, the target coordinate system $(\vec{p}, \vec{s}, \vec{r})$ has to be transformed in the lab coordinate system $(\vec{v}, \vec{h}, \vec{r})$ along the angle α	14
3.1	<i>Spectral intensity distribution of the local ISRF.</i> The plotted data was adapted from Moskalenko <i>et al.</i> (2006) and extrapolated.	25
3.2	<i>Schematic illustration of the Davis Greenstein effect.</i>	26
3.3	<i>Schematic illustration of the Barnett effect.</i> The cube indicates a subsystem within the rotating dust grain and the horizontal line is a segment of the subsystem's orbit.	28
3.4	<i>Schematic illustration of dust grain alignment according to Magneto-mechanical (GOLD) theory.</i> The vectors \mathbf{e}_x , \mathbf{e}_y , and \mathbf{e}_z represent the external reference frame where as the vectors \mathbf{a}_x , \mathbf{a}_y , and \mathbf{a}_z represent the reference frame with respect to the minor axis and the major axis, respectively.	32
3.5	<i>Left panel: Schematic illustration of dust grain alignment according to RAT theory.</i> The vectors \mathbf{e}_x , \mathbf{e}_y , and \mathbf{e}_z represent the external reference frame where as the vectors \mathbf{a}_x , \mathbf{a}_y , and \mathbf{a}_z represent the reference frame with respect to the minor axis and the major axis, respectively. <i>Right panel: Exemplary trajectory map with data adapted from Hoang & Lazarian (2007).</i> Dust grains settle over time either on the high-J attractor point A with parallel alignment or at the low-J attractor point B with anti-parallel alignment with respect to the magnetic field direction.	37

4.1	<i>Left panel: Exemplary color coded density distribution of the center plane of a MHD shock simulation in arbitrary units. The grid refinement was performed according to both criteria presented in Sect. 4.2. As a result of refinement the ratio of remaining cells to maximal possible cells is $\approx 1/200$. Right panel: Schematic illustration of light ray propagation through the octree. The neighboring cell can most efficiently be found with an pointer running up and down through the grid levels.</i>	43
4.2	<i>PDF of re-emitted wavelengths for different dust grain temperatures. The PDF was calculated according to 2.33 and the dust grain model as presented in Sect. 4.6 with astro-silicate as material and a maximal dust grain size of $a_{\max} = 250$ nm.</i>	46
4.3	<i>Geometrical configuration of the dust grains for the case of perfect alignment. The angle φ is defined by \mathbf{B}_p the projection of \mathbf{B} into the Q coordinate system of the Stokes vector and the inclination angle ϑ is made by the direction of propagation \mathbf{k} and the plane of rotation perpendicular to \mathbf{B}.</i>	50
4.4	<i>Left panel: First order moment of the imperfect internal alignment angle ζ as a function of dust temperature T_d to gas temperature T_g. The numerical solution is the black line while the $\gamma = 1$ - approximation is marked with blue crosses. Right panel: Rayleigh reduction factor R_{II} of the internal alignment over the substituted parameter η for different aspect ratios.</i>	56
4.5	<i>Rayleigh reduction factor R_{IDG} of IDG alignment over a normalized dust grain size distribution for oblate grains with different upper thresholds δ_0.</i>	57
4.6	<i>Rayleigh reduction factor R_{GOLD} of GOLD alignment over angle α between predominant direction of the gas stream and the magnetic field direction for oblate grains with different aspect ratios. The angle $\alpha \approx 54^\circ$ of totally randomized dust grains is independent of aspect ratio.</i>	58
4.7	<i>Rayleigh reduction factor R_{RAT} of RAT alignment over a dust grain size distribution normalized over the critical size a_{alg} for oblate grains. Since the quantity $f_{\text{high-J}}$ remains a free parameter the R_{RAT} can be fine tuned to be in the gray area.</i>	59
4.8	<i>Plots of the scattering matrix component M_{11} of an oblate averaged sized wobbling dust grain ($a \in [5 \text{ nm} - 250 \text{ nm}]$) as a function of incident angle ϑ corresponding to two different Rayleigh reduction factors ($R = 0.9$ in red lines and $R = 0.5$ in blue lines). Scattering is in forward direction ($\vartheta' = 0^\circ$, $\varphi' = 0^\circ$). Dotted lines are approximated by Eq. 4.46. The M_{11} component of a randomly orientated dust grain is shown in dark yellow. Solid lines are exact solutions integrated over the IDG cone angle distribution with Eq. 4.48.</i>	62
4.9	<i>Resulting cross sections over wavelength weighted for a size distribution $n(a)$ from $a_{\max} = 5 \text{ nm}$ to $a_{\max} = 0.25 \mu\text{m}$ (left panels) and $a_{\max} = 0.200 \mu\text{m}$ (right panels), respectively.</i>	66

4.10	<i>Resulting alignment efficiencies according to RAT theory over the ratio of wavelength to grain size for astro-silicate (right panel) and graphite (left panel), respectively, as material. The red line shows the fitted model for large dust grains.</i>	67
5.1	<i>Dust temperature distribution in the mid-planes of a MHD collapse simulation. Rows show the results of the same results, but rotated by 90°. In the left column the dust was heated by a MC RT simulation alone. The middle column shows the dust temperature distribution as a result of shock heating in the MHD simulation. The dust temperature combined by offset dust heating as described in Sect. 4.5.6 is shown in the right column. The length of 1400 AU is for scale. We applied an upper cut-off of 400 K to the colorbar for better illustration.</i>	70
5.2	<i>Color coded dust temperature distributions in the mid-plane of an artificial test scenario. The distributions were calculated with the HG phase function overlaid with the contour lines of the dust temperature considering spherical dust grains (left panel) and contour lines for partially aligned oblate dust grains with a Rayleigh reduction factor of $R = 0.5$ (right panel). Contour levels are at $0.1 T_{d,max}$, $0.2 T_{d,max}$, $0.4 T_{d,max}$, and $0.6 T_{d,max}$ calculated with isotropic scattering (solid white line), the HG phase function (solid cyan line), and Mie scattering (dotted yellow line) around a central star.</i>	72
5.3	<i>Resulting dust temperature T_d for the D03 disk model (see Tab. 5.3). The outer left panel shows the temperature distribution in a plane perpendicular to the mid-plane of the disk. The plots show the temperature along the edge of the disk perpendicular to the mid-plane (left) along the mid-plane of the disk (middle) and the distribution along the disks surface (right). The red lines show the results from the MC3D code, the blue ones the results from the POLARIS code, and the gray lines show the error between both codes.</i>	73
5.4	<i>Resulting distribution of the polarized flux F_p for the D03 disk model (see Tab. 5.3). The outer left panel shows the polarized flux distribution as a result of scattered stellar radiation under an inclination angle of $i = 45^\circ$ and a wavelength of $\lambda = 730$ nm. The plots show the polarized flux through the center of the disk along the horizontal direction (left) along the vertical direction (middle) and the bisecting line (right). The red lines show the results from the MC3D code, the blue ones the results from the POLARIS code, and the gray lines show the error between both codes.</i>	73
5.5	<i>The same as Fig. 5.4 for the D06 disk model.</i>	74
5.6	<i>The same as Fig. 5.3 for the D06 disk model.</i>	74
5.7	<i>3D plots for the constant (panel a, Eq. 5.2), toroidal (panel b, Eq. 5.4, hourglass (panel c, Eq. 5.3) helical (panel d, Eq. 5.5), dipole (panel e, Eq. 5.6), and quadrupole (panel f, Eq. 5.7) magnetic field morphologies.</i>	77

- 5.8 *Left panel: Dust temperature distribution in the mid-planes of the Bonnor-Ebert sphere density profile. The temperature was calculated with the ISRF as radiation source. Right panel: Resulting pattern of linear polarization. The pattern is overlaid with polarization vectors for the model BE_{const} at a wavelength of $810 \mu\text{m}$ and with an inclination angle of $i = 45^\circ$.* 78
- 5.9 *Linear polarization (top row) and circular polarization (bottom row) of model BE_{toro} with inclination angles of 3° (left column), 45° (middle column) and 87° (right column) at a wavelength of $810 \mu\text{m}$. We added an offset angle of 90° to the vectors of linear polarization to match the projected magnetic field morphology. The dust particles are aligned according to IDG theory.* 80
- 5.10 *Same as Fig. 5.9 for the BE_{hour} model.* 81
- 5.11 *Same as Fig. 5.9 for the BE_{heli} model.* 82
- 5.12 *Same as Fig. 5.9 for the BE_{dip} model.* 83
- 5.13 *Same as Fig. 5.9 for the BE_{quad} model.* 84
- 5.14 *Resulting mean values of optical depth τ (top left panel), normalized linear polarization (top right panel), and normalized circular polarization (bottom left panel) over wavelength for different inclination angles for the model BE_{hour} . The normalized circular polarization of model BE_{heli} is in the bottom right panel.* 85
- 5.15 *Distribution of grain sizes a_{alg} where dust particle start to align to the magnetic field direction \vec{B} according to RAT - theory. The shown plane is perpendicular to the mid-plane of the disks. The disk model D03 with $10^{-3} M_\odot$ is on panel a and the model D05 with $10^{-5} M_\odot$ is on panel b. Lower values of a_{alg} result in higher degree of linear polarization.* 89
- 5.16 *Maps with pattern of linear polarization overlaid with normalized orientation vectors at an exemplary wavelength of $\lambda = 515 \mu\text{m}$. We applied an offset of 90° to the orientation vectors to match the projected toroidal magnetic field morphology. The model D03 with $10^{-3} M_\odot$ is on the left column and model D05 with $10^{-5} M_\odot$ is shown on the right column for inclination angles from $i = 30^\circ$ (top row) to $i = 90^\circ$ (bottom row) in steps of 15° .* 90
- 5.17 *Schematic illustration of the cloud models C01 (left panel) and C02 (middle panel). Both models differ only by the position of a single star. The isocontour surface at $\log(n_d) = 3.27 \text{ m}^{-3}$ is in dark yellow. The direction of the common gas stream \vec{v} (right panel) towards the center is in green lines and the analytical hourglass field morphology is shown in grey. Red lines and blue bars indicate the different angles between radiation field and the magnetic field direction. The letters A – D indicate areas with expected characteristic features for RAT and GOLD alignment, respectively.* 92

5.18	<i>Ratio of polarization cross sections $\log_{10}(C_x/C_p)_{\lambda=723 \mu\text{m}}$ of imperfectly aligned dust grains C_x to perfectly aligned dust grains C_p in the mid-plane of the model space for the C01 model (top row) and C02 model (bottom row). The x stands for IDG alignment (left columns), RAT alignment (middle columns), and GOLD alignment (right columns). In the middle columns dotted white lines indicate the regions where the alignment efficiency $Q_{\Gamma}(\varepsilon)$ is at its minimum. The dotted red lines in the right columns show the transition where GOLD alignment does change the sign of linear polarization.</i>	94
5.19	<i>Maps with pattern of linear polarization overlaid with normalized orientation vectors at an exemplary wavelength of $\lambda = 723 \mu\text{m}$. We applied an offset of 90° to the orientation vectors to match the projected hourglass magnetic field morphology. The cloud model C01 is on the left column and the model C02 is on the right column for dust grains aligned with the IDG mechanism (top row), RAT mechanism (middle row), and GOLD mechanism (bottom row).</i>	98
5.20	<i>Plots of the degree of linear polarization of the C01 model (top row) and C02 model (bottom row) as a function of normalized intensity ($P - I$ relation). The results with IDG alignment (left column), RAT alignment (middle column), and GOLD alignment (right column). Blue crosses represent the original models C01 and C02 where as red crosses are the models rotated by 90°.</i>	99
5.21	<i>Plots of the gas number density (left column) and the adjusted dust temperature (right column) in two planes parallel (top row) and perpendicular (bottom row) to the disk of the MHD outflow simulation.</i>	100
5.22	<i>3D plots of the magnetic field morphology (panel a) and the velocity field (panel b) of the MHD outflow simulation.</i>	102
5.23	<i>Schematic illustration of the expected dust grain (blue ellipses) alignment behavior according to GOLD alignment in the center plane perpendicular (left panel) and parallel (right panel) to the symmetry axis of the outflow lobes (dark blue). The angle α is defined to be between magnetic field direction (dark red) and the velocity field (dark green) of the gas. The contour of the critical value of α_0 where dust grains start to align with their longer axis parallel to the magnetic field is indicated by a red dotted line.</i>	103
5.24	<i>The same as in Fig. 5.23. The angle ε is defined to be between the predominant direction of the radiation (blue lines) and the magnetic field lines (dark red).</i>	104
5.25	<i>Resulting maps of the degree of linear polarization P_l (color coded) overlaid with normalized orientation vectors considering GOLD alignment at four distinct wavelengths λ.</i>	106
5.26	<i>The same as Fig. 5.25 considering IDG alignment.</i>	106
5.27	<i>The same as Fig. 5.25 considering RAT alignment.</i>	106

5.28	<i>The same as Fig. 5.25 considering a combination of all three alignment mechanisms.</i>	106
5.29	<i>Resulting maps of the degree of linear polarization P_l (color coded) overlaid with normalized orientation vectors considering GOLD alignment at a wavelength of $\lambda = 1.3$ mm and three inclination angles i.</i>	108
5.30	<i>The same as Fig. 5.29 considering IDG alignment.</i>	108
5.31	<i>The same as Fig. 5.29 considering RAT alignment.</i>	108
5.32	<i>The same as Fig. 5.29 considering a combination of all three alignment mechanisms.</i>	108
5.33	<i>Physical quantities along the two exemplary line of sights LOS01 and LOS01. The top row shows the normalized values of polarized intensity I_p (blue), dust number density n_d (green), and its first derivative $dn(l)_d/dl$ (dotted black). Note, that the polarized intensity I_p is plotted as a cumulative value. The bottom row shows the orientation angles of linear polarization θ_{pl} (blue), magnetic field θ_B direction (dotted black), and their difference $\Delta\theta$ (green).</i>	110
5.34	<i>Flux map (left panel) overlaid with vectors of linear polarization and map of circular polarization (right panel) of the post-processed MHD outflow simulation. The maps are calculated for a wavelength of $\lambda = 1.3$ mm. Green regions in the flux map indicate a positive detection of the toroidal magnetic field component by the line of sight analysis. The selected line of sights (blue circles) correspond to the plot in Fig.5.33.</i>	111
5.35	<i>Flux maps (color coded) at a wavelength of $\lambda = 1.3$ mm overlaid with vectors of linear polarization considering a combination of all three alignment mechanisms (see Sect. 5.3.2.3) for an inclination angle of $i = 0^\circ$ (top row), $i = 30^\circ$ (middle row), and $i = 60^\circ$ (bottom row) and with maximal dust grain radii of $a_{\max} = 250$ nm (left column), $a_{\max} = 2$ μm (middle column), and $a_{\max} = 200$ μm (right column). The length of the vectors depends on the degree of linear polarization. For the flux an upper cut off of $F_{\max} = -0.5$ [$\log_{10}(Jy/px)$] was applied for better comparison. The contour lines show constant flux from $2F_{\max}$ (green) to $7F_{\max}$ (dark blue) in steps of F_{\max}.</i>	113

List of Tables

- 5.1 *Parameter space of the dust heating study.* The side length of the model is $L = 5000$ AU. 71
- 5.2 *Physical parameters of the Bok globule models.* The characteristic radius for the BonnorEbert sphere is $r_c = 1100$ AU. For the PA alignment not all parameters are required. Parameters irrelevant for the radiative transport calculations are marked with an X. 76
- 5.3 *Parameters of the applied disk models.* We consider different disk masses and refer to the models with a total disk mass of $10^{-3} M_\odot$ as D03, with $10^{-4} M_\odot$ as D04, with $10^{-5} M_\odot$ as D05 and with $10^{-6} M_\odot$ as D06, respectively. 87
- 5.4 *Table of physical parameter for the applied cloud models.* 92

Chapter 1

Introduction

The presence of matter between the stellar systems of our galaxy has been discovered about a century ago. This interstellar medium (ISM) consisting of gas and dust provides a reservoir of materials necessary for the formation of stars. Magnetic fields in the ISM affect astrophysical processes associated with star formation in various environments and scales in a crucial way. However, the exact contributions of magnetic fields to regulate the star formation process is still a topic of ongoing research (Mouschovias & Ciolek, 1999; Elmegreen, 2000; McKee & Ostriker, 2007). Currently, the models of what drives star formation by means of magnetic support (Mouschovias & Ciolek, 1999) or turbulence (Klessen *et al.*, 2004) make different predictions about the resulting magnetic field geometry.

For the magnetically supported model of star formation a characteristic hourglass field is predicted by theory (e.g. Galli & Shu, 1993) and magneto-hydrodynamic simulations (e.g. Banerjee *et al.*, 2006). An originally parallel magnetic field morphology turns into a well ordered hourglass morphology since the tension of the bent magnetic field lines provides support. Self-gravitating clouds have long been believed to reduce support against collapse by magnetic support and triggering star formation (Mouschovias & Ciolek, 1999) with time scales of collapse is up to 10 *Myr* assuming ambipolar diffusion (Falgarone *et al.*, 2008; Girart *et al.*, 2009; Crutcher *et al.*, 2010). This indicates a significant influence of magnetic fields on the star formation process.

The turbulent model, in turn, predicts a magnetic field that is too weak to resist the deformation by the local turbulent ISM environment. In this case, the magnetic field lines have an irregular and chaotic structure. Indeed, this model is supported by observations since molecular clouds seem to be much shorter lived and the cloud collapse is controlled by turbulence with negligible magnetic contribution (Elmegreen, 2000; Klessen *et al.*, 2004).

1.1 Why dust?

Indeed, in the ISM both magnetic fields and turbulence are involved in the star formation process each of them resulting with a characteristic prediction concerning the magnetic field properties. However, to identify the exact contributions of both effects a detailed comparison of observational data and numerical calculations is required. A variety of observational techniques are available to determine the magnetic field strength such as the Chandrasekhar-Fermi method (Chandrasekhar & Fermi, 1953; Crutcher *et al.*, 2004) and Zeeman measurements (e.g. Crutcher *et al.*, 2008). Focusing on the aspect of the magnetic field morphology, this quantity can be inferred by polarization measurements. This method takes advantage of the fact that non-spherical rotating dust grains tend to align with the magnetic field direction inside the ISM (e.g. Girart *et al.*, 1999; Lucas *et al.*, 2004; Tang *et al.*, 2010). Historically, the alignment of non-spherical dust grains was first identified in Hiltner (1949), Hall & Mikesell (1949), and Hall (1949) as a promising explanation for the observed polarization of starlight. Previously depolarized light will be polarized by dichroic extinction in the near-infrared (NIR) and thermal dust re-emission from far-infrared (FIR) to sub-millimeter (sub-mm) wavelengths (e.g. Frau *et al.*, 2011) perpendicular and parallel, respectively, to the magnetic field lines. This makes multi-wavelength observation on multiple scales a powerful tool completing our understanding of the fundamental physics of the star formation processes. However, from an observational point of view, the difficulty is that the reliability of polarization measurements and their interpretation depends on a wide range of physical parameters that are still discussed. So far, the main factors limiting an accurate interpretation of continuum polarization measurements are the current uncertainties concerning dust composition and size distribution as well as an incomplete theory of grain alignment.

1.2 The problem of partially aligned dust grains

Since the discovery of aligned dust grains, progress in the understanding of the fundamental grain alignment physics has been made to develop a consistent theory. Existing theories of grain alignment (see Lazarian, 2007; Andersson, 2015, for review) agree that rotating non-spherical dust grains align with their shorter axis parallel to the magnetic field direction. However, a comprehensive theory of grain alignment is still missing. The available theories of dust grain alignment can be divided into three three major classes.

- i) The classical theory of imperfect Davis-Greenstein (IDG) alignment (Davis & Greenstein, 1951) to account for the alignment of non-spherical dust grains with the magnetic field direction as reference frame is based on the paramagnetic dissipation inside the grain material itself. In IDG alignment random gas-dust col-

lisions are important for the dust grain to be spun up in the first place. However, these collisions also reduce the alignment efficiency. This mechanism provides an explanation for the alignment of small dust grains. As shown by observations (Clayton *et al.*, 1992, 1995; Martin, 2007) the alignment of small dust grains is necessary to account for the polarization of starlight in the ultraviolet (UV) wavelength regime.

- ii) In order to account for the observed polarization a mechanism was originally proposed by purely mechanical means of non-spherical dust grains without the consideration of any magnetic field interactions. In the 1950s the presence of magnetic fields strong enough to orient dust grains in a certain direction and the composition of the dust grains itself were speculative at best. In Gold (1952) it was assumed one can explain the measured dust polarization by mechanical alignment alone. To account for the gas stream in Gold (1952) cloud-cloud collisions in the galaxy are offered as an explanation. This result was put into doubt by Davis (1955) since the supersonic condition between gas and dust could not hold over a distance longer than ≈ 0.1 ly, making dust grain alignment by means of mechanical alignment implausible.

The theory of mechanical grain alignment was later extended by Lazarian (1994, 1995) to incorporate the presence of a magnetic field. The dust grains in this magneto-mechanical alignment theory gains rotational energy by a directed supersonic gas stream. However, the preferential direction of alignment remains the magnetic field line. Magneto-mechanical alignment is grain size independent and might explain the rotation of alignment in supersonic environments as reported in Rao *et al.* (1998). Additionally, supersonic gas streams as a result of Alfenic velocities are larger than the sound velocities over large regions in space for typical conditions in the ISM (Falgarone *et al.*, 1986; Myers, 1987). Hence, mechanical alignment may still account to the overall grain alignment under certain conditions.

- iii) It was first suggested by Dolginov & Mitrofanov (1976a) that irregular shaped dust grains with a helicity might react differently to right and left circular polarized radiation. This effect would induce a radiative torque (RAT) on the dust grain. Since then, the spin up of dust grains by radiative pressure was also supported by laboratory experiments (Abbas *et al.*, 2004). The development of the *DDSCAT* code (Draine & Flatau, 1994) made it possible to calculate numerically the effects of RATs on dust grains with the help of the discrete dipole approximation (DDA) (see Sect. 2.3) method. In Draine & Weingartner (1996, 1997) a first numerical study with irregular dust grains was presented to quantify the parameters of RAT alignment. This preliminary work confirmed the findings of

Dolginov & Mitrofanov (1976a). RATs were shown to be a common phenomenon for irregular grains and the dust grain alignment with respect to the magnetic field was demonstrated. However, the numerical studies suffered from the limited amount of investigated irregular grain shapes and dust grain sizes. The challenge was to find a mathematical description for RAT alignment in view of the complexity of radiation-dust interaction and dust grains with arbitrary and complex shapes. The theoretical frame work for RAT alignment was developed in Hoang & Lazarian (2007) where the numerical finding of Weingartner & Draine (2003) was reproduced with an analytical model. This analytical model (AMO) of RAT alignment handles the dust grain as an oblate spheroids with a mirror attached at certain distance from the grain's surface. The mirror mimics a helicity and scattered radiation can transfer an angular momentum to the oblate dust grain. Despite this enormous simplification the analytical results are in good agreement with that of the numerical simulations performed with the *DDSCAT* code. The RAT alignment could account for the alignment of large dust grains (Kim & Martin, 1995) in regions with a high radiation field (Andersson & Potter, 2010).

Each class of dust grain alignment theory comes with its characteristic effects making synthetic polarization maps highly dependent on the choice of considered grain alignment mechanism. Consequently, the lack of an unifying grain alignment theory is acting as an additional factor of ambiguity in the interpretation of polarization measurements.

In chapter 3 we introduce the parameters of the dust predominant in the ISM. Later in this chapter, we deliver the mathematical framework of the grain alignment theories considered in this thesis.

1.3 The potential of synthetic polarization maps

Furthermore, the expedient comparison between the magnetic field morphology predicted by different models of star formation with observational data requires to link the intrinsic problem of radiative transfer (RT) with the polarization effects of non-spherical dust and the physics of grain alignment. In idealized scenarios, the problem can be solved by using analytical RT techniques (e.g. Ivezić *et al.*, 1997; van Zadelhoff *et al.*, 2002; Steinacker *et al.*, 2006). Environments with ongoing star formation, however, are regions where gas, dust, and magnetic fields form complex structures and their values cover several orders of magnitude. The Monte-Carlo (MC) method is well suited for performing radiative transfer simulations independent of complexity. Here, photon packages are sent along probabilistic pathways to obtain numerical solutions to

RT problems. Despite, the increasing complexity of magneto-hydrodynamic (MHD) simulations, MC RT simulations in turn remain still among the outstanding challenges in computational astrophysics. The recent progress in technology and available computational equipment has become powerful enough to apply the MC RT method to complex astrophysical models with a growing variety of physical effects. For this reason a number of several codes has been developed to cover the distinct problems of astrophysical importance such as heating of dust by stellar radiation, photo ionization, line radiative transfer, and the calculation of polarization because of scattered light (Juvela, 1999; Wolf *et al.*, 1999; Whitney & Wolff, 2002; Niccolini *et al.*, 2001; Ercolano *et al.*, 2003; Wolf, 2003; Steinacker & Henning, 2003; Min *et al.*, 2009; Whitney, 2011; Baes *et al.*, 2011; Dullemond, 2012; Robitaille, 2013; Harries, 2014). Over the years the heating of dust and polarization of scattered light on spherical grains became a standard feature in most MC RT codes. However, despite the great success of RT MC simulations in astrophysics, the aspect of grain alignment has been mostly ignored so far. With instruments like Scuba II (Bastien *et al.*, 2005) and Sharc II (Novak *et al.*, 2004) and the upcoming observational equipment of HAWC+ (Dowell *et al.*, 2013) and ALMA (Brown *et al.*, 2004) the need for accurate and expedient MC RT polarizations simulations is rising. Hence, we developed a new RT code from scratch and fully incorporated radiative transfer, dust heating, and polarization algorithms with state of the art dust grain alignment theories.

In the first part of this thesis, we review the basic concepts of RT and of the MC approach in chapter 2. In chapter 4 we present the newly developed MC RT code *POLARIS*. Here, we combined the concepts introduced in chapter 2 and the physics of interstellar dust grains as presented in chapter 3 with MC optimization techniques. We provide test scenarios to demonstrate the accuracy of the code in chapter 5. In order to investigate the potential of polarization measurements because of grain alignment we start to apply the code to astrophysical models later in chapter 5. Here, we look for observable features of the magnetic field morphology by means of synthetic maps of intensity and polarization dependent on grain alignment theory.

In general, the advantage of synthetic polarization maps is that the spatial distribution of the physical input parameters is known in advance. Careful examination of the resulting synthetic intensity and polarization maps on multiple scales will help to disentangle the contributions of different dust parameters and grain alignment theories. In particular, this will allow to determine the constrains of projection effects and to identify the regions that contribute to the net polarization by means of a careful line of sight analysis. Finally, the evaluation of the potential of multi-wavelength polarization measurements as a tool to determine the magnetic field morphology will furthermore bridge the gap between observation and predictions of numerical simulations.

Chapter 2

Radiative transfer (RT): Basic concepts and numerical solutions

In this chapter we present the RT problem and introduce the related physics essential for this thesis. A number of methods for solving the RT problem have become standard features in RT codes over the years. Here, we present selected numerical features with regard to the propagation of radiation in a general manner. Later, we focus on the heating and polarization of dust grains covered in this thesis. Finally, we discuss a numerical approximation method for calculating the optical properties of non-spherical dust grains in detail.

2.1 Theory of radiative transfer

In the field of astrophysics the objects of interest and their properties are mostly out of reach for direct measurements considering the enormous distances in outer space. Almost all of our knowledge about the universe is based on the observation of electromagnetic radiation. While laboratory experiments and computer simulations are essential to complete our picture of astrophysical phenomena only by imaging and analyzing of radiation we can test our models and theories against reality. This makes observations one of the most important tools in astrophysics. However, the interpretation of observational data requires a detailed understanding of the physics of light emission and the alteration of the radiation within the medium it propagates.

2.1.1 The radiative transfer problem

The theory of radiative transfer provides the equations necessary to describe the change in specific intensity I_λ for a distinct wavelength λ along its path. In the stationary case

the quantity $I_\lambda := I_\lambda(\vec{r}, \vec{k})$ is a function of position \vec{r} and the wave vector $\vec{k} = \frac{2\pi}{\lambda}$ defines the direction of propagation. The amount of energy $d\varepsilon_\lambda$ per wavelength range $\lambda + d\lambda$ passing through an infinitesimal small area dA within a solid angle $d\Omega$ in direction of θ with respect to the surface normal of the area and per time dt the specific intensity is defined to be

$$I_\lambda = \frac{d\varepsilon_\lambda}{\cos(\theta)dAdtd\lambda d\Omega}. \quad (2.1)$$

Along the distance dl the specific intensity is modified by the loss because of extinction while the radiation passes a medium and the contribution of the released energy by the medium. The extinction is characterized by absorption of light and scattering inside the medium itself. In order to take care of the decrease in intensity because of extinction we introduce the sink term $-\kappa_\lambda I_\lambda$ which is proportional to the intensity itself with the extinction coefficient κ_λ and the source term with the emissivity j_λ . In its general form the radiative transfer equation becomes

$$\frac{dI_\lambda}{dl} = -\kappa_\lambda(\vec{r})I_\lambda + j_\lambda(\vec{r}). \quad (2.2)$$

Both coefficients κ_λ and j_λ govern the radiative transfer through a medium on a macroscopic level. The relations to the quantities of distinct particles on the microscopic level are $\kappa = \sum_i n_i C_i(\lambda)$ and $j = \sum_i n_i \varepsilon_i(\lambda)$, where n_i is the number of particles of species i per volume, $C_i(\lambda)$ is the wavelength dependent cross section of extinction and ε is the emission coefficient per particle. The cross section C is defined to be

$$C = \pi a^2 \times Q \quad (2.3)$$

where a is the radius of the particle and Q is a material dependent efficiency factor. Introducing the quantity of the optical depth with

$$\tau_\lambda = \int_0^{l'} \kappa_\lambda(\vec{r}) dl \quad (2.4)$$

allows the formal solution of the radiative transfer equation as

$$\frac{I_\lambda(\vec{r})}{d\tau} = I_\lambda(\vec{r}) - S_\lambda(\vec{r}) \quad (2.5)$$

with

$$S_\lambda(\vec{r}) = \frac{j_\lambda(\vec{r})}{\kappa_\lambda(\vec{r})} \quad (2.6)$$

as the source function. Here the limiting case with $\tau \gg 1$ is defined as optically thick and the case with $\tau \ll 1$ as optically thin. The solution of Eq. 2.5 is straightforward if the source function

$$I_\lambda(\tau') = I_\lambda(0)e^{-\tau'} + \int_0^{\tau'} S_\lambda(\tau)e^{-\tau} d\tau \quad (2.7)$$

is known in advance.

2.1.2 Local Thermodynamic Equilibrium (LTE)

The energy absorbed is usually re-emitted at a different wavelength dependent on the characteristic properties of the medium. When the amount of absorbed energy is in balance with the amount of re-emitted energy the medium is in thermodynamic equilibrium. In this case the re-emission of a medium with temperature T is that of a black body and the source function can analytically be expressed as a characteristic spectral distribution of energy with $S_\lambda = B_\lambda(T)$ where

$$B_\lambda(T) = \frac{2hc^2}{\lambda^5} \frac{1}{\exp(hc/\lambda k_B T) - 1} \quad (2.8)$$

is the Planck function. Using the definition of the source function (see Eq. 2.6) we get for the emissivity per mass

$$j_\lambda(T) = nC_{\text{abs},\lambda} B_\lambda(T). \quad (2.9)$$

However, the assumption of a strict thermodynamic equilibrium is a simplification which cannot hold under more realistic conditions where the temperature is not constant within the system.

The distance light travels between two points of interaction on average inside the medium is defined as the mean free path length. When the radiation interacts very inefficiently with the medium the mean free path length is large and vice versa. The inverse of the coefficient κ_λ^{-1} in the RT equation quantifies the distance a photon travels on average. For sufficiently small values of κ_λ^{-1} the mean free path length becomes very small compared to the temperature gradient. On such small scales the assumption of a thermodynamic equilibrium can locally be assumed and the medium has still a re-emission behavior like a black body. This simplification is referred to as local thermodynamic equilibrium (LTE) and often applied to dense astrophysical systems.(to do ref).

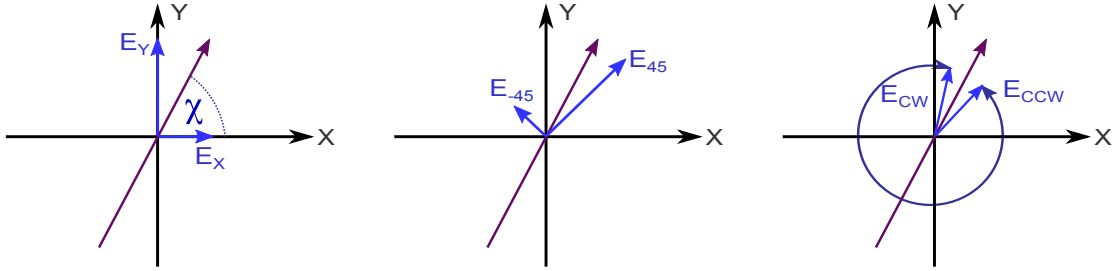


Figure 2.1: Representation of the same electric field vector in three different coordinate systems. Here, the quantity χ is the orientation angle as observed on the plane of the sky.

2.1.3 The Stokes Vector

The polarization state of radiation along its path can be quantified by the 4-component Stokes vector $\vec{S} = (I, Q, U, V)^T$ where the I parameter is the total intensity (see Bohren & Huffman, 1983, for details). Each ensemble of polarized radiation can be decomposed in vector components in different coordinate systems (see Fig. 2.1). The projection of the electric field vector \vec{E} on the axis of a fixed orthonormal coordinate system gives the \vec{E}_x and \vec{E}_y field components. The electric field components \vec{E}_{45} and \vec{E}_{-45} are defined as projections on the axis of a second coordinate system rotated by 45° with respect to the first one. Decomposing \vec{E} in two clockwise and counterclockwise rotating waves gives the components \vec{E}_{cw} and \vec{E}_{ccw} , respectively. With the decomposition of the electromagnetic wave in the different components the Stokes vector is completely defined by

$$\vec{S} = \begin{pmatrix} I \\ Q \\ U \\ V \end{pmatrix} = \begin{pmatrix} |E_x|^2 + |E_y|^2 \\ |E_x|^2 - |E_y|^2 \\ |E_{45}|^2 - |E_{-45}|^2 \\ |E_{cw}|^2 - |E_{ccw}|^2 \end{pmatrix}. \quad (2.10)$$

The parameters Q and U describe the state of linear polarization in vertical and diagonal direction for a given coordinate system. According to the Stokes formalism, linear polarization is determined by the degree of linear polarization P_l with

$$P_l = \frac{I_p}{I} = \frac{\sqrt{U^2 + Q^2}}{I} \quad (2.11)$$

and $0 \leq P_1 \leq 1$ where I_p is the polarized intensity and the position angle χ as observed on the plane of the sky is defined by

$$\tan(2\chi) = \frac{U}{Q}. \quad (2.12)$$

The parameter V describes the degree of circular polarization P_c with

$$P_c = \frac{V}{I} \quad (2.13)$$

and $-1 \leq P_c \leq 1$. Here, $P_c = 1$ stands for circular polarization with the electric field vector rotating clockwise and $P_c = -1$ stands a rotation counter clockwise towards the observer. The definition of the Stokes vector requires the parameters to follow the relation

$$I^2 \geq Q^2 + U^2 + V^2 \quad (2.14)$$

where equality of right hand side and left hand side indicate complete polarization.

2.2 The Monte-Carlo Method (MC)

The MC method (also Monte-Carlo simulation or Monte-Carlo technique) was named after the city in Monaco famous for its gambling. Applications of the MC method range from complex climate model calculations to the interaction of high energetic radiation with the upper atmosphere. Originally considered as too time consuming the MC method has become increasingly popular to tackle the radiative transfer problem numerically within reasonable accuracy and timescales. As is gambling, the MC method is based on chance albeit it is not random but governed by statistical sampling from known probability distributions. Hence, the accuracy of MC simulations rely on an explicit representation of the probability distributions associated with physical processes.

Modeling the propagation of radiation in matter is a high dimensional problem. In most circumstances, the radiative transfer problem can only be solved numerically. The great advantage of the MC method is, that it simulates actual events. In particular, the radiative transfer of polarized radiation can easily be implemented by mimicking nature. Instead of propagating single photons the radiation is represented by a package of photons with identical wavelengths. The astrophysical system of interest is represented by a grid with a number of discrete grid cells. Each cell represents a region of the system with constant physical quantities.

The life cycle of a photon package can be described by the following three steps:

- i) **Emission:** The photon package is emitted by a source in a predefined model space. The source represents an astrophysical object, usually a star. Energy and wavelength of the photon package are statistically sampled from the characteristic spectral emission of the source.
- ii) **Propagation:** The photon package propagates through the grid until the optical depth exceeds a certain critical value. At this point the photon package interacts with the particles in that particular cell, meaning the photon scatters or becomes absorbed. Here, the desired physical quantities such as temperature or polarization state by the photon package are adjusted. This step is repeated until the photon package passes the borders of the grid.
- iii) **Detection:** The photon package leaking from the grid are collected on a detector in order to calculate synthetic maps of intensity and polarization.

2.2.1 Error estimation of MC simulations

In contrast to analytical solutions the MC method remains an approximation and comes with an inherent error which manifests itself as noise in the output data. The level of noise inherent in RT MC simulations can usually be reduced by increasing the number N_{ph} of photon packages. However, a higher amount of photon packages comes with an increase in calculation time. Furthermore, the noise in the resulting output data does not linearly scale with N_{ph} but follows approximately a Poisson distribution (see Bevington, 1969, p. 40). Independent of the applied MC method of photon transfer, this error in MC simulations can be quantified with the standard deviation

$$\sigma \propto \frac{1}{\sqrt{N_{\text{ph}}}}. \quad (2.15)$$

Subsequently, the reduction of noise scales slowly with the number of applied photon packages.

2.2.2 Sampling of optical depth

In the RT MC run each photon package propagates a path length l between two points where particles and the radiation interact. Here, interaction means scattering or absorption and re-emission. The net optical depth τ_{Σ} of a photon package can be calculated by adding up the contributions of each cell

$$\tau_{\Sigma} = \sum_i C_{\text{ext},i} n_{\text{d},i} l_{\text{d},i} \quad (2.16)$$

where $C_{\text{ext},i}$, $n_{d,i}$, and $l_{d,i}$ are the cross section of extinction, the dust number density, and the path length passed in each cell, respectively. The optical depth and, subsequently, the path length l follows a probabilistic distribution. The maximal optical depth τ_{max} up to the next point of interactions can be sampled from (see Wolf, 2003, for details)

$$\tau_{\text{max}} = -\ln(1-z). \quad (2.17)$$

Finally, the next point of interaction is determined by the criterion $\tau_{\Sigma} \geq \tau_{\text{max}}$.

2.2.3 The radiation field

A common problem in RT MC simulations relates to the calculation method used for the local radiation field. The calculation of many physical quantities (especially dust temperature and grain alignment efficiency) by a MC simulation have their basis in a detailed knowledge of the local radiation field. Commonly the radiation field is calculated by the local estimation method (Lucy, 1999) by absorbing not just at the next point of interaction, but also along the path each photon package passed along. Photons travel through a distinct cell with volume V up to the next cell wall or the next point of interaction. In LTE the radiation loses energy because of absorption but the same amount of energy is re-emitted at longer wavelengths. Since we control the number $N_{1,2}$ of photons in each packet we can calculate with a constant energy ϵ_0 before (1) and after (2) absorption and re-emission independent of wavelength with $N_1 \frac{hc}{\lambda_1} = N_2 \frac{hc}{\lambda_2}$. The quantity that connects the energy of the photon packages ϵ_0 to the specific radiation field is the mean intensity

$$J_{\lambda} = \frac{1}{4\pi} \int_{\Omega} I_{\lambda} \vec{n} d\omega \quad (2.18)$$

where Ω is the solid angle in steradians and \vec{n} is the direction of propagation of the light ray with specific intensity I_{λ} . By incorporating the energy of the photon packages as it is defined in Eq. 2.1, the mean intensity can be rewritten as a sum of N_{ph} photon packages

$$J_{\lambda} = \frac{\epsilon_0}{4\pi\Delta t} \sum_{n=1}^{N_{\text{ph}}} \frac{1}{|\cos(\theta_i)| dA d\lambda} \quad (2.19)$$

passing a certain region of space. An alternative interpretation of the mean intensity is that it represents the energy per time deposited by each photon packet in a region with distinct volume V . This allows to calculate the mean intensity J integrated over wavelength by means of accumulation of all N_{ph} path lengths l of passed photons with

$$J = \frac{\epsilon_0}{4\pi V \Delta t} \sum_{n=1}^{N_{\text{ph}}} l. \quad (2.20)$$

The mean intensity J is the essential parameter for subsequent dust temperature and grain alignment efficiency calculations.

2.2.4 Scattering on spherical particles

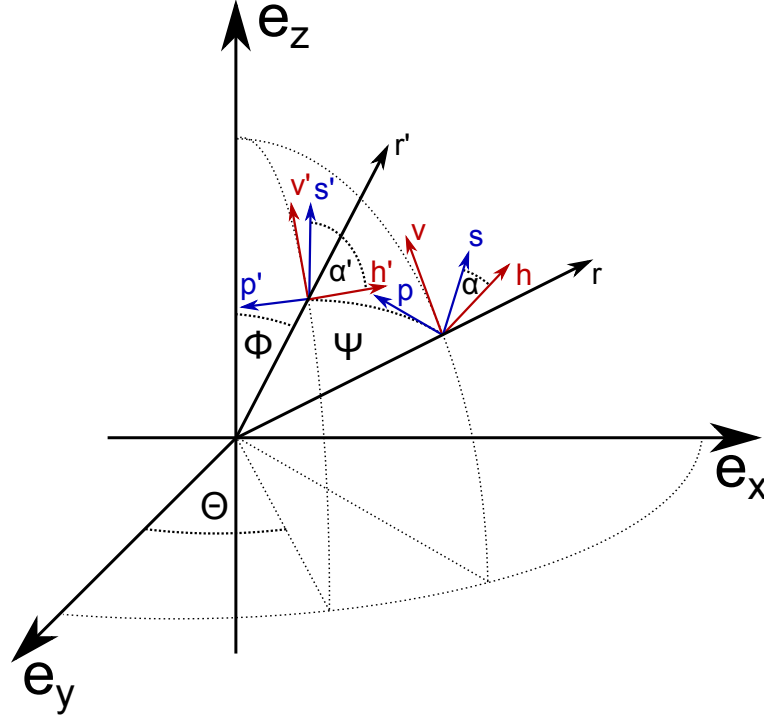


Figure 2.2: *Geometrical configuration of scattering on spherical particles.* The scattered light is redirected along the scattering plane by an angle of ψ . In order to apply the Müller matrix $\hat{M}(\psi)$, the target coordinate system $(\vec{p}, \vec{s}, \vec{r})$ has to be transformed in the lab coordinate system $(\vec{v}, \vec{h}, \vec{r})$ along the angle α .

The scattering of radiation on spherical particles is among the most common features in MC RT codes. However, it increases the complexity of the RT problem since scattering is anisotropic and requires the evaluation of additional probability functions. The probability for a scattering event is quantified by the albedo of the particle

$$a = \frac{C_{\text{sca}}}{C_{\text{ext}}}, \quad (2.21)$$

the measurement of the fraction of light deflected from the incident beam. Here, C_{ext} and C_{sca} are the cross sections of extinction and scattering, respectively. For each radiation-particle interaction a random number $0 < z \leq 1$ is chosen. In the case of $z > a$ we

have a scattering event. Rather than converting the radiation to internal energy, it emits the same amount of energy in a different direction and the polarization state of light becomes altered where as the wavelength remains the same. When describing polarized light at the physical level of radiative transfer theory, the change in the Stokes vector can be calculated with the help of the Müller matrix or scattering matrix $\hat{M}(\psi)$ (see van de Hulst, 1981; Bohren & Huffman, 1983, for details). The elements of the Müller matrix are dependent and for spherical particles we get

$$\hat{M}(\psi) = \begin{pmatrix} M_{11} & M_{12} & 0 & 0 \\ M_{12} & M_{11} & 0 & 0 \\ 0 & 0 & M_{33} & M_{34} \\ 0 & 0 & -M_{34} & M_{33} \end{pmatrix}. \quad (2.22)$$

Note that the scattering matrix elements are also a function of material, particle size, wavelength and scattering angle. The parameters of the Stokes vector before \vec{S} and after \vec{S}' each scattering event is determined by the Müller matrix with $\vec{S}' \propto \hat{M}(\psi)\vec{S}$. The direction of propagation \vec{r}' after the scattering defines the so called scattering plane with the original direction of radiation \vec{r} . The coordinate system of the Stokes vector $(\vec{r}, \vec{h}, \vec{v})$ is usually defined with respect to an external coordinate system. Here, \vec{v} is parallel to the z-axis of the external coordinate system and perpendicular to the direction of propagation \vec{r} with $\vec{h} = \vec{v} \times \vec{r}$. In order to apply the Müller matrix the Stokes vector has to be transformed into the same coordinate system as the scattering plane $(\vec{p}, \vec{s}, \vec{v})$ where \vec{p} is in the scattering plane and $\vec{s} = \vec{p} \times \vec{r}$. The rotation angle α is defined to be between the vectors \vec{s} and \vec{h} and the scattering angle ψ between \vec{r}' and \vec{r} is defined by

$$\cos(\psi) = \vec{r}' \cdot \vec{r}. \quad (2.23)$$

Since the Stokes parameters I and V are invariant under transformation, the rotation matrix that transforms the Stokes vector into the coordinate system of the scattering plane is:

$$\hat{R}(\alpha) = \begin{pmatrix} 1 & 0 & 0 & 0 \\ 0 & \cos(2\alpha) & -\sin(2\alpha) & 0 \\ 0 & \sin(2\alpha) & \cos(2\alpha) & 0 \\ 0 & 0 & 0 & 1 \end{pmatrix}. \quad (2.24)$$

After the scattering event, the stokes vector is in the new coordinate system $(\vec{r}', \vec{h}', \vec{v}')$. In order to align the new coordinate system again with the external coordinate system, the Stokes vector has to be rotated by an angle of α' . Finally, the change in the Stokes vector because of scattering can be calculated with

$$\vec{S}' = \hat{R}(-\alpha)\hat{M}(\psi)\hat{R}(\alpha')\vec{S}'. \quad (2.25)$$

After each scattering event a new direction of the photon package has to be determined. The phase function describes the probability of each propagation direction after the scattering event. The choice of the parametrization of the analytical phase functions or the use of numerical phase functions can be chosen dependent on the required accuracy and available computational equipment (Hong, 1985; Draine, 2003; Sharma & Roy, 2008).

2.2.4.1 Isotropic scattering

In the case of isotropic scattering each direction after the scattering event has the same probability. The sampling process is the same as by thermal remission. The new direction \vec{r}' is sampled from a uniform distribution of points on the surface of a unit sphere and depends on the three parameters $u = 1 - 2z_1$, $t = 2\pi z_2$, and $r = \sqrt{1 - u^2}$ and can be calculated by

$$\vec{r}' = (r \cos(t), r \sin(t), u)^T. \quad (2.26)$$

Here, the quantities z_1 and z_2 are random numbers.

2.2.4.2 Anisotropic scattering

In contrast to isotropic scattering, anisotropic scattering is characterized by a preferential scattering direction. The spatial distribution of scattering directions is highly dependent on the size parameter

$$x = \frac{2\pi a}{\lambda}. \quad (2.27)$$

Here, a is the radius of the particle. In the limit of $1 \gtrsim x$, the Henyey-Greenstein (HG) phase function (Henyey & Greenstein, 1941) is the most widely used parametrization of the phase function and provides a good single-parameter approximation with

$$F(\psi) = \frac{1}{4\pi} \frac{1 - g^2}{[1 + g^2 - 2 * \cos(\psi)]^{\frac{3}{2}}}. \quad (2.28)$$

This phase function depends on scattering angle ψ and the asymmetry parameter $g \in [-1, 1]$ where $g = 0$ means isotropic scattering, $g = -1$ backward scattering, and $g = 1$ forward scattering, respectively. The anisotropy parameter g can analytically be calculated with

$$g = \langle \cos(\theta) \rangle = \frac{\int_0^{4\pi} F(\theta, \phi) \cos(\theta) d\Omega}{\int_0^{4\pi} F(\theta, \phi) d\Omega}. \quad (2.29)$$

In the case of $\lambda \approx x$ for homogenous and spherical particles a solution to this problem can be found with Mie scattering theory (Mie, 1908; Debye, 1909). Here, the phase function of scattering can be expanded in terms of an infinite series of associated Legendre polynomials (Mie, 1908; Wolf & Voshchinnikov, 2004). The coefficients of the series can be calculated with the refractive index of the particles material.

2.2.5 Dust grain heating

In the specific case of the ISM, the particles of interest are dust grains with different sizes and materials. Under the prevalent conditions in the ISM, these dust grains can be assumed to be in radiative equilibrium with its environment. Dust grains re-emit an equal amount of energy absorbed in the optical wavelength regime as infrared radiation. The mean intensity J_λ per wavelength can be calculated by a RT MC simulation. A number of N_{ph} photon packages are sent through the grid and interact with the dust component in each cell. For an albedo with $z > a$ we have an absorption event. In this case, the photon package stops and a new photon package starts with a different wavelength. The condition of LTE allows to determine the dust temperature in each cell with C_{abs} the cross section of absorption implicitly by solving

$$\int_0^\infty C_{\text{abs}} B_\lambda(T) d\lambda = \int_0^\infty C_{\text{abs}} J_\lambda d\lambda. \quad (2.30)$$

2.2.5.1 Immediate re-emission method

The method of immediate re-emission corrects the dust temperature for each absorption event. For the re-emitted dust photon a new wavelength will be sampled in such a way that the dust grain remains in LTE. The dust temperature T_d is the essential parameter for thermal radiation. The new dust temperature T_d can then be calculated for a number N_{abs} of absorbed photon package (Bjorkman & Wood, 2001) with

$$T_d = \frac{N_{\text{abs}}}{N_{\text{ph}}} \frac{L}{4\sigma C_p(T_d)}. \quad (2.31)$$

Here, L is the luminosity of the photon package emitting source, σ is the StefanBoltzmann constant, and $C_p(T_d)$ is the mean absorption cross section weighted over the Planck function with

$$C_p(T_d) = \int_0^\infty C_{\text{abs}} B_\lambda(T_d) d\lambda. \quad (2.32)$$

Eq. 2.31 can be numerically solved by an iterative approach. In order to achieve an increase in computational time the mean absorption cross section $C_p(T_d)$ can alternatively

be pre-calculated. The strength of this method is that it operates with the correct spectral wavelength distribution of the photon packages. The temperature is corrected after each absorption event. This means the dust re-emitted photons with the wrong spectrum $B_\lambda(T_{d,i-1})$. The index i indicates the number of absorptions. In order to correct this error the wavelength of the new photon package has to be sampled from the spectrum of $B_\lambda(T_{d,i}) - B_\lambda(T_{d,i-1})$. In the continuous case the new wavelength λ_i can be sampled with a random number z from

$$z = \frac{\int_0^{\lambda_i} C_{\text{abs},\lambda} \frac{dB_\lambda(T_{d,i})}{dT} d\lambda}{\int_0^\infty C_{\text{abs},\lambda} \frac{dB_\lambda(T_{d,i})}{dT} d\lambda} \quad (2.33)$$

where $\frac{dB_\lambda(T_{d,i})}{dT}$ is the derivative of the Planck function after the temperature. The disadvantage of this technique is a poor convergence because the temperature of the dust is updated just at each point of absorption.

2.2.5.2 Continuous absorption technique

A more efficient way to calculate the dust temperature by means of a RT MC simulation is the method presented in Lucy (1999). As shown in Sect. 2.2.3 the mean intensity can be calculated by adding up the contributions to the energy of radiation deposited in each cell. This is particularly advantageous in optically thin regions where the probability of a dust-radiation interaction is low. The method of continuous absorption allows to calculate the rate \dot{A} of absorbed energy per time and mass with

$$\dot{A} = \frac{\epsilon_0}{4\pi V \Delta t} \sum_{n=1}^{N_p} C_{\text{abs}} l. \quad (2.34)$$

Since, we assume LTE the rate of absorbed energy is equal to the rate of re-emitted energy ($\dot{A} = \dot{E}$) and the dust temperature can be determined by

$$\dot{E} = 4\pi V \int C_{\text{abs},\lambda}(a) B_\lambda(T_d) d\lambda. \quad (2.35)$$

The temperature correction occurs here after several separate MC RT simulations until the temperature converges. This means, that the final dust temperature has to be calculated by means of iterating. After each RT MC simulation the temperature is corrected in the entire grid. At each point of absorption the new wavelength is sampled from

$$z = \frac{\int_0^{\lambda_i} C_{\text{abs},\lambda} B_\lambda(T_{d,i}) d\lambda}{\int_0^\infty C_{\text{abs},\lambda} B_\lambda(T_{d,i}) d\lambda} \quad (2.36)$$

which represents the false spectral distribution of wavelengths as shown in Sect. 2.2.5.1.

2.3 The discrete dipole approximation (DDA)

The mathematical tools available to calculate the optical properties of dust grains such as the extinction, absorption, and scattering cross sections as well as the scattering phase function are limited. For the interpretation and fitting of observational data the shape of the dust grains are usually assumed to be spherical. Indeed, the spherical model of interstellar dust grains is promising for the interpretation of extinction and fitting of observational data based on scattered light. Considering the growth of dust grains by means of coagulation the dust grains can be expected to have irregular shapes rather than symmetrical ones. Furthermore, non-spherical dust grains are also required to account for the observed polarization of starlight and the materials of interstellar dust, especially graphite, are highly anisotropic. Therefore, Mie theory is of limited use for the determining the parameters required by the specific radiative transfer problem in the ISM.

In order to get the optical properties of dust grains with arbitrary shapes the discrete dipole approximation (DDA) can be applied. Originally a version of the DDA accurate for grains far smaller than the wavelength was proposed by DeVoe (1964). Later, the DDA was extended by Purcell & Pennypacker (1973) to study interstellar dust grains. A consistent formulation of the DDA method was presented in Draine (1988) and later implemented in the *DDSCAT* code Draine & Flatau (1994).

The basic idea behind this method is to approximate the required arbitrary dust grain shape by a periodic lattice with a limited number of N dipoles. Each lattice position \vec{r}_j is associated with a dipole moment of

$$\vec{p}(\vec{r}_j, t) = \vec{p}(\vec{r}_j, 0) \exp(-i\omega_0 t) = \alpha_j \vec{E}_j \quad (2.37)$$

where α_j is the polarizability. The polarizability is a symmetrical tensor and can be written as a series (Draine & Flatau, 1994) with the real and imaginary part of the complex refractive index $m(\omega) = \varepsilon(\omega) + \kappa(\omega)$ of the dust grain material as parameter. The components of the electromagnetic field for the j -th dipole can be written as a sum of an incident and scattered wave with

$$\vec{E}_j = \vec{E}_{\text{inc},j} + \vec{E}_{\text{sca},j} \quad (2.38)$$

and

$$\vec{B}_j = \vec{B}_{\text{inc},j} + \vec{B}_{\text{sca},j}. \quad (2.39)$$

In order to calculate the dipole moments at each position \vec{r}_j of the lattice, the radiation field for each dipole inside the dust grain must be determined by adding up the contributions of the dipoles at distance $\vec{r}_{jl} = \vec{r}_j - \vec{r}_l$. Assuming plane waves with the direction of

propagation \hat{n} and the wave vector $\vec{k} = \frac{2\pi}{\lambda}\hat{n}$ gives the electric and magnetic components with

$$\vec{E}_{\text{inc},j} = \vec{E}_{\text{inc},0} \exp\left(i\vec{k}\vec{r}_j - i\omega t\right), \quad (2.40)$$

$$\vec{E}_{\text{sca},j} = e^{(-i\omega t)} \sum_{j=1, l=1; j \neq l}^N \frac{\exp\left(i\vec{k}\vec{r}_{jl}\right)}{r_{ij}^3} \left[k^2 \vec{r}_{jl} \times (\vec{p}_l \times \vec{r}_{jl}) + \frac{1 - ikr_{jl}}{r_{jl}^2} \left(3\vec{r}_{jl}(\vec{p}_l \vec{r}_{jl} - r_{jl}^2 \vec{p}_l) \right) \right], \quad (2.41)$$

$$\vec{B}_{\text{inc},j} = \vec{B}_{\text{inc},0} \exp\left(i\vec{k}\vec{r}_j - i\omega t\right), \quad (2.42)$$

and

$$\vec{B}_{\text{sca},j} = e^{(-i\omega t)} \sum_{j=1, l=1; j \neq l}^N k^2 \frac{\exp\left(i\vec{k}\vec{r}_{jl}\right)}{r_{jl}^3} (\vec{p}_l \times \vec{r}_{jl}) \left(1 - \frac{1}{ikr_{jl}} \right), \quad (2.43)$$

respectively. The DDA allows to obtain an approximate description of the interior radiation field of the dust grain. The associated net force acting on each dipole is due to the gradient in the electric field and the Lorentz force on the currents induced by the magnetic field

$$\vec{F}_{\text{rad}} = \sum_{j=1}^N \Re(\vec{p}_j \nabla_j) \Re(\vec{E}_j) + \Re\left(\frac{d\vec{p}_j}{dt}\right) \times \Re(\vec{B}_j). \quad (2.44)$$

This equation applies to the incident and the scattered radiation alike and the net force is $\vec{F}_{\text{rad}} = \vec{F}_{\text{inc}} + \vec{F}_{\text{sca}}$. Because of anisotropic radiation the force \vec{F}_{rad} produces a torque $\vec{\Gamma}_{\text{rad}} = \sum_{j=1}^N \vec{r}_j \times \vec{F}_j$ on the dust grain. Averaged over time the torque is defined by the energy density u_{rad} of the incident radiation and the effective dust grain radius a with

$$\langle \vec{\Gamma}_{\text{rad}} \rangle = \vec{Q}_\gamma \pi a^2 \frac{4\pi |\vec{E}_{\text{inc},0}|^2}{kc} = \frac{1}{2} a^2 u_{\text{rad}} \lambda \vec{Q}_\gamma. \quad (2.45)$$

Here, the dimensionless parameter $Q_\Gamma = |\vec{Q}_\gamma|$ is the alignment efficiency and depends on the orientation of the dust grain and its angle with respect to the incident light. Since

the solution for each dipole moment in the lattice is known within the limits of numerical precision this allows to calculate the extinction efficiency of the entire grain with

$$Q_{\text{ext}} = \frac{4k}{a^2 |E_{\text{inc},0}|^2} \sum_{j=1}^N \Im \left(\vec{E}_{\text{inc},j}^* \vec{p}_j \right) \quad (2.46)$$

by considering the amount of radiation that is lost in the direction of an external incident wave using the optical theorem. The extinction efficiency can be separated by the part of incident radiation that is lost because of scattering and the part that is absorbed from the grain material: $Q_{\text{ext}} = Q_{\text{abs}} + Q_{\text{sca}}$. The scattering efficiency Q_{sca} can be calculated by means of a far field approximation. By averaging the amount of radiation scattered in each direction \vec{n}_{sca} over the solid angle Ω the scattering efficiency can be calculated by

$$Q_{\text{sca}} = \frac{k^4}{\pi a^2 |E_{\text{inc},0}|^2} \int \sum_{j=1}^N [\vec{p}_j - \vec{n}_{\text{sca},j} (\vec{n}_{\text{sca},j} \vec{p}_j)] \exp(-ik\vec{n}_{\text{sca},j} \vec{r}_j) d\Omega. \quad (2.47)$$

A similar calculation can be performed for the scattering asymmetry parameter g (see Sect. 2.2.4.2) to quantify the probability distribution of the scattering directions. The parameter g can be written as

$$g = \langle \cos(\theta) \rangle = \frac{k^3}{\pi a^2 Q_{\text{sca}}} \int \vec{n}_{\text{sca},j} \vec{k}_j \left| \sum_{j=1}^N [\vec{p}_j - \vec{n}_{\text{sca},j} (\vec{n}_{\text{sca},j} \vec{p}_j)] \exp(-ik\vec{n}_{\text{sca},j} \vec{r}_j) \right|^2 d\Omega \quad (2.48)$$

where θ is defined to be the angle between incident and scattered radiation.

Absorption in the dust grain takes place because of dissipation of energy in each of the dipoles in the lattice. The sum over the rate of energy dissipation gives the absorption efficiency with

$$Q_{\text{abs}} = \frac{k^4}{\pi a^2 |E_{\text{inc},0}|^2} \int \sum_{j=1}^N [\vec{p}_j - \vec{n}_{\text{sca},j} (\vec{n}_{\text{sca},j} \vec{p}_j)] \exp(-ik\vec{n}_{\text{sca},j} \vec{r}_j) d\Omega. \quad (2.49)$$

A plane wave with arbitrary direction of polarization can be dissected in its components parallel and perpendicular to the symmetry axis. Each component suffers a different phase lag which means they are no longer in phase after passing a dusty region on a path with length l . Consequently, the incident wave becomes circular polarized as long as the direction of polarization is not parallel or perpendicular to the symmetry axis of

the dust grain. The phase lag is defined to be the angle $\delta\phi$ in radians at which a plane wave is out of phase compared with the incident light and can be written as

$$\delta\phi = \pi a^2 n_d Q_{\text{pha}} l \quad (2.50)$$

where n_d is the number density of dust grains and Q_{pha} is the phase lag efficiency. It is obvious, that the precision of the DDA increases with a higher number N of applied dipoles in the lattice. However, the DDA requires the distance between neighboring dipoles to be small compared to the structure of the dust grain surface and the considered wavelength. The range at which the DDA is valid can be estimated by

$$a < 5 \frac{\lambda}{|m|} \left(\frac{N}{10^6} \right)^{\frac{1}{3}}. \quad (2.51)$$

Consequently, the use of the DDA is mostly limited by the complex refractive index $|m|$ and the computational efforts to calculate optical properties towards larger dust grains grow with N^3 .

Chapter 3

The alignment of dust in the ISM

The polarization of starlight depends on the efficiency and direction of dust grain alignment, the material properties, the size distribution, and the shape of the dust. All these quantities are poorly constrained. Furthermore, grain alignment is not an isolated process but highly dependent on the complex interplay of the dust with the interstellar medium (ISM) and the interstellar radiation field (ISRF).

In order to quantify this interplay, in this chapter we introduce first the ISM and ISRF in which the dust grains are embedded. Then we focus on the dust component and the available theories developed so far to account for the alignment of dust grains with the local magnetic field in the ISM. Finally, we shortly discuss alternative alignment mechanisms and reasons why they are not considered in this thesis.

3.1 The interstellar medium (ISM)

Although the ISM has been investigated intensively since its discovery, some of its physical properties remain still unknown. The ISM is permanently enriched with heavier elements from stellar ejections and supernovae as well as dust forged in the atmospheres of red giants. However, its main constituent remains hydrogen. The component of the ISM can be classified by the thermal phases of hydrogen (e.g. McKee & Ostriker, 1977; Ferrière, 2001).

- **Cold molecular gas:** The molecular phase accounts for approximately 50 % of the ISM. Since, molecular hydrogen cannot sustain photo-dissociation because of interstellar ultra-violet (UV) radiation, it can only be found in dense regions with a gas typical gas number density n_g of 10^{12} m^{-3} - 10^{15} m^{-3} . The temperatures in this phase are in the order of 10 K because dense regions are shielded by surrounding gas and therefore no heating processes by radiation can take place.

- **Neutral gas:** The neutral atomic hydrogen emits and absorbs at a characteristic 21 cm line. This component can be found in a cold and a warm phase. The cold phase has a cloudy structure with temperatures of about 100 K and a number density of $20 \times 10^{10} \text{ m}^{-3}$ - $50 \times 10^{10} \text{ m}^{-3}$. The warm phase is diffuse and less dense with $n_g \approx 10^9 \text{ m}^{-3}$ and temperatures of $10^3 \text{ K} - 10^4 \text{ K}$.
- **Warm ionized gas:** This phase can be found in HII regions around *O*-type and *B*-type stars where the gas is ionized by stellar radiation and planetary nebula. Since, this regions are centered around stars they extend up to a few 100 pc. The densities range typically 10^{10} m^{-3} - 10^{13} m^{-3} with a temperature below 10^4 K .
- **Hot ionized gas:** This gas phase is supported by supernovae ejections. The ejected gas expands supersonically in the surrounding ISM and heats the gas up to 10^6 K . Typically densities and scales are 10^6 m^{-3} and 10 pc, respectively.

The mass of the ISM ranges up to 10 % of the total baryonic mass in a galaxy.

3.2 The interstellar radiation field (ISRF)

The space between the stars is also filled by electromagnetic radiation (Kaplan & Pikel’Ner, 1970). This radiation field originates from three major sources:

- **Cosmic microwave background (CMB):** The background of microwave radiation with a temperature of 2.7 K is a remnant of the big bang and is evenly distributed in the universe. This cosmic microwave radiation manifests itself in a maximum at $\approx 1 \text{ mm}$ in the spectrum of the ISRF.
- **Heated dust:** The dust in the ISM is heated by nearby stars and the ISRF itself. In molecular clouds, HI, and HII regions the dust temperature is in the order of 10 K - 50 K. Higher temperatures in the range of 200 K - 500 K can be found for very small dust grains heated by UV radiation and dust heated by M types stars. The distribution of dust temperature lead to a maximum in the spectrum of the ISRF at $100 \mu\text{m}$.
- **Stellar radiation:** In the wavelength regime of $0.1 \mu\text{m} - 10 \mu\text{m}$ the ISRF is dominated by the stellar radiation. Here, the spectrum is dominated of *O/B* stars with characteristic maximal values of about $1 \mu\text{m}$.

The distribution of radiation of the ISRF inside the galaxy varies greatly dependent on the local distribution of stars and is expected to be larger toward the galactic center. For all MC RT calculations considering the contributions of the ISRF we use the data of

Moskalenko *et al.* (2006) modeled with the parameters of stellar populations and high energy γ -rays typical in our local galactic neighborhood as well as the CMB contribution (see Fig 3.1). The model was extrapolated in the mm regime of wavelength. Here, we assumed the CMB to be a perfect black body radiator with a temperature of $T_{\text{CMB}} = 2.7$ K (Fixsen, 2009).

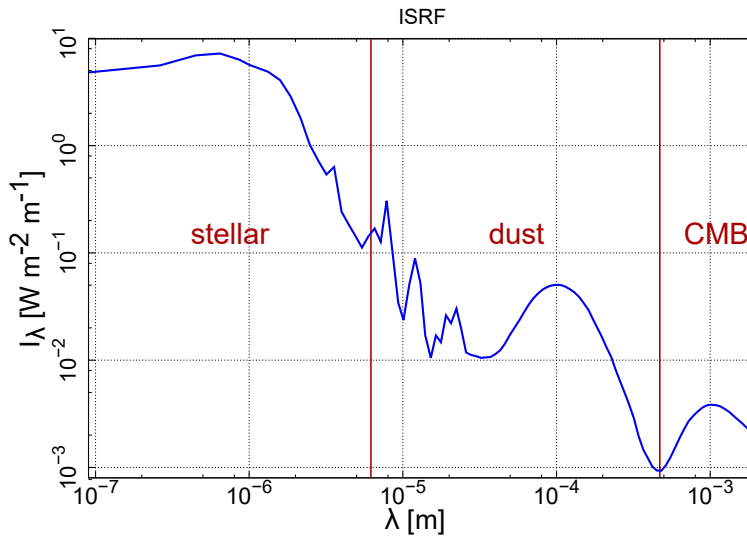


Figure 3.1: *Spectral intensity distribution of the local ISRF.* The plotted data was adapted from Moskalenko *et al.* (2006) and extrapolated.

3.3 Interstellar dust

The dust in the ISM is a compound of dielectric and refractive materials with a distinct size distribution and complex shapes. The formation of dust starts primarily in the expanding atmospheres of luminous red giants. Solid grains can be formed by nucleation of abundant elements. The exact chemical composition is determined by the elements available in the stellar atmosphere. Hence, the expected composition of interstellar dust grains are silicates with inclusions of iron as well as carbonaceous components. Later, the dust grains grow by the processes of condensation and coagulation in stellar winds, interstellar clouds and circumstellar disks. Large dust grain populations can be redistributed towards smaller sizes by mean of photo-dissociation or inside the bow shocks

of outflow lobes. Radiative pressure transports the dust grains away from its birthplace into the ISM. The amount of dust mass is predicted to be only a few per cent of the total mass of the ISM. However, dust manifests itself by absorption and scattering of light from the ultra-violet (UV), the near-infrared (NIR) wavelength regime, and by thermal re-emission of the absorbed energy in the infrared and sub-millimeter (sub-mm) range.

3.3.1 Mechanisms of dust grain alignment

Commonly, the expression „dust grain alignment mechanism“ refers to theories proposed to account for the alignment of dust grains in the ISM with the direction of the magnetic field. However, this alignment theories entail all effects, the ones who can lead to alignment as well as misalignment of dust grains. Hence, we introduce in this section just the relevant two physical effects that result in dust grain alignment and treat the theories of grain alignment as well as their steady state solutions in the following sections.

3.3.1.1 The Davis Greenstein (DG) effect

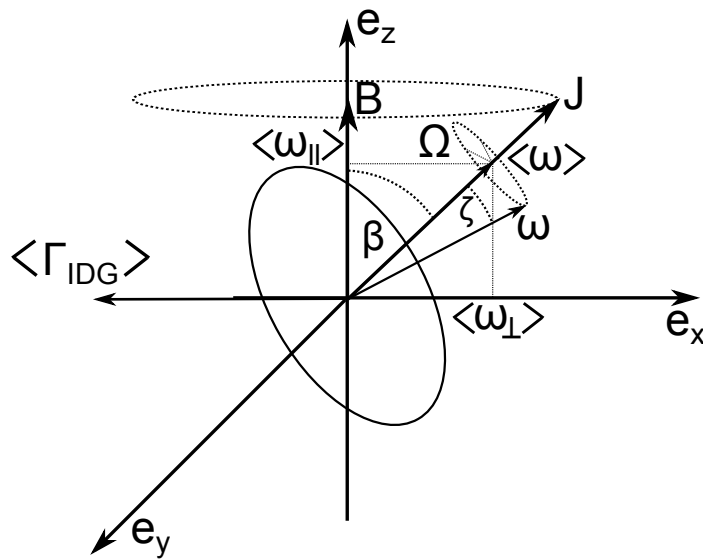


Figure 3.2: Schematic illustration of the Davis Greenstein effect.

Paramagnetic materials have unpaired electrons which possess no counterpart on its orbit and can therefore choose their spin orientation freely. In the presence of a magnetic

field the unpaired electrons align with the field direction inducing a net magnetic moment and the dust grain becomes magnetized. In the reference frame of a rotating dust grain the direction of a constant magnetic field \vec{B}_0 changes and the electrons become contentiously reoriented. Like a spinning top, a rotating dust grain performs a nutation around its angular momentum \vec{J} . For an angular velocity ω the magnetization $\vec{M}(t)$ as seen by the dust grain material is modulated with

$$\vec{M}(t) \propto \vec{B}_0 [\chi' \cos(\omega t) + \chi'' \sin(\omega t)] \quad (3.1)$$

where χ is the magnetic susceptibility. The susceptibility depends on the magnitude of the applied field and the properties of the dust material. Rearranging of electron spins gives rise to a complex component of the susceptibility χ'' with $\chi = \chi' + i\chi''$. Consequently, the real part χ' of the susceptibility is in phase with the rotation of the dust grains while the imaginary part χ'' is phase shifted by $\pi/2$. This means that electrons in the lattice of the dust material cannot follow the change of magnetic field direction instantaneously and causes vibrations in the lattice. This vibrations are directly correlated to the loss of rotational energy. Thus, the spin-lattice interaction partly leads to a transfer of rotational energy into internal heat. In order to change its orientation a net torque has to act on the dust grain. In the reference frame of the rotating dust grain the magnetic field B is not constant but its orientation becomes a function of time and the resulting torque Γ_{DG} takes the following form:

$$\vec{\Gamma}_{\text{DG}} = \vec{\mu} \times \vec{B} \propto \frac{V\vec{B}\vec{\omega}}{\omega^2} (\chi_0 - \chi') (\vec{B} \times \vec{\omega}) + \frac{V\chi''}{\omega} (\vec{B} \times \vec{\omega}) \times \vec{B}. \quad (3.2)$$

Here, χ_0 is the magnetic susceptibility for the stationary case with $\omega = 0$ and V is the volume of the dust grain defining the magnetic moment $\vec{\mu} = V\vec{M}$.

Since the dust grain is assumed to perform an additional nutation around its rotation axis, the first term on the left hand side in Eq.3.2 averages out by integrating over the precession angle Ω and the net torque can simply be expressed as

$$\frac{d\vec{J}}{dt} \langle \vec{\Gamma}_{\text{DG}} \rangle \propto \frac{V\chi''}{\omega} (\vec{B} \times \langle \vec{\omega} \rangle) \times \vec{B} \quad (3.3)$$

where the brackets $\langle \rangle$ indicate the averaging. This means the angular velocity $\langle \vec{\omega} \rangle$ and angular momentum \vec{J} of the rotating dust grain are parallel. Consequently, the direction of the net torque $\langle \vec{\Gamma}_{\text{DG}} \rangle$ is in the same planes as \vec{B} and $\langle \vec{\omega} \rangle$ and it acts on the dust grain in a direction perpendicular to the magnetic field (see Fig. 3.2).

In Eq.3.2 the first term is perpendicular to ω and therefore also irrelevant for the calculation of the loss of rotational energy E_{rot} . The change of rotational energy over time

can now be expressed as

$$\frac{dE_{\text{rot}}}{dt} = \langle \vec{\Gamma}_{\text{DG}} \rangle \langle \vec{\omega} \rangle = -\frac{V\chi''}{\omega} \left(\vec{B} \times \langle \vec{\omega} \rangle \right)^2. \quad (3.4)$$

Since the right hand side of Eq.3.4 is negative the dust grain loses rotational energy as a result of paramagnetic dissipation as long as $\langle \vec{\omega} \rangle$ possesses a component perpendicular to \vec{B} . Without external perturbations the net torque $\langle \vec{\Gamma}_{\text{DG}} \rangle$ can act long enough to steadily decrease the cone angle β and the dust grain becomes perfectly aligned.

3.3.1.2 The Barnett effect

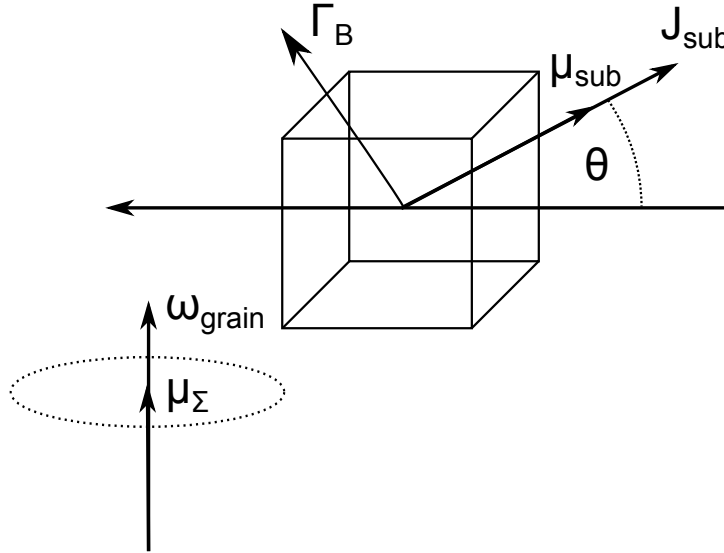


Figure 3.3: Schematic illustration of the Barnett effect. The cube indicates a subsystem within the rotating dust grain and the horizontal line is a segment of the subsystem's orbit.

In Barnett (1917) it was noticed that non-ferromagnetic materials can become magnetized without an external magnetic field involved. This effect can be understood in a classical picture of the magnetic moment of an atom with one electron, a mass m , and the charge e . The electron is orbiting the core with the angular velocity ω at a distance r and the system has consequently a magnetic moment of $\mu = e\frac{1}{2}r\omega^2$. The angular momentum is directly proportional with the magnetic moment and defined as

$$\vec{J} = mr^2\omega = 2\frac{m\mu}{e}. \quad (3.5)$$

Considering a subsystem of unit volume in a rotating dust grain the net angular momentum is given by

$$\vec{J}_{\text{sub}} = 2\frac{m}{e} \sum_i \mu_i \cos(\theta_i). \quad (3.6)$$

Here, the angle θ is between the angular momentum $\vec{\omega}$ of the dust grain and the orbital path of the subsystem around the rotation axis (see Fig.3.3). As the dust grain rotates a net torque of

$$\vec{\Gamma}_{\text{sub}} = \frac{d\vec{J}_{\text{sub}}}{dt} = \vec{\omega} \times \vec{J}_{\text{sub}} \quad (3.7)$$

acts on each of the subsystems of the grain (see Fig. 3.3). Like a gyroscope the subsystems tend to an equilibrium state with $\frac{d\vec{J}_{\text{sub}}}{dt} = 0$. This forces the magnetic moment of each subsystem to align with the angular velocity $\vec{\omega}$ over time. By sharing its angular momentum with its subsystems, a rotating dust grain with volume V gains a net magnetic moment $\vec{\mu}_{\Sigma}$ independent of the presence of an external magnetic field. Considering an external magnetic field the net torque on a rotating dust grain is $\vec{\Gamma}_{\Sigma} = \vec{\mu}_{\Sigma} \times \vec{B}$. Any cone angle $\beta > 0^\circ$ would increase the potential energy by $E_{\text{pot}} = -\mu_{\Sigma} B \cos(\beta)$. Consequently an angle of $\beta = 0^\circ$ represents the favorable energetic state and the dust grain tends to align with its angular momentum in direction of the magnetic field.

3.3.2 Dust grain alignment theories

The challenge in the development of a consistent dust grain alignment theory is not so much the question of what aligns the dust grain but what effect spins up the dust grain in the first place. As shown in the previous section the DG effect as well as the Barnett effect are well established as the dominant mechanisms to explain the grain alignment behavior. However, both effects require the dust grains to rotate with an angular velocity sufficiently fast enough for both alignment mechanisms to work efficiently. A consistent grain alignment theory, therefore, should entail the mechanism to spin up the dust grains, quantify the effects that prevents perfect grain alignment and deliver a steady state solution in order to calculate the long term grain alignment efficiency. Since the polarization of starlight was an established fact, several theories of grain alignment were proposed.

3.3.2.1 Imperfect Davis Greenstein (IDG) alignment

To account for the alignment by the DG effect the dust grain requires an initial angular momentum. The rotation of dust grains is common in the ISM since they are exposed to

a permanent bombardment by the surrounding gas. However, the tendency of dust grains to align perfectly with their rotation axis parallel to the magnetic field directions is also heavily opposed by a random gas bombardment. When the rate of bombardment is too high compared to the characteristic timescales of the DG effect, the orientation of the dust grains remains randomized. In a steady state situation both gas bombardment and grain alignment are in balance. In this case a distribution function for the cone angle β can be derived. Where as in Davis & Greenstein (1951) a solution based on a corpuscular point of view was presented later in Jones & Spitzer (1967) a similar solution using a statistical approach over an ensemble of dust grains using the Fokker-Planck equation was derived. In general terms, this equation describes the time evolution of a probability density function taking drag, drift, and diffusion of the system into account. In this particular case the Fokker-Planck equation takes the form

$$\frac{\partial f_i}{\partial t} = -\frac{\partial}{\partial J_i} f_i \langle \Delta J_i \rangle + \frac{1}{2} \frac{\partial^2}{\partial J_i^2} f_i \langle (\Delta J_i)^2 \rangle. \quad (3.8)$$

In the reference frame of the magnetic field the angular momentum of the dust can be decomposed into its J_x , J_y and J_z components and the Fokker-Planck equation can be solved in each direction independently with $i = x, y, z$, $f_i := f(J_i) dJ_i$, and the fraction of dust grains is within the range $J_i - J_i + dJ_i$. Here, the brackets $\langle \rangle$ denote the mean value. Since the change in angular velocity is a result of both random gas bombardment and the DG effect the mean values are $\langle \Delta J_i \rangle = \langle \Delta J_i \rangle_g + \langle \Delta J_i \rangle_{\text{DG}}$ and $\langle (\Delta J_i)^2 \rangle = \langle (\Delta J_i)^2 \rangle_g + \langle (\Delta J_i)^2 \rangle_{\text{DG}}$, respectively.

The number of gas-dust collisions per time is $\pi a^2 n_g \bar{v}_g$ where \bar{v}_g is the average gas velocity. With each collision a gas particle carries an angular momentum $J = -\frac{2}{3} \omega_i a^2$ away. With the definition of angular momentum $J_i = \omega_i I_i$ and because \bar{v}_g follows from the Maxwell-Boltzmann distribution we get for the coefficients of gas collision

$$\langle \Delta J_i \rangle_g = \frac{4J_i a^4 n_g \sqrt{m_g k_B T_g}}{3I_i} \quad (3.9)$$

and

$$\langle (\Delta J_i)^2 \rangle_g = \frac{8}{3} T_d a^4 n_g \sqrt{m_g k_B^3 T_g}. \quad (3.10)$$

As shown in Sect. 3.3.1.1 the DG effect transfers the angular velocity component perpendicular to the magnetic field direction into heat. For this reason the coefficients are $\langle \Delta J_z \rangle_{\text{DG}} = \langle \Delta (\Delta J_z)^2 \rangle_{\text{DG}} = 0$. Using Eq.3.3 the coefficients for the DG effect can be written as

$$\langle \Delta J_i \rangle_{\text{DG}} = -\frac{VB^2 \chi''}{I_i \omega_i} \quad (3.11)$$

and

$$\langle (\Delta J_i)^2 \rangle_{\text{DG}} = \frac{2}{\omega} k_B T_d V B^2 \chi'' . \quad (3.12)$$

Solving Eq. 3.11 and Eq. 3.12 for the steady state solution $\frac{\partial f_i}{\partial t} = 0$ where the DG effect and the gas bombardment are in balance, the normalized distribution functions of angular momentum are

$$f_i(J_i) = \frac{1}{\sqrt{2\pi I_i k_B T_{\text{av}}}} \exp\left(-\frac{J_i^2}{2I_i k_B T_{\text{av}}}\right) \quad (3.13)$$

and for $i \neq z$

$$f_z(J_z) = \frac{1}{\sqrt{2\pi I_z k_B T_g}} \exp\left(-\frac{J_z^2}{2I_z k_B T_g}\right) . \quad (3.14)$$

Here, the average temperature is defined to be

$$T_{\text{av}} = \frac{T_g + \delta T_d}{1 + \delta} \quad (3.15)$$

with the parameter

$$\delta_{\text{DG}} = \frac{\langle \Delta J_i \rangle_{\text{DG}}}{\langle \Delta J_i \rangle_i} = \frac{\chi'' B^2}{2a\omega n_g} \sqrt{\frac{2\pi}{m_g k_B T_g}} \approx 8.23 \times 10^{31} \frac{\kappa B^2}{a n_g T_d \sqrt{T_g}} [\text{m}] . \quad (3.16)$$

Furthermore, the dimensionless material constant is $\kappa = 2.5 \times 10^{-12}$ (Davis & Greenstein, 1951), assuming a constant magnetic susceptibility $\chi(\omega)$ for paramagnetic dust grain materials. This means that the angular momentum is maxwellian distributed in the equilibrium state. By defining $f_{\text{DG}}(\beta)d\Omega$ as the fraction of grains having an angular momentum of J within a solid angle of $d\Omega$ at the angle β , the cone angle distribution follows from integrating Eq. 3.13 and Eq. 3.14 and can be written as

$$f_{\text{DG}}(\xi, \beta) = \frac{\xi \sin(\beta)}{(\xi^2 \cos^2(\beta) + \sin^2(\beta))^{\frac{3}{2}}} . \quad (3.17)$$

Here, the distribution function depends on the cone angle β and the alignment parameter ξ . The latter encapsulates all physical quantities and can be written as

$$\xi^2 = \frac{a + \delta_0 \frac{T_d}{T_g}}{a + \delta_0} \quad (3.18)$$

with $\delta_0 = a\delta_{DG}$. The IDG alignment works similar to that of a heat engine. It requires a significant difference between dust temperature and gas temperature with $T_d \gg T_g$. This becomes apparent in the extreme case where $T_d = T_g$, $\xi = 1$, and the distribution of angular momenta follows $f_{DG}(1, \beta) = \sin(\beta)$. In this case the orientation of dust grains remains randomized. The characteristics of the IDG cone angle distribution function is that it behaves like a Dirac delta function with $\lim_{\xi \rightarrow 0} f_{DG}(\xi, \beta) = \delta(\beta)$, which means perfect alignment. The parameter δ_0 acts as an upper threshold. Dust grains with effective radii $a \geq \delta_0$ can be considered to be randomized since they do not contribute significantly to the net polarization (see also Fig. 4.5).

3.3.2.2 Magneto-mechanical (GOLD) alignment

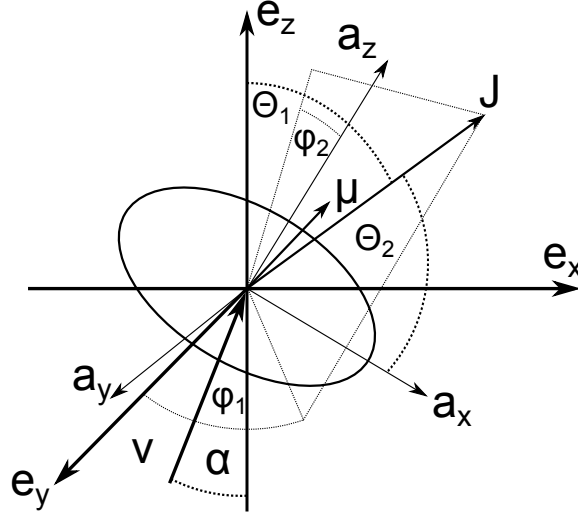


Figure 3.4: Schematic illustration of dust grain alignment according to Magneto-mechanical (GOLD) theory. The vectors \mathbf{e}_x , \mathbf{e}_y , and \mathbf{e}_z represent the external reference frame where as the vectors \mathbf{a}_x , \mathbf{a}_y , and \mathbf{a}_z represent the reference frame with respect to the minor axis and the major axis, respectively.

Gas bombardment increases the angular momentum J of the dust grain and after N_c collisions. Hence, the net angular momentum increased by

$$\vec{J}(N_c) = \vec{J}_{eq} + \vec{J}_{st} = I_d \omega_{eq} + \sum_{n=1}^{N_c} m_g \vec{r} \times \vec{v}_g \quad (3.19)$$

where \vec{r} is the radius from the dust grain's center of mass to the point of impact, I_d is the maximum moment of inertia of the dust grain and m_g and \vec{v}_g are the mass and the velocity difference between gas and dust. Although this simple picture does not include magnetic fields, it shows that this mechanism requires a predominant direction. Random gas bombardment alone could not account for grain alignment because the angular momentum is $\vec{J}_{st} = \sum_{i=1}^{N_c} m_g \vec{r} \times \vec{v}_g = 0$. Hence, the grain orientation is fully determined by the equilibrium angular momentum J_{eq} which is randomly orientated. Subsequently, just in the presence of a directed gas stream the non-spherical dust grains orientate with their angular momentum perpendicular to the gas stream.

A second condition necessary for the mechanical alignment is the supersonic velocity of the gas colliding with the dust grains. The random and isotropic gas bombardment is associated with a thermal temperature $T_g \propto m_g v_g^2 / k_B$. As shown in Eq. 3.19 the angular momentum increases with each gas-dust by N_c collision up to $N_c v_g m_g r$. However, random bombardment by gas with a thermal velocity v_T and dust rotation reach an equilibrium state and the maximum amount of mean angular velocity ω_d of the dust grain can be estimated from $I_d \omega_d^2 \propto k_B T_g$. In order for the net angular momentum to orient with the gas the contribution of the stream has to be dominant $J_{st} \gg J_{eq}$ and consequently the velocity of the gas stream has to be supersonic to exceed the thermal velocity $v_{st} \gg \sqrt{m_d / m_g} v_{th}$.

The orientation of the angular momentum \vec{J} is dependent on both the angle Θ_d in the reference frame of the dust grain and the angle Θ_g in the reference frame of the gas, whereas the distribution function $f_g(n, \vec{x})$ for the precession angle is defined by new variables. These variables are n , the number of gas-dust collisions over time and the pseudo vector components are $x_1 = J$, $x_2 = \cos(\Theta_d)$, and $x_3 = \cos(\Theta_g)$ (see Fig. 3.4). The change in angular momentum for each single collision event is considerably small and the distribution function follows also the Fokker-Planck equation with

$$\frac{\partial f_g(n, \vec{x})}{\partial n} = \sum_{i=0}^2 a_i(\vec{x}) \frac{\partial f_g(n, \vec{x})}{\partial x_i} + \sum_{i=0}^2 \sum_{j=0}^2 b_{ij}(\vec{x}) \frac{\partial^2 f_g(n, \vec{x})}{\partial x_i \partial x_j}. \quad (3.20)$$

The coefficients a_i and b_{ij} determine the change in angular momentum with

$$a_0 = \left\langle \Delta x_2 \frac{\partial \Delta x_1}{2 \partial \Delta x_2} + \Delta \Phi_2 \frac{\partial \Delta x_1}{2 \partial \Delta \Phi_1} - \Delta x_1 \right\rangle, \quad (3.21)$$

$$a_i = \left\langle \Delta x_1 \frac{\partial \Delta x_i}{2 \partial \Delta x_1} + \Delta x_i \frac{\partial \Delta x_i}{2 \partial \Delta x_i} + \Delta \Phi_i \frac{\partial \Delta x_i}{2 \partial \Delta \Phi_i} - \Delta x_i \right\rangle, \quad (3.22)$$

and

$$b_{ij} = \langle \Delta x_i \Delta x_j \rangle. \quad (3.23)$$

Here, the brackets $\langle \rangle$ stand for the averaging over the dust grain surface. As a consequence, the angles Φ_1 and Φ_2 average out. The exact solution of Eq. 3.20 is straight forward and is performed in Dolginov (1974) in great detail. For an ellipsoidal dust grain with its major and minor semi-axis l_a and l_b , respectively, the resulting distribution function can be expressed as

$$f_g(n, \vec{x}) \propto n^{-\frac{3}{2}} \exp \left[-\frac{J^2 (1 + g \cos^2(\Theta_2) + s \cos^2(\Theta_1))}{2nl_b^2 p^2 (1 + s + g)} \right] \quad (3.24)$$

with the normalizing constant C . Here, the parameter

$$s = -\frac{1}{2} \left(\frac{\langle p^2 \rangle - 3\langle p_z^2 \rangle}{\langle p^2 \rangle - \langle p_z^2 \rangle} \right) \quad (3.25)$$

is defined to be the external flux anisotropy and

$$g = \frac{1}{2l_b^2} (2l_a^2 - 2l_b^2) \quad (3.26)$$

is the grain non-sphericity. Both s and g are in the same range of $[-0.5, \infty]$ where $g < 0$ stands for an oblate dust grain and $g > 0$ for a prolate one. The squared momentum p^2 of a single collision is averaged over time and is $\langle p^2 \rangle \neq 0$ for an anisotropic gas flux. The final distribution function of Eq. 3.24 represents an approximate solution in the case of where $J_{st} \gg J_{eq}$ obtained under the condition that the quantities $\cos(\theta_1) \longleftrightarrow \cos(\theta_2)$ and $g \longleftrightarrow s$ are simultaneously interchangeable. For this reason the distribution function is just valid for ellipsoidal shaped dust grains. In this thesis we refer to magneto-mechanical alignment furthermore simply as GOLD alignment.

It was suggested that dust grains with a helicity can also spin up to a super thermal rotation in the presence of sub-sonic velocity streams. However, the possible mechanical alignment of helical dust grains in sub-sonic environments is currently discussed (Lazarian & Hoang, 2007) but not yet finally confirmed.

3.3.2.3 Imperfect internal alignment (II)

Originally, it was assumed that the Barnett effect aligns the angular momentum J perfectly with the maximum moment of inertia $I_{||}$ of the dust grain. It was first noted by Purcell (1979) that two internal mechanisms can cause the dust grain to rotate around

all the axis of inertia leading to an additional precession of J around I_{\parallel} . Inelastic dissipation in the dust grain material as a result of stress is caused by a sudden change in the dust grain's angular velocity. However, for thermally rotating dust grains, the Barnett dissipation can be considered to be the major effect of imperfect internal alignment. Since the dust grain material possesses a temperature, the lattice of the dust grain is subject to thermal fluctuations. As shown by Jones & Spitzer (1967) the DG effect can transfer rotational energy into heat. A similar coupling between magnetic moments and lattice of the dust grain material can also transfer heat into rotational energy. Consequently, the magnetization of the dust grain remains not constant because of thermal fluctuations resulting in a rotation with respect to all three body axis of the dust grain.

Assuming the dust temperature to be constant the distribution function of internal alignment follows the Boltzmann distribution. In a steady state where the dust grain exchanges no energy with its environment, the distribution function of dust grains with an opening angle ζ between I_{\parallel} and J (see Lazarian & Roberge, 1997a) is

$$f_{\Pi}(J, \zeta) = \exp(-\alpha [1 + \delta \sin^2(\zeta)]) \quad (3.27)$$

with $\alpha = J^2/2I_{\parallel}k_{\text{B}}T_{\text{d}}$ and $\delta = I_{\parallel}/I_{\perp} - 1$.

3.3.2.4 Radiative torque (RAT) alignment

Paramagnetic alignment and magneto-mechanical alone cannot explain the full range of observational data. A significant degree of linear polarization in subsonic ISM environments and the discovery of very large aligned dust grains suggested that the understanding of grain alignment is incomplete (see Andersson, 2015, for review). In Dolginov & Mitrofanov (1976a) the Barnett effect was first identified to induce a magnetic moment large enough to make the magnetic field direction the dominant axis of dust grain precession. The rotation of the dust grains is a result of different absorption and scattering cross sections for right and left circular polarized radiation. This may result in a net torque Γ_{RAT} acting on the dust grain. For dust grains that undergo many absorption and scattering events this radiative torque (RAT) can spin up dust grains and subsequently increase the alignment efficiency. Since this effect depends primarily on the grain shape, the dust can effectively be spun up over a long period of time. An analytical model (AMO) of grain alignment was presented by Hoang & Lazarian (2007) in excellent agreement with the numerical studies of Draine & Weingartner (1996, 1997) and Weingartner & Draine (2003). Later in Hoang & Lazarian (2007) the effect of thermal fluctuations within the dust grain material and the contributions of gas-dust collisions were incorporated in the AMO.

In the AMO the dust grain alignment is determined by the time evolution of angular

momentum

$$\frac{dJ}{dt} = MH - J(t) \quad (3.28)$$

and the angle ε , β , and φ can be expressed with the angles between external reference frame and the reference frame of the wobbling dust grain (see Fig. 3.5 left panel) with

$$\frac{d\varepsilon}{dt} = M \frac{F}{J} \quad (3.29)$$

and

$$\frac{d\varphi}{dt} = \frac{M}{\sin(\varepsilon)} G - \Omega_B. \quad (3.30)$$

The quantity M is a collection of physical parameters with:

$$M = \frac{\gamma u \lambda a^2 t_{\text{gas}}}{2I_{\parallel}}. \quad (3.31)$$

Here, u_{λ} is the energy density of the radiation field at wavelength λ , Ω_B is the Larmor precession rate, J_{th} the thermal angular momentum because of gas bombardment, and t_{gas} (see Eq. 3.33) is the gas dumping time. The radiative torque Γ_{RAT} is decomposed into the components H (spin-up torque), F (alignment torque) and G projected on the axis of the reference frame of the dust grain. For the stationary solution with $\frac{dJ}{dt} = 0$ the AMO predicts attractor points in the parameter space under the condition of $\frac{dF}{d\varphi} < 0$. Consequently the dust grains align at two attractor points (see Fig. 3.5 right panel). One with $H < 0$ where the angular momentum is thermal (low-J) and another one with $H > 0$ with super-thermal angular momentum (high-J). Most dust grains drift to the unstable low-J attractor, where they are prone to thermal fluctuations and are subsequently partially misaligned. Here, gas bombardment can increase the grain alignment efficiency because dust grains become lifted from the low-J to the high-J attractor point. In order to align stably at the high-J attractor point the torque acting on the dust grain needs to be dominated by radiation and not random gas bombardment. Hence, the AMO demands as a criterion of stability: $\omega_{\text{rad}} > 3 \times \omega_{\text{th}}$. With increasing effective dust grain radius a , RATs become more efficient and the dust grains get supra-thermally spun up. The effective radius a_{alg} at which the dust grains start to align stably can be calculated as presented in Bethell *et al.* (2007) with

$$\left(\frac{\omega_{\text{rad}}}{\omega_{\text{th}}} \right)^2 = \frac{a \rho_d}{\delta m_H} \left[\frac{\int Q_{\Gamma}(\varepsilon) \lambda \gamma_{\lambda} \bar{u}_{\lambda} d\lambda}{n_g k_B T_g} \frac{1}{1 + \frac{t_{\text{gas}}}{t_{\text{rad}}}} \right]^2. \quad (3.32)$$

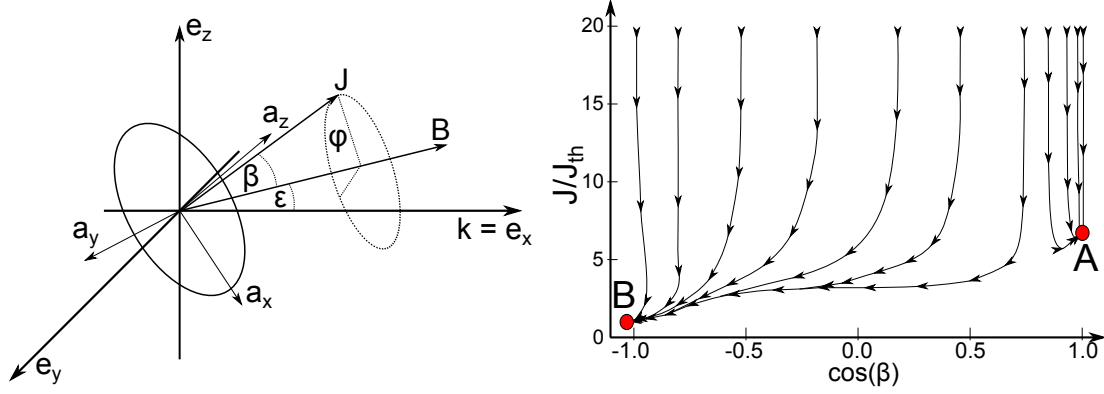


Figure 3.5: *Left panel: Schematic illustration of dust grain alignment according to RAT theory.* The vectors \mathbf{e}_x , \mathbf{e}_y , and \mathbf{e}_z represent the external reference frame whereas the vectors \mathbf{a}_x , \mathbf{a}_y , and \mathbf{a}_z represent the reference frame with respect to the minor axis and the major axis, respectively. *Right panel: Exemplary trajectory map with data adapted from Hoang & Lazarian (2007).* Dust grains settle over time either on the high- J attractor point A with parallel alignment or at the low- J attractor point B with anti-parallel alignment with respect to the magnetic field direction.

Here, γ_λ and \bar{u}_λ are the local anisotropy and the mean energy density, respectively, of the radiation field. For the local anisotropy of the radiation field $\gamma_\lambda = 0$ means isotropic radiation and no net torque Γ_{RAT} acts on the dust grain and $\gamma_\lambda = 1$ means all radiation approaches the dust grain from only one direction. In the later case RAT alignment work most sufficiently. The parameter $Q_\Gamma(\varepsilon)$ is the alignment efficiency of the RAT which depends on the angle ε between the predominate direction in the radiation field and the magnetic field direction. The efficiency $Q_\Gamma(\varepsilon)$ is also a function of grain size, wavelength, and grain composition. The shape dependent parameter δ is introduced in Draine & Weingartner (1996, 1997) in detail. The characteristic time scales of gas bombardment t_{gas} and radiation t_{rad} acting on the dust grains can analytically be calculated following Draine & Weingartner (1996) with

$$t_{\text{gas}} = \frac{\pi \rho_d a}{3 n_g \sqrt{2 \pi m_H k_B T_g}} \quad (3.33)$$

and

$$t_{\text{rad}} = 7.8489 \frac{k_B^2}{\hbar^2 c} \frac{\rho_d a^3 T_d^2}{\bar{u} \langle Q_{\text{abs}} \rangle}, \quad (3.34)$$

respectively. Here, ρ_d is the density of the dust grain material itself, and $\langle Q_{\text{abs}} \rangle$ is the efficiency of absorption weighted over the spectral distribution of the mean energy density \bar{u}_λ with

$$\langle Q_{\text{abs}} \rangle = \frac{1}{\bar{u}} \int \bar{u}_{\lambda} Q_{\text{abs},\lambda} d\lambda \quad (3.35)$$

and

$$\bar{u} = \int \bar{u}_{\lambda} d\lambda. \quad (3.36)$$

Consequently, to check for supra-thermal conditions requires also information about the local anisotropy γ_{λ} and the mean energy density \bar{u}_{λ} of the radiation field. This can be achieved by means of a RT MC simulation.

3.4 Discussion

That dust grains align with the magnetic field direction cannot just occur by paramagnetic means. Indeed, it was first proposed by Martin (1971) that a magnetic moment can also be induced by charged rotating dust grains. This magnetic moment would result in grain precession with an orientation either parallel or perpendicular with respect to the magnetic field direction. This effect was thought to be a promising explanation for the observed large scale grain alignment of dust grains. Although, this effect completes the list of effective grain alignment mechanisms the contribution of charged dust grains is miniscule. As pointed out in Dolginov & Mitrofanov (1976a) the Barnett effect is a much more efficient mechanism for inducing a magnetic moment in the dust grain material. Hence, the charge of a dust grain is a parameter that can be neglected for most dust grain alignment considerations.

Initially, the DG effect with its analytical treatment seemed to be the most promising to explain large scale grain alignment. Later, numerical studies of Purcell (1969) the DG in its original form seems to be too slow to account for a significant grain alignment in the ISM. This is mostly because of the expected thermal rotation of dust grains spun up only by gas-dust collisions. The resulting angular momentum is too low for the galactic magnetic field (≈ 5 nT) to be the dominating direction of grain alignment. However, the critical parameters here are related to the dust composition. In Jones & Spitzer (1967) it was already noted, that dust grains could have encapsulated clusters of iron. The abundance of ferromagnetic inclusions in dust grains is supported by observations (Martin, 1995) and laboratory experiments (Bradley, 1994). The critical parameter here is δ_{DG} (see Eq. 3.16). Ferromagnetic inclusions would increase the imaginary part χ'' of the magnetic susceptibility by a factor of 10 – 100. Consequently, the upper threshold δ_{DG} would be shifted towards higher values and more dust grain species could effectively align. Another explanation for a higher efficiency of the DG mechanism is to consider

an ice component in the dust grain composition. Over time, H_2O molecules can stick on the grains surface forming an ice mantle. As a result of the unknowns of the exact dust composition inside the ISM, the parameter δ_{DG} can be assumed to be a free parameter over several orders of magnitude.

An alternative to boost grain rotation was proposed by Purcell (1975). Dust grains can act as a catalyst for the formation of H_2 molecules. Ionized hydrogen sticks to the dust grain surface because of permanent collisions. The captured particles wander along the dust grain surface because of thermal fluctuations and quantum tunneling. Finally, two H ions can overcome their potential barrier on the grain surface and a H_2 molecule gets emitted. Here, the emitted H_2 molecule acts similar to a rocket thruster by means of the transfer of energy from the H_2 formation into rotational energy. In principle this pinwheel torque as a result of H_2 emission can also spin up the dust grain to super-thermal rotation. In order to expect a net torque acting on the dust grain, the formation of a H_2 molecule has to occur on fixed positions on the dust grain surface. The dust grain surface can always be expected to have irregularities giving rise to special active side where hydrogen particles can be trapped. However, this active side has to be long lived. Otherwise the dust grain can even be slowed down when an active site relocates its position on the grain surface. The effective increase of the IDG alignment by the pinwheel effect was shown in Purcell (1979). Later, the influence to a higher alignment efficiency was also demonstrated for RATs in Hoang & Lazarian (2007) by a numerical approach. However, the active sites required by the Purcell mechanism are expected to change positions by formation of heavier elements and can even disappear completely over time (Hoang & Lazarian, 2007). Additionally, a fraction of hydrogen has to be ionized to provide a reservoir for the Purcell mechanism to work at all. This means the pinwheel torques can not account for super-thermally rotating dust grains in dark molecular clouds. Furthermore, the influence of pinwheel torques to grain alignment has to be calculated by means of a numerical approach e.g. a time evolution model using a Runge-Kutta method. This would push a MC RT simulation beyond reasonable time scales making the pinwheel torques of minor practical use for the purposes of this thesis. A mechanism to spin up dust grains similar to that of Purcell's pinwheel torques was suggested by Sorrell (1995). Here, it was speculated that the evaporation of grain mantles by cosmic radiation might spin up dust grains to super-thermal angular velocities. However, it is evident that the evaporating grain mantles provide just thrust over a limited amount of time not long enough to account for long-term grain alignment. The expected flux of cosmic radiation is also expected to be several orders of magnitude to low (Lazarian & Roberge, 1997b) for this mechanism to be of relevance. Hence, the effect of evaporating grain mantles is also not considered in this thesis.

The alignment of dust grains even in dark cores of molecular clouds can be explained by RATs. Simultaneously, the RAT alignment mechanism is not sufficient for the alignment

of small dust grains. The alignment of small dust grains can be accounted by IDG theory. Both, RAT and IDG, predict the dust grain alignment with the angular momentum parallel to the magnetic field direction. However, this seems not to hold in general. In contradiction to the expected behavior of RAT and IDG alignment observational findings (Rao *et al.*, 1998; Cortes *et al.*, 2006) indicate that the grain alignment might also occur with an angular momentum perpendicular to the magnetic field. Indeed, molecular outflows can provide the necessary supra-sonic environment for the GOLD alignment to work. For this reasons, the focus of this thesis lies on the IDG, RAT, and GOLD alignment theories combined with the effects of imperfect internal alignment to study the effects of aligned dust grains as a tool to observe the magnetic field morphology in various ISM environments.

Chapter 4

The *POLARIS* MC RT code

The astronomical objects of interest are manifold, from single stars over molecular clouds to galaxies and galaxy clusters. Measurements of radiation are the dominant tool in astronomy to investigate the fundamental physical processes in such objects. However, the big drawback of observations is that the detection of radiation on the plane of the sky can only deliver a projected view of objects with complex spatial density and temperature distributions. Consequently, the interpretation and analysis of observational data requires a detailed RT modeling to deal with projection effects.

In this chapter we introduce the major features of *POLARIS* (**POLARized RadIation Simulator**) a 3D MC RT code newly developed from scratch and capable of dust heating and polarization calculations. First, in order to account for the effects of non-spherical partially aligned dust grains we have to extend the basic concepts of MC and the physics RT introduced in chapter 2. For the considered theories of IDG, RAT, and GOLD alignment as well as the reduced grain alignment efficiency because of II alignment, the calculation of grain alignment efficiency comes with the computational burden of solving integral equations. To perform MC RT simulations within acceptable time scales in the order of days we present the analytical solutions and applied approximations. The required calculation time of the MC RT simulation can be furthermore reduced by MC optimization techniques. Finally, we present a dust database with pre-calculated parameters of dust grains allowing to simulate the effects of dust grain alignment on synthetic observational data.

4.1 Major features and specifications

POLARIS is a 3D MC continuum RT code designated to post-process complex density, temperature, and magnetic field distributions resulting from multi-scale MHD simulations. The aim is to calculate synthetic polarization maps to investigate the observability

of different MHD scenarios. *POLARIS* can make use of the full parameter set (density, temperature, velocity and magnetic field distributions, sources of radiation) delivered by MHD simulations to perform dust heating and complex polarization RT calculations. The code is platform independent and completely written in C++ in a strict object oriented manner.

The code works in three independent main operation modes:

- i) **Dust heating:** In a first MC RT simulation, the dust grains are self-consistently heated. Here, a model of an astrophysical object can include an arbitrary number of radiation sources all contributing to the dust grain heating calculation.
- ii) **Calculation of the overall radiation field:** Once, the dust temperature has been calculated a second MC RT simulation is started. Here, the spectral mean energy density \bar{u}_λ and local anisotropy factor γ_λ of the radiation field is determined to calculate the parameters for radiative torque (RAT) alignment (see Sect. 3.3.2.4). This mode is similar to the dust heating mode, except that the sources that emit the radiation are stellar sources as well as the heated dust itself.
- iii) **Synthetic observational data:** Finally, calculations of spectral energy distributions (SEDs), synthetic multi-wavelength intensity, and polarization maps as well as statistical analysis data are created.

To access the full functionality the code *POLARIS* parses script files. Predefined commands in a pseudo XML style implemented in the code allows the user to create scripts with sequences of operation modes.

4.2 The octree grid

In MC RT simulations the photon packages propagate in grids with cells of constant physical parameters (e.g. density or temperature). One of the difficulties of MC RT simulations is the partition of complex distributions of physical parameters adequately in a grid structure. Linear grids with a uniform resolution are too memory intensive in order to resolve huge gradients. The choice of the grid geometry and the coordinate system can be made by exploiting the symmetry of certain astrophysical systems (e.g. a spherical coordinate system for RT simulations of disks). However, this would limit any code to the simulations of special cases.

In order to make RT simulations possible for a broad variety of astrophysical systems, all RT simulations are performed on an adaptive octree grid. Such a grid starts with a cube which represents the entire volume of the model. If the gradient of a certain

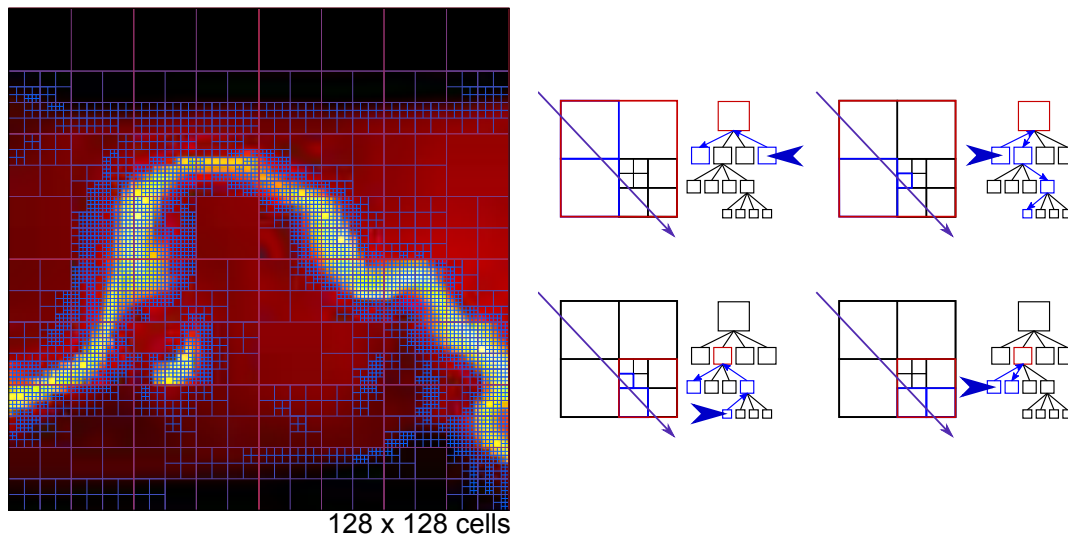


Figure 4.1: *Left panel: Exemplary color coded density distribution of the center plane of a MHD shock simulation in arbitrary units. The grid refinement was performed according to both criteria presented in Sect. 4.2. As a result of refinement the ratio of remaining cells to maximal possible cells is $\approx 1/200$. Right panel: Schematic illustration of light ray propagation through the octree. The neighboring cell can most efficiently be found with a pointer running up and down through the grid levels.*

parameters is still not adequately matched by the current resolution, each cube can now be divided into eight sub-cubes. The criterion of grid refinement are as follows:

- i) $\chi_{i,l} > A \times l \bar{\chi}$
- ii) $\frac{\chi_{i,l}}{\chi_{k,l}} > B, \quad j \neq k.$

Here, $\chi_{i,l}$ can be any physical quantity in the i -th cell or k -th cell, respectively, on the l -th grid level. The first criterion compares the quantity χ with the average $\bar{\chi}$ of the entire grid multiplied by a constant A and the number of levels l . This ensures that quantities with high values are in areas of the grid with a better resolution. The second criteria deals with high gradients. As long as the fraction of χ in neighboring cells is higher than some constant B the grid will be refined until the cubes are sufficiently small.

The choice of an octree grid structure for the MC RT calculations provides major advantages:

- In the octree grid each cell is either a leaf and contains a set physical parameters or is a branch and is divided into eight sub cells. This allows to represent the grid in a tree like structure. The time required to find the neighboring cell for a photon

package penetrating a cell wall scales with the order of levels ($\mathcal{O}(l)$). This means that the photon package can propagate efficiently. Furthermore, it allows for parallel computing since several photon packages can propagate within an octree grid independently, each on a separate processor. Consequently, the calculation time approximately scales then with the number of processors.

- For highly complex distributions of physical parameters and in a non adaptive grid the refinement has to be increased in the entire grid to match high gradients in certain areas. This leads to an unnecessary high memory requirement. In an octree grid areas with high gradients can be refined while cells with a similar or identical set of parameters can be combined to a single cell.
- Modern MHD codes (e.g. Fryxell *et al.*, 2000) make already use of adaptive grid refinements and the original grid structure can be maintained by the octree grid. This means no artificial information is introduced into the MHD data by means of a conversion process to another grid structure.

4.3 Radiation emitting sources

The photon package starts its life cycle in a MC RT simulation with a characteristic spatial emission, energy, wavelength, and an initial degree of linear and circular polarization mimicking a certain type of emitting source. In order to cover the broad variety of radiating objects in the ISM that we provide several classes of photon emitting sources in *POLARIS*.

- **Point source:** In our simulations we consider the spatial extension of a star to be small compared to the cell size. Hence, no possible irregularities associated with the surface of the star such as sun spots or limb darkening is taken into consideration and a star is considered to be a simple point source. The direction of each photon package is calculated similar to the procedure of Sect. 2.2.4.1. The distribution of wavelengths is determined by the spectral luminosity of the star and can hence be sampled from

$$z = \frac{\int_0^{\lambda_i} L_\lambda(R_*, T_*) d\lambda}{\int_0^\infty L_\lambda(R_*, T_*) d\lambda}. \quad (4.1)$$

Here, R_* and T_* are the radius and the surface temperature of the star, respectively. Each newly created photon package carries an energy per unit time of

$$\dot{E} = \frac{L(R_*, T_*)}{N_{\text{ph}}} \quad (4.2)$$

away.

- **Diffuse source:** The diffuse source is intended to mimic a spacial extended source such as a molecular cloud surrounding a star or an entire starfield located in a region small in comparison to the entire model space. This source is similar to the point source. However, the photon packages start not from a single point but from a position inside a sphere with a certain radius. The positions follow a Gaussian distribution meaning that the probability to start at a position toward the center of the sphere is higher.
- **ISRF source:** Even in the absence of stars the dust has a certain temperature. This can be due to heating by the ISRF. The ISRF contributes also to the overall radiation field inside the model space and is therefore of relevance for the calculation of the RAT alignment efficiency. As for the point source the ISRF source sends photon packages in random direction. However, the starting point is from the surface of a sphere which surrounds the model space. The SED is defined by an external file. So far, we use exclusively the ISRF model from Moskalenko *et al.* (2006) as introduced in Sect. 3.2. The model data has been interpolated to match the wavelengths of the dust grain database presented in Sect. 4.6.
- **Background source:** The background source is designed to simulate objects outside the model. This objects are assumed to be far enough behind that the emitted light rays entering the model can assumed to be parallel. The background source is defined by a pixel matrix where each pixel has its characteristic SED, intensity, and state of linear and circular polarization.
- **Dust source:** Since dust with a certain temperature contributes also to the radiation field in the model space, each dust containing cell is considered as a separate photon package emitting source. The photon package starts from a random position evenly distributed in the entire cell volume. Since, the dust is assumed to be a black body radiator the wavelengths of the photon packages can be sampled from Eq. 2.33. The energy per unit time of an individual photon package is determined by the dust properties with a modified black body spectrum

$$\dot{E} = \frac{4\pi N_d}{N_{\text{ph}}} \int_0^\infty C_{\text{abs},\lambda} B_\lambda(T_{\text{d},i}) d\lambda \quad (4.3)$$

where N_d is the number of dust grains in the cell volume. The resulting probability distribution function for different dust temperature is shown in Fig. 4.2.

Besides the propagation of photon packages inside the model space in order to perform dust heating calculations or to determine the overall radiation field, the detection of

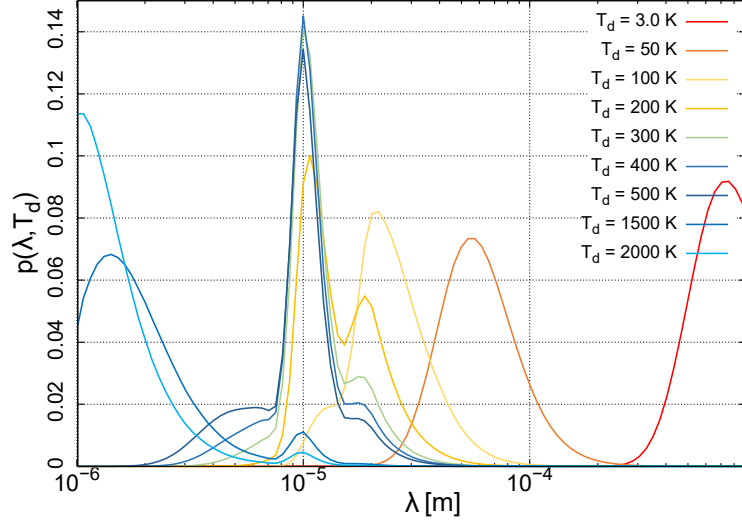


Figure 4.2: *PDF of re-emitted wavelengths for different dust grain temperatures.* The PDF was calculated according to 2.33 and the dust grain model as presented in Sect. 4.6 with astro-silicate as material and a maximal dust grain size of $a_{\max} = 250$ nm.

radiation is a vital process. Similar to a CCD camera the detector in *POLARIS* consists of a pixel matrix array to store the intensity and the polarization state of the photon packages leaving the grid towards the observer. An arbitrary number of detectors can be positioned with *POLARIS* each for a specific orientation and wavelength.

4.4 Optimization techniques

A 3D MC RT simulation is challenging concerning run time and the capabilities of available computational equipment. However, in complex environments provided by MHD simulations, the physically well motivated dust models, and alignment mechanisms require a huge parameter space to solve the RT problem including polarization. For this reason *POLARIS* is equipped with several optimization algorithms to perform RT calculations on a reasonable time scale in the order of days.

4.4.1 The modified random walk (MRW)

The number of absorption and scattering events increases with optical depth (see Sect. 2.2.2). This can slow down a MC RT simulation significantly, especially when a source is embedded in a high density region. In order to propagate photon packages in regions with extreme optical depth more efficiently we implemented the MRW, a technique that uses a diffusion approximation instead of a MC approach (Min *et al.*, 2009; Robitaille, 2010) for optically thick regions. Hence, several MC steps can be combined in a single calculation. In regions where the mean free path length is much smaller than the density gradient, the energy is transported by the diffusion of photons. In the stationary case the photon diffusion of dust temperature T_d follows the equation

$$\nabla(D_R \nabla T_d^4) = 0 \quad (4.4)$$

where

$$D_R = \frac{1}{3} \frac{1}{n_d \bar{C}_r} \quad (4.5)$$

is the diffusion coefficient. The calculation of the Rosseland mean extinction cross section \bar{C}_r is similar to that of the mean absorption cross section in Eq. 2.32. Here, C_{ext} is weighted over the temperature derivative of the Planck function:

$$\bar{C}_r(T)^{-1} = \frac{\int_0^\infty C_{\text{ext}}^{-1} \frac{dB_\lambda(T)}{dT} d\lambda}{\int_0^\infty \frac{dB_\lambda(T)}{dT} d\lambda}. \quad (4.6)$$

The criterion for the MRW is such that the closest wall distance R_{MRW} has to be larger than the diffusion coefficient times some constant c :

$$R_{\text{MRW}} > c \times D_R. \quad (4.7)$$

When the constant is chosen to be small, the MRW does not increase the MC RT simulation significantly whereas larger values come with a higher error. If the MRW criterion is fulfilled, the photon package propagates to a random position on the surface of a sphere of radius R_{MRW} . In a MC RT simulation this distance would have been much longer to reach the same point. However, in optically thick regions propagation of photon packages are similar to a random walk where the passed distance follows a statistical distribution. Solving Eq. 4.4 leads to the following relation:

$$l_{\text{MRW}} = -\ln(y) \left(\frac{R_{\text{MRW}}}{\pi} \right)^2 \frac{1}{D_R}. \quad (4.8)$$

Here, l_{MRW} is the average distance a photon package would have passed to the surface of the sphere in a MC simulation and the quantity y can be sampled with a random number z from the series:

$$z = 2 \sum_{n=1}^{\infty} (-1)^{n+1} y^{n^2}, y \in [0; 1]. \quad (4.9)$$

The relation between z and y can be pre-calculated and interpolated to decrease the calculation time even more. This means that the photon package travels at each MRW step a distance R_{MRW} . However, for the overall radiation field the contribution of the photon package along the distance l_{MRW} is considered.

For the MRW, we agree with the a values of $c = 7$ for the constant as suggested in Min *et al.* (2009) because of MC RT test simulations of dust in artificial test scenarios. As expected by the results of Min *et al.* (2009) the MRW slightly overestimates the dust temperature in the order of a few percent. Similar test scenarios reveal, that the MRW cannot be applied for the calculation of the RAT alignment. While the mean energy density is correctly approached, the MRW leads to a loss of information about the anisotropy of the radiation field.

4.4.2 Forced first scattering

A different problem emerges in optically thin regions. An interaction between dust and radiation is very unlikely and a significantly high amount of photon packages can escape the grid without any interaction. In order to compensate the increase in signal-to-noise ratio one requires a higher amount of photon packages. As a solution, each photon package is forced to interact at least one time (Cashwell & Everett, 1959). For each photon package newly emitted by a source, an optical depth τ_{esc} is calculated to the boundaries of the grid along the current direction. A new optical depth τ_{forced} to the first interaction point is then randomly selected from

$$\tau_{\text{forced}} = -\log(1 - z(1 - f_e)) \quad (4.10)$$

with a random number z and the factor $f_e = \exp(-\tau_{\text{esc}})$. In order to compensate for the forced interaction the photon package p_0 has to be split in two packages p_1 and p_2 with their energy adjusted by $E_1 = (1 - f_e)E_0$ and $E_2 = f_e E_0$ at the forced interaction point. From this point on each photon package follows independently the usual propagation scheme of Sect. 2.2 to the boundaries of the grid.

4.4.3 Ray-tracing

At longer wavelengths scattering becomes increasingly insignificant and a ray-tracing algorithm can be applied. The criterion for this approach is an albedo of

$a = C_{\text{sca}}/C_{\text{ext}} \ll 100$. Instead of a MC approach in the ray-tracing technique the photon packages follow a straight line between a background source and the detector. Here, we simply add up all contributions in each cell because of extinction and re-emission along the line of sight. Compared to a RT simulation with scattering, the ray-tracing approach is more time efficient and allows to achieve an excellent signal-to-noise ratio (e.g. Robitaille, 2010; Dullemond, 2012) in the synthetic images of intensity and polarization.

4.4.4 Peel-off technique

The simplest approach to create intensity and polarization images of scattered light is to collect the photon packages leaving the grid in a certain direction on a detector. However, most of the photon packages do not leak from the grid with directions towards the observer and a huge amount of information is lost. This results in a bad signal-to-noise ratio. In order to overcome this weakness the peel-off technique was developed by Yusef-Zadeh *et al.* (1984). Here, at each scattering point a fraction of light is scattered in direction of the detector. The energy of the peel-off photon package E_{po} has to be adjusted by

$$E_{\text{po}} = E_{\text{pp}}F(\psi)\exp(-\tau_{\text{det}}) \quad (4.11)$$

where the probability of scattering in direction of the detector is determined by the phase function $F(\psi)$ and the angle ψ is between direction of propagation of the photon package and detector orientation. The optical depth τ_{det} is integrated along the line of sight between the position of the scattering event and the detector position. Although, the optical depth towards the observer has to be calculated for each scattering event, the peel-off technique results in synthetic images with an excellent signal-to-noise ratio even with a reduced number of photon packages.

4.4.5 Wavelength range selection

Stars and starfields emit photons in the full wavelength range of its black body SED which depends on their characteristic temperature. However, wavelengths at both ends of the SED can be neglected since they do not contribute significantly to the total emitted energy of the source. This reduces the number of wavelengths to be considered and subsequently the computational efforts.

4.5 Radiative transfer with non-spherical dust grains

4.5.1 RT equation for polarization

Even though the total ISM mass is mostly due to gas mass than dust, the contribution of dust to extinction is many orders of magnitude larger than that of the gas. In order to incorporate the full range of possible polarization mechanisms in the ISM we extend the contribution to light polarization because of scattering by the effects of dichroic extinction and re-emission of compact elongated dust grains aligned with the magnetic field lines. In contrast to spheres, irregular dust grains have different cross sections for light polarization parallel (C_{\parallel}) and perpendicular (C_{\perp}) to the particles alignment axis resulting in linear polarization and circular polarization. Previously unpolarized light can now additionally gain polarization by passing irregular grains due to preferential extinction and thermal re-emission, respectively. Therefore, the polarized light carries with it the information about the projected configuration of the magnetic field and the local dust parameters along the line of sight.

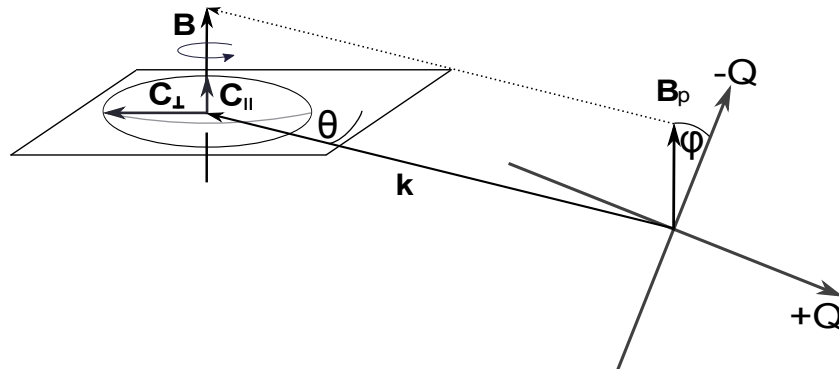


Figure 4.3: Geometrical configuration of the dust grains for the case of perfect alignment. The angle φ is defined by \mathbf{B}_p the projection of \mathbf{B} into the Q coordinate system of the Stokes vector and the inclination angle ϑ is made by the direction of propagation \mathbf{k} and the plane of rotation perpendicular to \mathbf{B} .

The analytical approach to calculate those contributions is to apply the Stokes vector formalism to the RT equation (see Sect. 2.1.1 and Sect. 2.1.3). Subsequently, one obtains for the extinction a system of equations in matrix form as presented in Martin (1974) with:

$$\frac{d}{dl} \begin{pmatrix} I \\ Q \\ U \\ V \end{pmatrix} = -n_d \begin{pmatrix} \bar{C}_{\text{ext}} & \Delta\bar{C}_{\text{ext}} & 0 & 0 \\ \Delta\bar{C}_{\text{ext}} & \bar{C}_{\text{ext}} & 0 & 0 \\ 0 & 0 & \bar{C}_{\text{ext}} & \Delta\bar{C}_{\text{circ}} \\ 0 & 0 & \Delta\bar{C}_{\text{circ}} & -\Delta\bar{C}_{\text{ext}} \end{pmatrix} \begin{pmatrix} I \\ Q \\ U \\ V \end{pmatrix} + n_d B_\lambda(T_d) \begin{pmatrix} \bar{C}_{\text{abs}} \\ \Delta\bar{C}_{\text{abs}} \\ \Delta\bar{C}_{\text{abs}} \\ 0 \end{pmatrix}. \quad (4.12)$$

In this chapter \bar{X} denotes the averaging over grain size distribution and $\langle X \rangle$ over orientation. The matrix is similar to that of the scattering problem but contains now the cross sections of extinction \bar{C}_{ext} and absorption \bar{C}_{abs} , the cross sections for linear polarization because of extinction $\Delta\bar{C}_{\text{pol}}$ and thermal re-emission $\Delta\bar{C}_{\text{abs}}$ as well as the cross sections for circular polarization $\Delta\bar{C}_{\text{circ}}$. For the definition of the cross section of circular polarization see Sect. 2.3.

Here, the characteristic of the re-emitted light is dependent on the magnetic field direction, the absorption properties and the geometry of the dust grains. The angle of maximum re-emission is perpendicular to the magnetic field. In contrast to scattering as introduced in Sect. 2.2.4 the reference frame is now determined by the magnetic field. For this reason, the coordinate system of the Stokes vector has to be aligned with the magnetic field direction for every interaction event by applying the rotation matrix (see Eq. 2.24).

The matrix of cross sections in Eq. 4.12 consists of two sub-matrices. Hence, the RT problem of polarization can be separated into two independent equation systems (Whitney & Wolff, 2002). For the definition of the angle φ see Fig. 4.3. The first equation system can simply be solved by substitution and it describes the resulting Stokes parameters of intensity I' polarization Q' by dichroic extinction and thermal re-emission after each radiation-dust interaction with

$$I' = (I + Q) e^{-n_d l (\bar{C}_{\text{ext}} + \Delta\bar{C}_{\text{ext}})} + n_d l B_\lambda(T_d) [\bar{C}_{\text{abs}} + \Delta\bar{C}_{\text{abs}} \cos(2\varphi)] \quad (4.13)$$

and

$$Q' = (I - Q) e^{n_d l (\Delta\bar{C}_{\text{ext}} - \bar{C}_{\text{ext}})} - n_d l B_\lambda(T_d) [\bar{C}_{\text{abs}} + \Delta\bar{C}_{\text{abs}} \cos(2\varphi)]. \quad (4.14)$$

The second system of equations can be solved with a complex eigenvalue approach and describes the resulting transfer of linear polarization into circular polarization and vice versa with

$$U' = e^{-n_d l \bar{C}_{\text{ext}}} [U \cos(n_d l \Delta\bar{C}_{\text{circ}}) - V \sin(n_d l \Delta\bar{C}_{\text{circ}})] + n_d l \Delta\bar{C}_{\text{abs}} B_\lambda(T_d) \sin(2\varphi) \quad (4.15)$$

and

$$V' = e^{-n_d l \bar{C}_{\text{ext}}} [U \sin(n_d l \Delta \bar{C}_{\text{circ}}) - V \cos(n_d l \Delta \bar{C}_{\text{circ}})]. \quad (4.16)$$

Consequently, un-polarized light can just gain circular polarization in the case of non-parallel magnetic field lines along the line of sight. For parallel magnetic field lines, light accumulates just polarization in the Q' parameter while U' and V' remain zero. Consequently, the degree of circular polarization is a measurement for the turbulence of the magnetic field morphology.

In Eq. 4.12 the required matrix of cross sections depends on grain size, orientation, and wavelength. The matrix elements are determined by the values along the minor axis (C_{\perp}) and major axis (C_{\parallel}) of the dust grain. In the case of perfectly (PA) aligned dust grains the cross sections of extinction and linear polarization of oblate dust grains are only dependent on the two angles defined by the direction of the incident light ϑ and the orientation of the coordinate system ϕ of the Stokes vector both with respect to the direction of the magnetic field \vec{B} (see Fig. 4.3) and can be calculated for each dust grain size by

$$C_{\text{ext}} = \frac{1}{2} [C_{\text{ext},\perp} + C_{\text{ext},\parallel} + (C_{\text{ext},\perp} - C_{\text{ext},\parallel}) \cos^2(\vartheta)] \quad (4.17)$$

and

$$\Delta C_{\text{ext}} = \frac{C_{\text{ext},\perp} - C_{\text{ext},\parallel}}{2} \sin^2(\vartheta). \quad (4.18)$$

However, PA of the dust grains does not take into consideration the wobbling of grains because of the local physical conditions of the ISM and remains an ideal approximation which would result in an unrealistically high degree of linear polarization. Usually this problem is circumvented by modeling cross sections of the dust and the alignment efficiencies by a single parameter to adjust the degree of linear polarization to observational data (e.g. Fiege & Pudritz, 2000). However, this is without any physical motivation. The Rayleigh reduction factor R (see Sect. 4.5.2) is a measurement for the grain alignment efficiency and for realistic situations the cross sections have to be adjusted by

$$C_x = \langle C_{\text{ext}} \rangle + \frac{1}{3} R \times (C_{\parallel} - C_{\perp}) \quad (4.19)$$

and

$$C_y = \langle C_{\text{ext}} \rangle + \frac{1}{3} R \times (C_{\parallel} - C_{\perp}) (1 - 3 \sin^2(\vartheta)) \quad (4.20)$$

where x and y stand for the directions perpendicular and parallel to the magnetic field lines and $\langle C_{\text{ext}} \rangle$ is the contribution of randomly aligned dust grains. For oblate

dust grains, the cross sections can simply be calculated by $C_{\text{ext}} = 0.5(C_{\text{ext},x} + C_{\text{ext},y})$, $\Delta C_{\text{ext}} = 0.5(C_{\text{ext},x} - C_{\text{ext},y})$, and $\langle C_{\text{ext}} \rangle = (2C_{\text{ext},\parallel} + C_{\text{ext},\perp})/3$. Because of its $\sin^2(\vartheta)$ dependency, the dust grain appears to be spherical for an inclination angle of $\vartheta = 0^\circ$ and the cross section of extinction disappears. Consequently, the magnetic field morphology can not be deduced from polarization measurements in areas where the line of sight is parallel to the magnetic field direction.

So far, the cross sections are calculated for a single dust grain species with a distinct size. Dependent on the considered astrophysical environment the dust is a composition of dust grain sizes following a size distribution $n(a)$ with a minimal dust grain size a_{min} and a maximal dust grain size a_{max} . Finally, in order to calculate the average dust grain cross sections of extinction and linear polarization one has to weight the dust grains accordingly over the grain size distribution $n(a)$ with

$$\bar{C}_{\text{ext}} = \sum_i \chi_i \times \int_{a_{\text{min}}}^{a_{\text{max}}} C_{\text{ext}} n(a) da \quad (4.21)$$

and

$$\Delta \bar{C}_{\text{ext}} = \sum_i \chi_i \times \int_{a_{\text{min}}}^{a_{\text{max}}} \Delta C_{\text{ext}} n(a) da \quad (4.22)$$

where χ_i is the fraction of the different dust grain materials. Exactly the same calculations apply for the cross sections of absorption and circular polarization. This means, that the cross sections in Eq. 4.12 are fully determined once the dust grain properties are defined and the Rayleigh reduction factor R is calculated.

In each cell of our model space we have the two opposing effects of dichroic extinction and thermal re-emission adding to the linear polarization perpendicular to each other. In the reference frame of the magnetic field the dichroic extinction provides a negative contribution to the Stokes Q parameter while thermal re-emission contributes positively. It is possible to determine the exact conditions for the 90° flip in a single cell of the model space. Unfortunately, a threshold for this effect does not exist along the entire line of sight. In this orientation the U and V parameter remain zero. If we solve equation 4.14 for the Q_{i+1} parameter, we can calculate the conditions when the two effects cancel each other out:

$$Q_{i+1} = e^{-n_i \times l_i C_{\text{ext},i}} [Q_i \cosh(n_i l_i \Delta C_{\text{ext},i}) - I_i \sinh(n_i l_i \Delta C_{\text{ext},i})] = 0. \quad (4.23)$$

The contribution of thermal re-emission is determined by the temperature of the dust T_d , the number density n_d , the cross sections for absorption ΔC_{abs} , C_{abs} and the path length l . Inside each cell all the parameters and functions n_d , l , ΔC_{abs} , C_{abs} , C_{ext} , $B_\lambda(T)$

are positive and constant, so one can solve Eq. 4.23. As we can see from Eqs. 4.13 and 4.14, the contributions of I_i and Q_i in a single cell are as followed:

$$I_i = n_i \times l_i C_{\text{abs},i} B_\lambda(T_i) \quad (4.24)$$

and

$$Q_i = n_i \times l_i \Delta C_{\text{abs},i} B_\lambda(T_i). \quad (4.25)$$

For a wavelength of $\lambda > 7 \mu\text{m}$ one can approximate $C_{\text{abs},i} \approx C_{\text{ext},i}$. By introducing the optical depths for extinction

$$\tau_{\text{ext},i} = n_i \times l_i C_{\text{ext},i} \quad (4.26)$$

and polarization

$$\tau_{\text{pol},i} = n_i \times l_i \Delta C_{\text{ext},i} \quad (4.27)$$

we can derive an inequality for the Q parameter to change its sign as a function of the inverse hyperbolic tangent:

$$1 \leq \frac{1}{\tau_{\text{ext}}} \tanh^{-1} \left(\frac{\tau_{\text{pol}}}{\tau_{\text{ext}}} \right). \quad (4.28)$$

If the right-hand side is larger than unity, the polarization process is dominated by thermal re-emission and, in the reverse case, by dichroic extinction. However, in the calculated synthetic polarization maps the observed flip of 90° for the orientation of linear polarization depends on all the physical quantities along the entire line of sight and cannot be determined with this inequality.

4.5.2 Grain alignment: Analytical solutions and approximations

The Rayleigh reduction factor R (Greenberg, 1968) was introduced as a measurement to quantify the imperfect alignment of dust grains and is defined as:

$$R = \langle G(\cos^2(\beta)) G(\cos^2(\zeta)) \rangle. \quad (4.29)$$

As introduced before, ζ is the angle between the axis of the largest moment of inertia $I_{||}$ and the angular momentum \vec{J} and represents the II alignment (see Sect. 3.3.2.3). Furthermore, β is the angle between \vec{J} and magnetic field \vec{B} and is determined by the applied grain alignment theory, while $G(x) = 1.5x - 0.5$. The Rayleigh reduction factor

is in $R \in [-0.5; 1]$ where positive values correspond to an alignment with the longer grain axis perpendicular to the magnetic field direction and for negative values vice versa. Note that the Rayleigh reduction factor can also be a function of wavelength and effective radius and is dependent on the considered grain alignment mechanism. Hence, grain alignment and, subsequently, polarization is completely determined by first order moments weighted over a distribution function $f(x)$ so that $\langle \cos^2(x) \rangle = \int f(x) \sin(x) dx$. Unfortunately, grain alignment and the corresponding internal alignment do not work independently. For exact solutions a simultaneous integration over both distribution functions ($f(\beta)$ and $f(\zeta)$) is required. However, exact calculations are required for each photon-dust interaction resulting in a further burden because numerical integration is one of the challenges to perform MC RT simulations in reasonable time. Dependent on the considered grain alignment mechanisms, the distribution functions in turn are also functions of density, temperature, magnetic field strength, velocity and direction of the incident light (see Sect. 3.3.2.1, Sect. 3.3.2.2 and Sect. 3.3.2.1). Because of this enormous parameter space, the reduction in polarization can not be pre-calculated without loosing an enormous amount of precision. Therefore, we approximate

$$\langle G(X)G(Y) \rangle \approx \langle G(X) \rangle \times \langle G(Y) \rangle (1 + f_c) \quad (4.30)$$

with a correlation factor f_c where $f_c = 0$ stands for no correlation (see Roberge & Lazarian, 1999; Hoang *et al.*, 2014). Since the correlation factor is of minor influence for physical parameters typical for the ISM, we apply a value of $f_c = 0.6$ in this thesis. Once, the Rayleigh reduction factor is decoupled, the challenge is to determine the analytical solution of each grain alignment mechanism separately.

4.5.2.1 Analytical solution of II alignment

Analytical solution for IDG and GOLD alignment are available. However, the II requires still numerical integration over angular momentum J and cone angle β . Taking the effects of gas-grain collisions into consideration, a solution to this problem can be found with an approach using the Focker-Planck equation. However, the coefficients need to be numerically calculated for each new set of parameters. This approach is therefore not suitable for MC RT simulations in reasonable time scales. Lazarian & Roberge (1997a) presented an approximation by estimating the average angular momentum of a dust grain for a given set of parameters with $J = \gamma J_{\text{eff}}$. The parameter γ adjusts the approximation solution to the results of the numerical calculations. As it turns out a value of $\gamma = 1$ is in good agreement with the numerical solution throughout the entire parameter space. The exact value of J_{eff} , however, is dependent on grain alignment theory and must be calculated individually. This approach delivers reliable values in the limit of thermal equilibrium ($T_d/T_g = 1$), however, slightly underestimates the internal

alignment for $s < 0.5$ and $T_d/T_g < 0.2$ (see Fig. 4.4 left side). Once the effective angular momentum J_{eff} is known, the distribution function of II alignment can be rewritten as

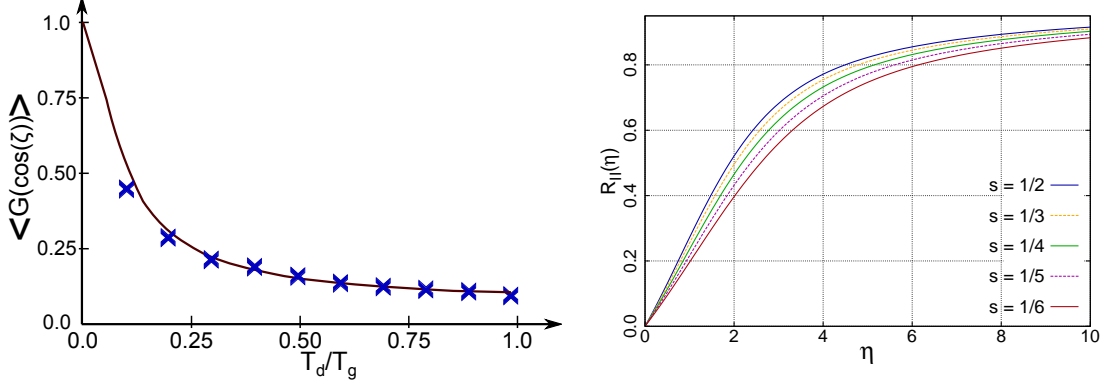


Figure 4.4: Left panel: First order moment of the imperfect internal alignment angle ζ as a function of dust temperature T_d to gas temperature T_g . The numerical solution is the black line while the $\gamma = 1$ - approximation is marked with blue crosses. Right panel: Rayleigh reduction factor R_{II} of the internal alignment over the substituted parameter η for different aspect ratios.

$$f_{\text{II}}(\zeta) \approx \exp(-\eta [1 + \delta \sin^2(\zeta)]) \quad (4.31)$$

with

$$\eta = J_{\text{eff}}^2 / 2I_{\parallel} k_B T_d. \quad (4.32)$$

The quantity δ is defined by the moment of inertia and, subsequently, the aspect ratio s with:

$$\delta = I_{\parallel} / I_{\perp} - 1 = h - 1 = \frac{2}{1 + s^2}. \quad (4.33)$$

In order to calculate the contribution of internal alignment one has still to solve the integration over internal alignment angle ζ with

$$R_{\text{II}} = \langle G(\zeta) \rangle = \frac{\int_0^{\pi} G(\zeta) \sin(\zeta) f_{\text{II}}(\zeta) d\zeta}{\int_0^{\pi} \sin(\zeta) f_{\text{II}}(\zeta) d\zeta} \quad (4.34)$$

at each point of interaction. However, with the substitution of $x = \eta \times \delta$ the integral can be solved and the degree of internal alignment can then exactly be calculated with the use of the complex error function $\text{erfi}(x)$:

$$\langle G(\cos^2(\zeta)) \rangle(x) = \frac{e^x}{\sqrt{\pi x} \times \text{erfi}(\sqrt{x})} - \frac{1}{2x} \quad (4.35)$$

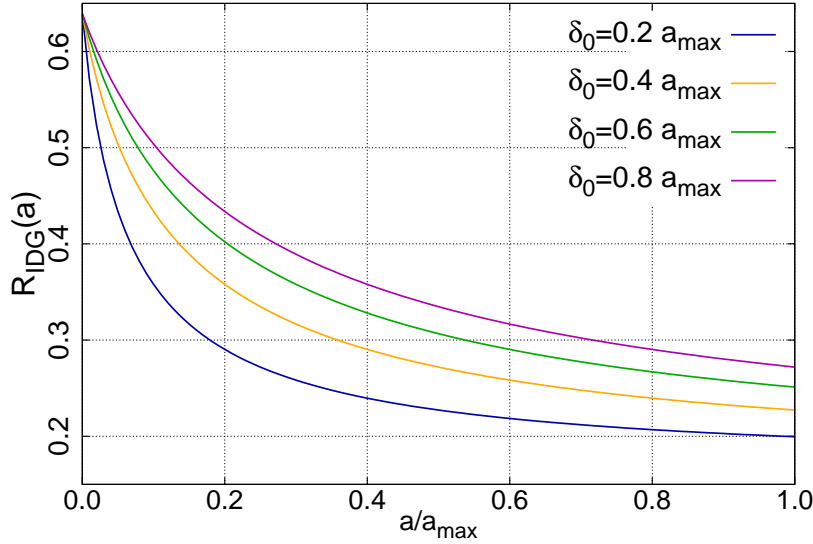


Figure 4.5: Rayleigh reduction factor R_{IDG} of IDG alignment over a normalized dust grain size distribution for oblate grains with different upper thresholds δ_0 .

The complex error function can easily be pre-calculated and interpolated. Obviously, $\lim_{x \rightarrow +\infty} \langle G(\cos^2(\zeta)) \rangle(x) = 1$ when internal alignment is taken into account. This is consistent with physics because in the supra-thermal regime ($J^2 \gg J_{\text{th}}^2 \approx 2I_{\parallel} k_B T_d$) and for disk like dust grains ($\delta \rightarrow 1$) internal alignment becomes irrelevant (see Lazarian, 1996; Lazarian & Roberge, 1997a). For $x \rightarrow 0$ the first order moment $\langle G(\cos^2(\zeta)) \rangle(x)$ remains positive and polarization vectors can also not change their sign in IDG or RAT alignment as a result of imperfect internal alignment (see also Fig. 4.4 left side).

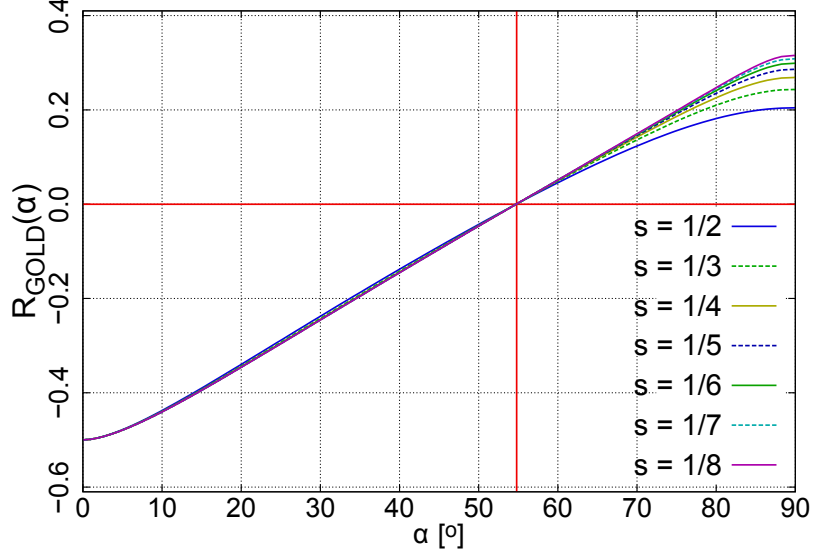
4.5.2.2 Analytical solution of IDG alignment

By comparison of the ratio of the characteristic timescale of paramagnetic relaxation and gas-dust collisions a distribution function for IDG alignment was found solving the Fokker-Planck equation (see Spitzer & McGlynn, 1979) as shown in Sect. 3.3.2.1. Later, an analytical solution for the first order moment $\langle \cos^2(\beta) \rangle$ was derived in Aannestad & Greenberg (1983). This allows to calculate

$$\langle \cos^2(\beta) \rangle = \left(1 - \sqrt{\frac{\xi^2(a)}{1 - \xi^2(a)}} \right) \arcsin \frac{\sqrt{1 - \xi^2(a)}}{1 - \xi^2(a)} \quad (4.36)$$

Figure 4.6:

Rayleigh reduction factor R_{GOLD} of GOLD alignment over angle α between predominant direction of the gas stream and the magnetic field direction for oblate grains with different aspect ratios. The angle $\alpha \approx 54^\circ$ of totally randomized dust grains is independent of aspect ratio.



and subsequently the Rayleigh reduction factor. The IDG can not flip the polarization angle since $\cos^2(\beta) > 1/3$ for any combination of physical parameters. In order to calculate the internal alignment we use the approximation from Lazarian & Roberge (1997a) for the angular momentum

$$J_{\text{eff}}^2 \approx \sqrt{(1 + 0.5s^{-2})(1 + T_d/T_g)} \times J_{\text{th}}^2 \quad (4.37)$$

where $J_{\text{th}}^2 \approx 2I_{\parallel}k_B T_g$ is the angular momentum obtained from gas-dust collisions and s is the aspect ratio of the grains.

4.5.2.3 Analytical solution of GOLD alignment

A distribution function for the cone angle β was derived by Dolginov & Mitrofanov (1976a). For spheroidal dust grains, the first order moment $\langle \cos^2(\beta) \rangle$ is completely defined by the anisotropy in the gas stream s and the grain non-sphericity g (see Eq. 3.25 and Eq. 3.26). In the case of oblate dust grains g is negative (Lazarian, 1994) and

$$\langle \cos^2(\beta) \rangle = \begin{cases} \frac{\sqrt{-g} \arcsin(\sqrt{-s/(1+g)})}{s \arctan \sqrt{sg/(1+s+g)}} - 1/s & \text{if } s < 0 \\ \frac{\sqrt{-g} \sinh^{-1}(\sqrt{s/(1+g)})}{s \tanh^{-1}(\sqrt{-sg/(1+s+g)})} - 1/s & \text{if } s > 0 \end{cases} \quad (4.38)$$

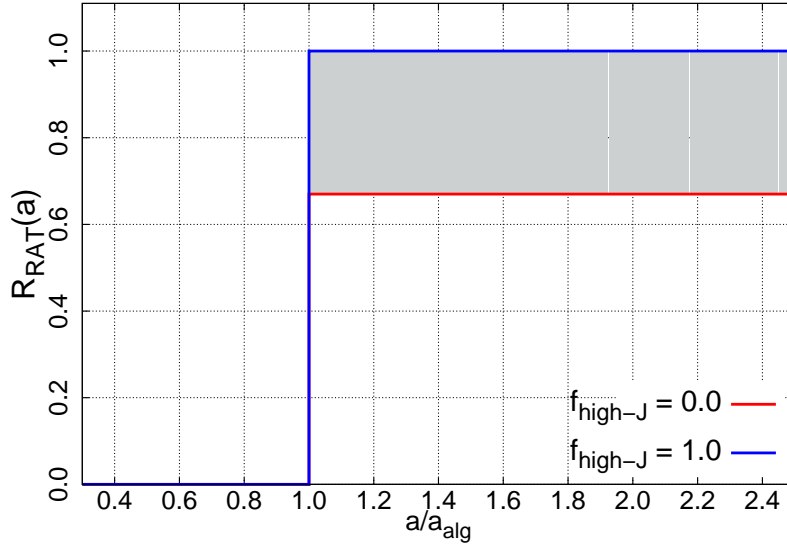


Figure 4.7: Rayleigh reduction factor R_{RAT} of RAT alignment over a dust grain size distribution normalized over the critical size a_{alg} for oblate grains. Since the quantity $f_{\text{high-J}}$ remains a free parameter the R_{RAT} can be fine tuned to be in the gray area.

Here, the Rayleigh reduction factor is independent of wavelength and grain size. The polarization can change sign for an angle α between magnetic field and predominant gas stream lower as 54° (see Fig. 3.4). For other grain shapes we refer to Lazarian (1996).

Following Lazarian (1997) for the internal alignment, the effective angular momentum can be approximated by

$$J_{\text{eff}}^2 \approx k_{\text{B}} I_{\parallel} (2/h + 1) \left(\frac{T_{\text{g}} + T_{\text{d}}}{2} + \frac{\mu m_{\text{H}} v_{\text{g}}^2}{6k_{\text{B}}} \right) \quad (4.39)$$

with the mass μm_{H} of a gas molecule and $h = I_{\parallel}/I_{\perp}$.

4.5.2.4 Approximation of RAT alignment

For the RAT alignment mechanism to work, the dust grains must be able to rotate super thermally (see Sect. 3.3.2.4). To determine the parameters of supra-thermal rotation it is necessary to calculate the anisotropy factor γ_{λ} .

The values of the anisotropy factor γ_{λ} and the mean energy density \bar{u}_{λ} of the radiation field are acquired by a RT MC approach where we store the energy density direction \vec{u}_{λ} in each cell. Here, we consider all radiation sources including thermal dust re-emission.

Following Lucy (1999) for the mean energy density per path length and wavelength we use Eq. 2.20. This allows to calculate the mean energy density in the case of discrete wavelength

$$\bar{u}_\lambda = \sum_{i=1}^{N_{\text{ph}}} |\vec{u}_{\lambda,i}| \quad (4.40)$$

and the anisotropy parameter determined by

$$\gamma_\lambda = \frac{\left| \sum_{i=1}^{N_{\text{ph}}} \vec{u}_{\lambda,i} \right|}{\sum_{i=1}^{N_{\text{ph}}} |\vec{u}_{\lambda,i}|} \in [0; 1]. \quad (4.41)$$

At the current stage of its development no analytical function for the distribution of the cone angle β is available. While PA can be assumed at both high-J and low-J attractor points, internal alignment is just given for supra-thermally rotating grains. At low-J the angular momentum can be assumed to be thermal (Hoang & Lazarian, 2009). This means that $J_{\text{th}} \approx \sqrt{2I_{\parallel} k_B T_d}$ and the distribution of internal alignment (see Eq. 3.27) becomes a function of grain geometry alone because of the parameter $\eta = 1$ (see Eq. 4.32).

Now, for the Rayleigh reduction factor only the moment $\langle G_{\text{low-J}}(\cos^2(\zeta)) \rangle$ remains of relevance. When we consider $f_{\text{high-J}}$ to be the fraction of dust grain aligned at the high-J attractor point the Rayleigh reduction factor is:

$$R = \begin{cases} (1 - f_{\text{high-J}}) \langle G_{\text{low-J}}(\cos^2(\zeta)) \rangle + f_{\text{high-J}} & \text{if } a \geq a_{\text{alg}} \\ 0 & \text{if } a < a_{\text{alg}} \end{cases}. \quad (4.42)$$

So far, $f_{\text{high-J}}$ can not exactly be determined (Hoang & Lazarian, 2007) and remains a free parameter.

For oblate dust grain with an aspect ratio of $s = 0.5$ the lower limit of the Rayleigh reduction factor is determined by $\langle G_{\text{low-J}}(\cos^2(\zeta)) \rangle \approx 0.67$. Consequently, the internal alignment of RAT theory is completely determined by parameters related to the dust grain geometry.

4.5.3 Combined effects of dust grain alignment

So far, none of the proposed alignment theories have observationally definitely been confirmed. Most likely all the considered processes resulting in grain alignment are not independently at work inside the ISM. To investigate this scenario *POLARIS* allows to combine several grain alignment mechanisms in a single 3D RT simulation. In order

to calculate a composite polarization map we use the approach suggested in Lazarian (1995) and generalize it to handle three different alignment mechanisms acting simultaneously on the dust grains:

$$R_{\Sigma} \approx \frac{R_{\text{IDG}} + R_{\text{RAT}} + R_{\text{GOLD}} + R_{\text{IDG}}R_{\text{RAT}} + R_{\text{IDG}}R_{\text{GOLD}} + R_{\text{RAT}}R_{\text{GOLD}} + 3R_{\text{IDG}}R_{\text{RAT}}R_{\text{GOLD}}}{1 + 2R_{\text{IDG}}R_{\text{RAT}} + 2R_{\text{IDG}}R_{\text{GOLD}} + 2R_{\text{RAT}}R_{\text{GOLD}} + 2R_{\text{IDG}}R_{\text{RAT}}R_{\text{GOLD}}}. \quad (4.43)$$

Here, it needs to be emphasized that its approach remains a first approximation and the accuracy of this approach is not yet confirmed. However, this estimated measure of a combined Rayleigh reduction factor R_{Σ} allows defensively a qualitative statement about the dominant mechanism of grain alignment and subsequently about the net polarization.

4.5.4 Limitations on magnetic field strength and velocity stream

Once, a dust grain starts to tumble in the presence of a magnetic field a Larmor precession acts on the grains due to the Barnett effect. For the RATs to work, the magnetic field strength has to be sufficiently high to resist misalignment by gas-dust interactions. This requires the characteristic time scale for Larmor precession (t_{L}) to be lower than the gas dumping time (t_{gas}): $t_{\text{L}} < t_{\text{gas}}$ which gives us a limit of

$$|\vec{B}| > 4.1 \times 10^{-9} a \frac{n_{\text{g}} \sqrt{T_{\text{g}} T_{\text{d}}}}{s^2} [\text{T}] \quad (4.44)$$

for the magnetic field strength (Hughes *et al.*, 2009; Hoang & Lazarian, 2009). This limitation is similar in nature to that of Eq. 3.16. Since the coupling mechanism with the magnetic field is also the Barnett effect, the same limitation for the field strength is applied to RT simulations with GOLD alignment.

For the supersonic velocity condition required by GOLD we locally calculate the Mach number in each cell

$$M = \frac{v}{\sqrt{k_{\text{B}} T_{\text{g}} / \mu m_{\text{H}}}} \quad (4.45)$$

and demand $M > 1$. Otherwise, the GOLD alignment is considered to be insufficient to contribute to the net polarization.

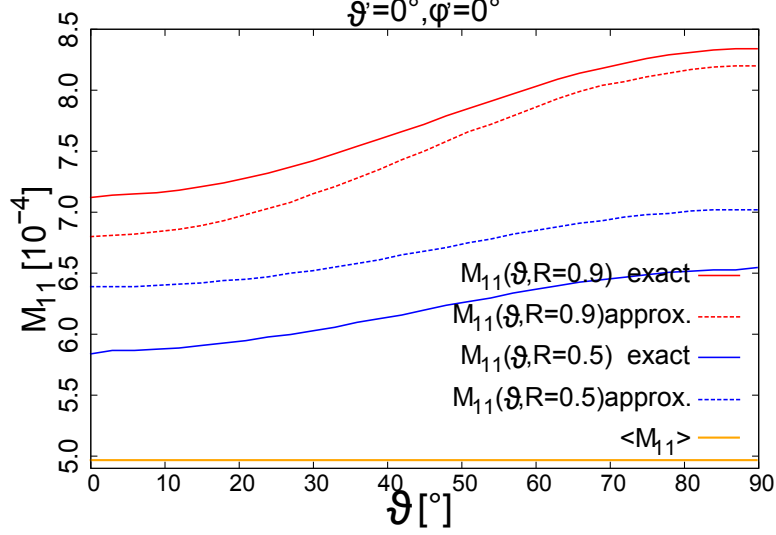


Figure 4.8: Plots of the scattering matrix component M_{11} of an oblate averaged sized wobbling dust grain ($a \in [5 \text{ nm} - 250 \text{ nm}]$) as a function of incident angle ϑ corresponding to two different Rayleigh reduction factors ($R = 0.9$ in red lines and $R = 0.5$ in blue lines). Scattering is in forward direction ($\vartheta' = 0^\circ$, $\varphi' = 0^\circ$). Dotted lines are approximated by Eq. 4.46. The M_{11} component of a randomly orientated dust grain is shown in dark yellow. Solid lines are exact solutions integrated over the IDG cone angle distribution with Eq. 4.48.

4.5.5 Scattering on partially aligned dust grains

For scattering from one direction to a new direction the Stokes vector S is modified via a scattering matrix (see Sect. 2.2.4). The calculation of the new direction after the scattering event requires wavelength and grain size dependent asymmetry factor g for the HGphase function or, alternative, the M_{11} element of the scattering matrix. Both possibilities are fully supported by *POLARIS*.

The scattering matrix elements and the asymmetry factor g can be calculated with the assumption of either spherical dust grains with Mie theory or with *DDSCAT* for spheroidal but PA dust grains. Here, we face the same problem as for the calculation of cross sections in Sec. 2.3. For imperfectly aligned wobbling dust grains the angles of incident light (ϑ, φ) and the scattering angles (ϑ', φ') are now functions of the alignment angles β and ζ , respectively. This which increases the dimensionality of the scattering problem dramatically. In order to obtain a scattering matrix for an average sized dust grain

one has to integrate the functions $f(\beta)$ for alignment, $f(\zeta)$ for internal alignment, and the size distribution $n(a)$ over β , ζ as well as a simultaneously. The exact distribution function for RAT alignment is still missing and solving the exact integrals for GOLD or IDG alignment would push exact 3D RT MC simulations again beyond accessibility for current computer equipment. In order to take care of scattering on non-spherical imperfectly aligned dust grains we apply the following approximation:

$$\hat{M}_{ij}(\lambda, R, a, \vartheta, \varphi, \vartheta', \varphi') \approx R \times \hat{M}_{ij}(a, \lambda, \vartheta, \varphi, \vartheta', \varphi') + (1 - R) \langle \hat{M}_{ij}(a, \lambda, \vartheta', \varphi') \rangle. \quad (4.46)$$

The same approximation is used for the orientation and sizedependent asymmetry parameter g of the HGPhase function (see Eq. 2.28):

$$g(\lambda, R, a, \vartheta, \varphi) \approx R \times g(a, \lambda, \vartheta, \varphi) + (1 - R) \langle g(a, \lambda, \vartheta, \varphi) \rangle \quad (4.47)$$

where the brackets $\langle \rangle$ indicate randomly aligned dust grains. With increasing efficiency in dust grain alignment the Rayleigh reduction factor reaches unity and the dust grains and the contribution of randomly aligned dust grains diminish. *POLARIS* uses this approximation at each scattering event.

In Fig. 4.8 we show a comparison of an exact averaging calculation and the approximation of Eq. 4.46 in the exemplary case of IDG alignment and the \hat{M}_{11} component of the scattering matrix. The averaging calculations over grain size and opening angle were performed according to Voshchinnikov & Das (2008) and Das *et al.* (2010) with

$$\hat{M}_{ij}(\lambda, R, a, \vartheta, \varphi, \vartheta', \varphi') = \frac{4}{\pi^2} \int_{a_{\max}}^{a_{\max}} \int_0^{\frac{\pi}{2}} \int_0^{\frac{\pi}{2}} \hat{M}_{ij}(a, \lambda, \vartheta', \varphi') n(a) f_{\text{DG}}(\xi(a), \beta) d\Omega d\beta da \quad (4.48)$$

where the Rayleigh reduction factor is implicitly in this equation by averaging over the cone angle distribution function $f_{\text{DG}}(\xi(a), \beta)$ (see Eq. 3.17 and compare Fig. 3.2). Here, the internal alignment was considered to be perfect. This result is quite similar for applying GOLD alignment theory. The approximated solutions can deviate from the exact solution by up to 20 %. However, this is an improvement in accuracy in comparison with the common approach of considering scattering on partially aligned dust grains to be randomly orientated dust grains.

In *POLARIS* we use optionally the inverted phase function as presented in Henyey & Greenstein (1941).

$$\cos(\vartheta') = \begin{cases} \frac{1}{2g} \left[1 + g^2 - \left(\frac{1-g^2}{1-g+2g \times z} \right) \right] & \text{if } g \neq 0 \\ 1 - 2 \times z & \text{if } g = 0 \end{cases} \quad (4.49)$$

$$\varphi' = 2\pi \times z \quad (4.50)$$

The probability distribution of scattering is described by one parameter, the anisotropy $g = \langle \cos(\vartheta') \rangle \in [-1, 1]$, $g = 0$ means isotropic scattering, $g = -1$ backward scattering, and $g = 1$ forward scattering, respectively. The anisotropy parameter is pre - calculated with DDSCAT (Draine & Flatau (2013), see also Eq. 2.48) and is a function of grain size, grain orientation and wavelength. Although alternative phase functions are currently discussed (see Sharma & Roy, 2008), the HG phase function still provides a good approximation for the scattering probability. During all dust heating calculations, the dust grain orientation is assumed to be random.

4.5.6 Radiative heating of non-spherical dust grains

In *POLARIS* we use a hybrid approach to calculate the temperature of the dust grains. The dust temperature is calculated by the energy radiation deposited in a cell per unit time along its path by use of the continuous absorption technique (see Sect. 2.2.5.2). However, we apply no iteration but correct the temperature after each absorption event immediately as introduced in Sect. 2.2.5.1. The photon package is then re-emitted in a random direction calculated similar to 2.2.4.1 with a wavelength sampled by Eq. 2.33 to remain in thermal equilibrium. *POLARIS* handles the dust parameter of each dust component separately. Each component has its own characteristic sublimation temperature where the dust grain starts to evaporate. This sublimation temperature is material dependent. When the dust temperature exceeds the sublimation temperature of a certain material, this component will be removed from the cell and will also no longer be considered in the following dust heating and polarization MC RT simulations.

The challenge of RT dust heating is that for the input data a temperature can already have been calculated. With temperatures resulting from MHD simulations we have to deal with two effects of dust heating: The RT heating because of radiation sources and the MHD heating because of compression and gas-dust interaction (for details we refer to Banerjee *et al.*, 2006; Krumholz *et al.*, 2007). However, both temperatures are equally physically well-motivated and cannot simply be added up. Originally, the algorithm of the continuous absorption technique assumes the energy content of a certain cell to be empty at the beginning of the radiative heating process. As a first step the rate of re-emitted energy (see Eq. 2.35) for the entire ensemble of dust grain sizes is pre-calculated and interpolated as a function of dust temperature. Using

$$\dot{E} = \frac{\epsilon_0}{\Delta t} \sum_i C_{\text{abs},\lambda_i}(a) \times l_i + \Delta \dot{E} \quad (4.51)$$

we extend the equation of continuous absorption with an offset $\Delta\dot{E}$ (see Eq. 2.35) in the absorbed energy. Since the cross sections of absorption C_{abs} are completely defined by the applied dust model, we make use of a reverse calculation to determine $\Delta\dot{E}$ for an ensemble of dust grains with the help of the pre-calculated values of $j(a, T_d)$ and, subsequently, the initial dust temperature. We refer to this method as „offset dust heating“ in the following.

The consideration of both temperatures leads to a shift in the profitability distribution of the wavelengths of re-emission (see Eq. 2.33 and Fig. 4.2) towards shorter wavelength. In this regime of wavelength the absorption of radiation is more effective because of higher cross sections of absorption $C_{\text{abs},\lambda}$ (see Fig. 4.9 top row). This results in a net temperature higher than the single temperatures alone which would not have been the case by simply adding up the temperatures resulting from RT and MHD simulations.

4.6 Dust grain database

Technically, the dust grain database is not part of the *POLARIS* code. However, it provides the pre-calculated input parameters necessary for the MC RT calculations. The interpretation of observational polarization data is usually limited by the parameters of the underlying dust grain models. A satisfactory model reproducing the galactic extinction curve is the so called MRN (Mathis, Rumpl, & Nordsieck, 1977) model. It is a three parameter model with a power-law size distribution $n(a) \propto a^{-q}$ and a dust grain size range of $a \in [a_{\text{min}} : a_{\text{max}}]$ with values of $q = -3.5$, $a_{\text{min}} = 5$ nm, and $a_{\text{max}} = 250$ nm typical for ISM dust. The dust is usually a mixture of materials with 62.5 % astro-silicate (olivine, $(Fe, Mg)_2SiO_4$) and 37.5 % graphite. Later, the upper limit was expected to be of μm -size (e.g. Clayton *et al.*, 2003; Draine & Li, 2007). The assumption of dust grains with a range of dust grain radii from about ≈ 10 nm to radii of several ≈ 100 nm is well constraint for the ISM. However, all the observations show clear evidence that grains in circumstellar disks and outflow environments differ significantly from grains in the diffuse ISM. Grain growth in the disk is expected to enrich the surrounding environment with dust grain sized of up to millimeter-sized dust grains. For dust grains up to $a = 2 \mu\text{m}$ we used the DDA code DDSCAT 7.3 (Draine & Flatau, 2013) and approximated oblate shape dust grains by defining a regular lattice with 171,500 distinct dipoles and an error tolerance of 8.5×10^{-3} . For the astro-silicate and graphite we used the refractive indices of Weingartner & Draine (2000), and applied the 1/3 – 2/3 approximation to take care of the anisotropic graphite structure (Draine & Malhotra, 1993). In order to overcome the numerical limitations of DDSCAT (see Sect. 2.3) concerning dust grain size we combined the optical dust properties from DDSCAT with data obtained by the *MIEX* code (Wolf & Voshchinnikov, 2004). *MIEX* is a program that calculates the

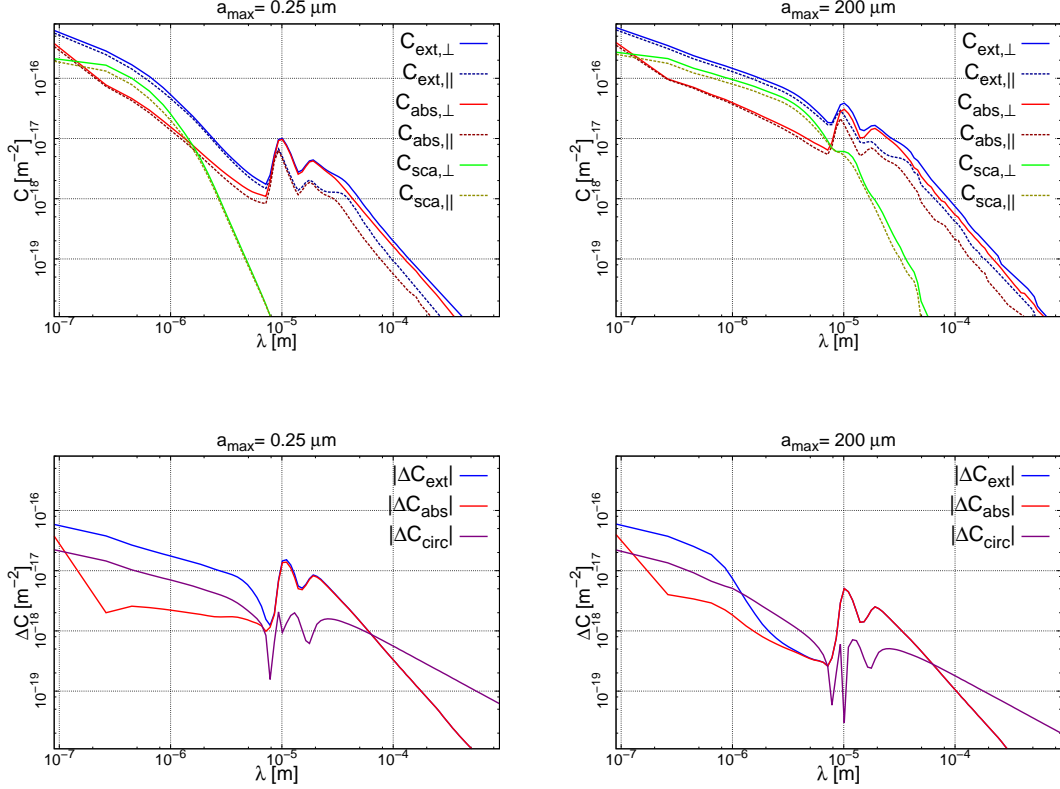


Figure 4.9: Resulting cross sections over wavelength weighted for a size distribution $n(a)$ from $a_{\max} = 5 \text{ nm}$ to $a_{\max} = 0.25 \mu\text{m}$ (left panels) and $a_{\max} = 0.200 \mu\text{m}$ (right panels), respectively.

optical properties of spherical dust grains using Mie scattering theory. The cross section of linear and circular polarization ΔC_{ext} , ΔC_{abs} , and ΔC_{circ} as well as the cross sections of scattering C_{sca} approach zero for increasing dust grain sizes. Hence, larger dust grains with radii $a > 2 \mu\text{m}$ can be assumed to be insignificant to polarization and scattering. We pre-calculated the cross sections of extinction C_{ext} and absorption C_{abs} with the *MIEX* for dust grains with radii $a \in [2 \mu\text{m} : 2 \text{mm}]$. The efficiency of RAT alignment $Q_{\Gamma}(\varepsilon)$ can not be pre-calculated with *MIEX*. However, $Q_{\Gamma}(\varepsilon)$ follows for $\frac{\lambda}{a} \gg 1$ a power-law distribution (Cho & Lazarian, 2007) with

$$Q_{\Gamma}(\varepsilon) = Q_{\Gamma, \max} \sin(\varepsilon) = \left(\frac{\lambda}{a} \right)^{-\rho} \sin(\varepsilon) \quad (4.52)$$

where $Q_{\Gamma, \max}$ and ρ are fit parameter for extrapolation. With this additional data from *MIEX* we smoothly extend our *DDSCAT* dust model up to an upper cut-off radius of

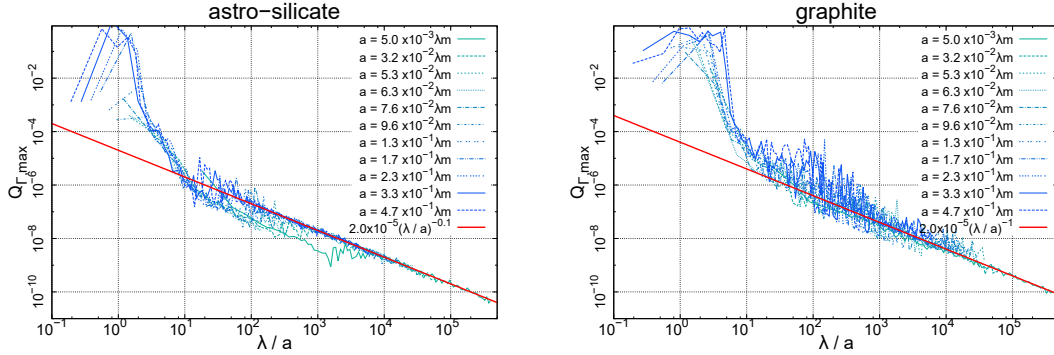


Figure 4.10: Resulting alignment efficiencies according to RAT theory over the ratio of wavelength to grain size for astro-silicate (right panel) and graphite (left panel), respectively, as material. The red line shows the fitted model for large dust grains.

$a_{\max} = 2$ mm for dust grains with 218 effective radii and 120 wavelengths logarithmically distributed between $a \in [5 \text{ nm} : 2 \text{ mm}]$ and $\lambda \in [90 \text{ nm} : 3 \text{ mm}]$, respectively. The best fit model is with $\rho = 1$ for both astro-silicate and graphite (see Fig. 4.10).

Since the grain materials have unique dielectric and paramagnetic properties this should also result in a difference alignment behavior. As it is shown in the left panel of Fig. 4.10 graphite can be effectively spun up by RATs. However, the analysis of observational linear polarization and circular polarization data shows that a higher alignment efficiency is to be expected for silicate grain while carbonaceous grains seem to be unaffected by the presence of a magnetic field (e.g Martin & Angel, 1976; Mathis, Rumpl, & Nordsieck, 1977; Mathis, 1986). Therefore, we consider graphite dust grains to be randomized in all the following MC RT simulations.

The choice of dust grain shape is limited by the considered alignment theories of GOLD, IDG, RAT, and II alignment, respectively. While the alignment behavior for arbitrary shapes can be calculated by means of numerical calculation, exact analytical solutions for the problem of grain alignment are just available for oblate shaped dust grains. Additionally, the heating of oblate and spherical dust grains is similar as long as the aspect ratio of minor axis to major axis is $s > 0.1$. Higher aspect ratios would result in higher peak values and more contrast in the maps of linear and circular polarization, but the dust heating can no longer be calculated by the procedure described in Sect. 4.5 and Sect. 4.5.6. The same problem arises for small dust grains with radii $a < 5$ nm. Such grains can be heated up by UV radiation to very high temperatures. Here, the assumption that dust grains remain in LTE with their environment can no longer be assumed (Draine & Li, 2001) and the dust temperature must be evaluated for each dust grain size

separately. Therefore, we chose a constant aspect ratio of $s = 0.5$ (Aannestad & Purcell, 1973; Hildebrand & Dragovan, 1995) of oblate dust grains and remain in the size limit of the MRN model with a lower cut-off radius of $a_{\max} = 5$ nm in all simulations. For the dust-to-gas ratio we assume a constant value of $m_{\text{dust}}/m_{\text{gas}} = 0.01$ (Boulanger *et al.*, 2000) in the entire thesis.

Chapter 5

Synthetic polarization maps of star-forming regions

In this chapter we investigate the potential of synthetic continuum polarization measurements with aligned dust grains to determine its potential to trace the magnetic field morphology in star-forming regions. For this purpose we perform MC RT simulations in artificial environments. Initially, we apply the *POLARIS* to benchmark tests as well as complex density and temperature distributions in order to establish the predictive capability and accuracy of the MC RT code. Later, we apply the *POLARIS* code to analytical models as well as a post-processed complex MHD simulation associated with different stages of the star formation process. Here, we study the impact of different grain alignment theories on synthetic polarization observations. Thus, we cover the full spectrum of dust grain parameters, grain alignment theories, and polarization effects presented so far in this thesis. The resulting synthetic polarization maps will provide constraints concerning the accuracy, spectral coverage, and spatial resolution required to determine the magnetic field morphology with aligned dust grains.

5.1 Benchmark and test setups

5.1.1 Offset dust heating

In this section we post-process the dust temperature provided by a MHD collapse simulation in order to validate the accuracy of the offset dust heating feature of the *POLARIS* code. The chosen MHD simulation formed an accretion disk with two outflow lobes (see

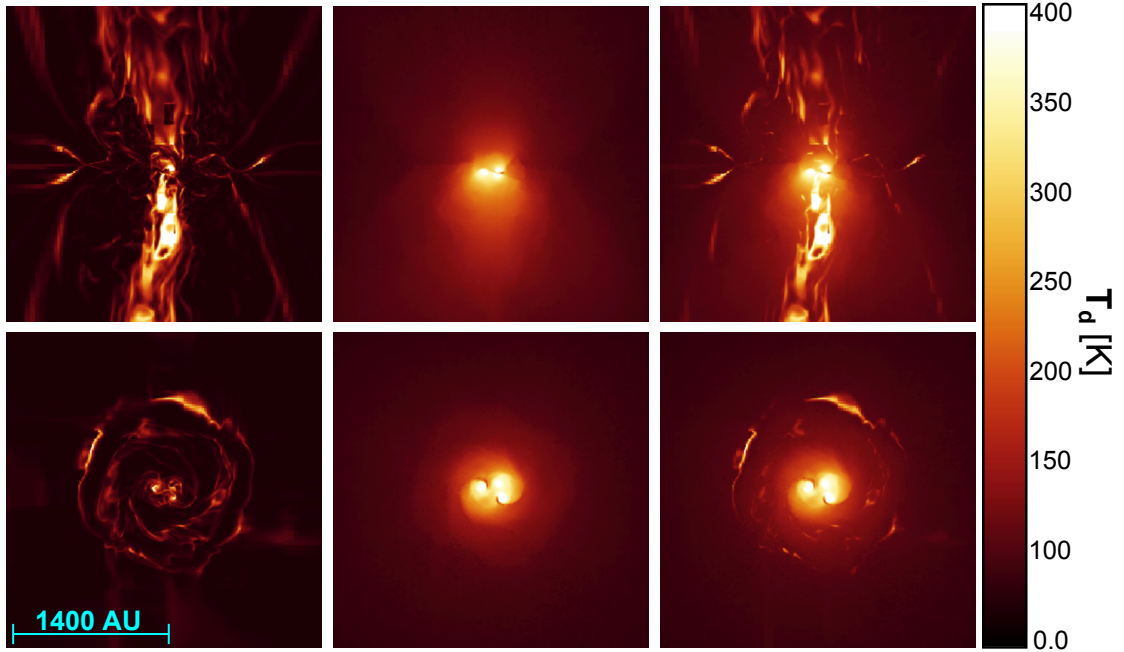


Figure 5.1: *Dust temperature distribution in the mid-planes of a MHD collapse simulation.* Rows show the results of the same results, but rotated by 90° . In the left column the dust was heated by a MC RT simulation alone. The middle column shows the dust temperature distribution as a result of shock heating in the MHD simulation. The dust temperature combined by offset dust heating as described in Sect. 4.5.6 is shown in the right column. The length of 1400 AU is for scale. We applied an upper cut-off of 400 K to the colorbar for better illustration.

Sect. 5.3.1 for a detailed description). The initial dust temperature as well as the position, stellar radii, and the surface temperatures of the stars were provided by the data of the MHD simulation itself. As dust model we apply the typical ISM parameters presented in Sect. 4.6 with an upper cut of radius of $a_{\max} = 0.25 \mu\text{m}$. The resulting highest temperature in these simulations is below the sublimation temperature of the silicate and graphite grains, respectively. First, we ignore the MHD dust temperature and performed a MC RT simulation with the stars as only source of radiation. Then, we adjust the temperature with the method of offset dust heating as described in Sect 4.5.6.

In Fig. 5.1 we show the resulting dust temperature distributions in the center planes of each MHD simulation. For the MC RT simulations without offset heating (Fig. 5.1 middle column), the dust temperature shows the expected diffuse distribution with the highest temperature near the stars. Regions with high densities are shielded from stellar radiation and cannot be heated sufficiently. For a dust temperature distribution as such a signal in intensity and polarization can just be expected near the stars. All the

information of density distribution is lost in the outer regions of the MHD simulation. The resulting dust temperature distribution matches the density structure near the disk region while the outflow regions remain hidden. High density regions, however, gain temperature by the dynamical processes of shock heating in MHD simulations (Fig. 5.1 left column). The MHD dust temperature resembles the dust density in all regions while underestimating the temperature in close proximity of the stars. The offset dust heating gives the correct temperature near the stars and simultaneously allows to make predictions about the dust density distribution in the outflow lobes (Fig. 5.1 right column) with the help of synthetic intensity and polarization maps.

5.1.2 Choice of grain alignment and scattering phase function

phase function	Rayleigh reduction factor	star position in [L]
ISO, HG, MIE	$R \in [0, 1]$ with $\Delta R = 0.1$	(-0.5,-0.5,-0.5), (0.0,0.0,0.0), (0.5,0.5,0.5)

Tabelle 5.1: *Parameter space of the dust heating study.* The side length of the model is $L = 5000$ AU.

Despite the spatial distribution of radiation sources the propagation of scattered light as well as the grain alignment efficiency may also be of relevance for the 3D distribution of the local radiation field and, subsequently, for dust temperature as well as the RAT alignment efficiency calculated by a MC RT simulation. The scattering behavior of the dust is highly dependent on the applied scattering phase function as well as the shape and the alignment efficiency of the dust grains. The assumption of dust grains to be spherically shaped or PA might be an approximation prone to large errors. In order to calculate the correct dust temperature with an MC RT simulation, the exact alignment efficiency has to be known in the first place. A problem arises from the dust temperature dependency of the considered IDG, RAT, and II alignment theories. The problem may be resolved by an iterative approach with alternating calculations of radiation field and grain alignment efficiency in the dust heating mode and the RAT alignment mode until a convergence criteria is fulfilled.

In this section we study the influence of different grain shapes, alignment efficiencies, and phase functions on the resulting distribution of dust temperature and RAT alignment efficiency in an artificial environment. The test model consists of a cube with a side length of $L = 5000$ AU and a linear gradient of gas density with $n_g \in [0 \text{ m}^{-3}, 10^{10} \text{ m}^{-3}]$. Here, the radiation source is a single star at three different positions. The applied parameter space is shown in Tab. 5.1. For the dust, we applied the mixture of Sect. 4.6 with

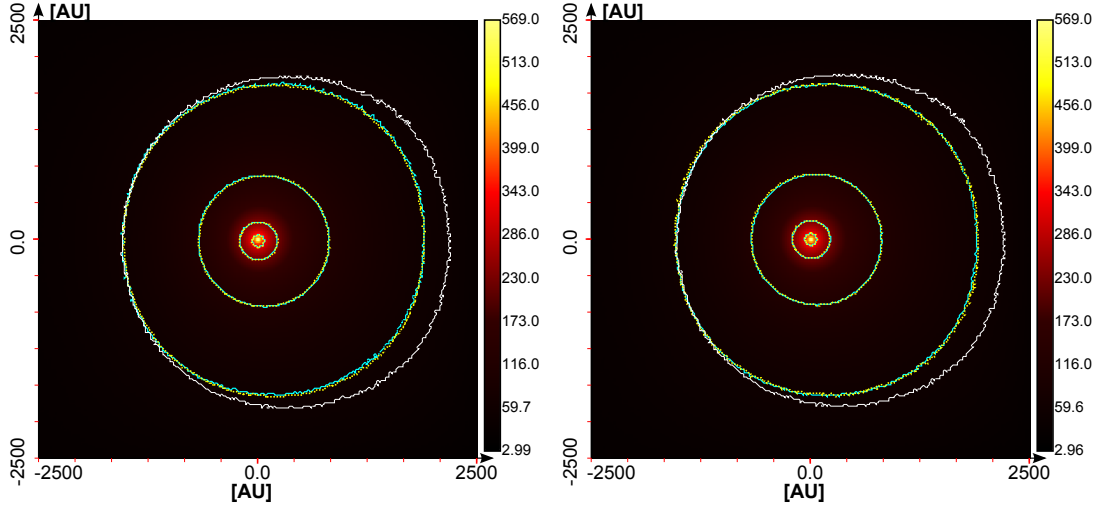


Figure 5.2: Color coded dust temperature distributions in the mid-plane of an artificial test scenario. The distributions were calculated with the HG phase function overlaid with the contour lines of the dust temperature considering spherical dust grains (left panel) and contour lines for partially aligned oblate dust grains with a Rayleigh reduction factor of $R = 0.5$ (right panel). Contour levels are at $0.1 T_{d,max}$, $0.2 T_{d,max}$, $0.4 T_{d,max}$, and $0.6 T_{d,max}$ calculated with isotropic scattering (solid white line), the HG phase function (solid cyan line), and Mie scattering (dotted yellow line) around a central star.

an upper cut of radius of $a_{max} = 0.25 \mu m$.

All the results of the different configurations listed in Tab. 5.1 are similar to that shown in Fig. 5.2 in the entire parameter space without exception. An increase in dust temperature is expected because of higher density towards the right side. However, the resulting dust temperature calculated with the HG phase function and Mie scattering are identical within numerical limits. The exception is isotropic scattering where the dust temperature is higher towards the center region. The same results appear for the tests with the distribution of aligned dust grains according to RAT theory. A significant difference between HG phase function and Mie scattering cannot be demonstrated.

Consequently, in the dust heating mode and the mode for RAT alignment the scattering phase function is of minor relevance. Hence, we use in all MC RT simulations the HG phase function because of its lesser computational efforts to sample the new direction of the photon package. Only in the MC mode for creating polarization maps, the full scattering matrix is required to sample the new directions of the photon package and to calculate the change in the Stokes vector components accordingly.

5.1.3 Comparison between the MC RT codes *MC3D* and *POLARIS*

In order to make predictions about the impact of imperfectly aligned dust grains on polarization measurements the *POLARIS* code goes beyond previous approaches in this field. Its treatment concerning polarization as a result of dichroic extinction and thermal re-emission combined with state of the art dust grain alignment mechanisms is unique in that way. Therefore, essential features cannot be tested because of the absence of standardized benchmark tests. However, dust heating and polarization calculations of scattering on spherical dust grains are implemented in many codes.

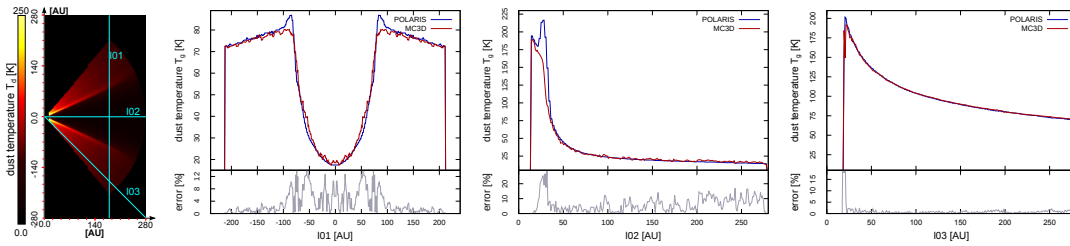


Figure 5.3: Resulting dust temperature T_d for the D03 disk model (see Tab. 5.3). The outer left panel shows the temperature distribution in a plane perpendicular to the mid-plane of the disk. The plots show the temperature along the edge of the disk perpendicular to the mid-plane (left) along the mid-plane of the disk (middle) and the distribution along the disks surface (right). The red lines show the results from the *MC3D* code, the blue ones the results from the *POLARIS* code, and the gray lines show the error between both codes.

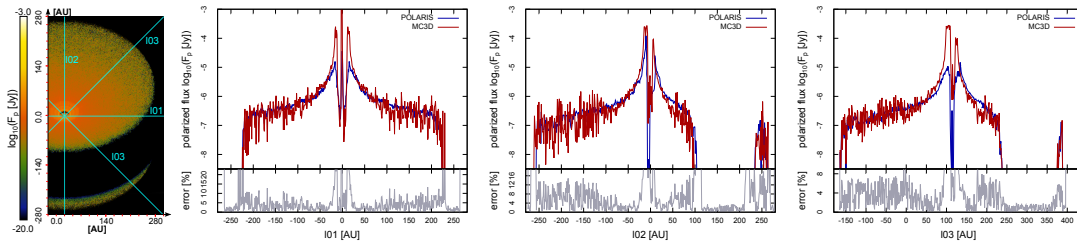


Figure 5.4: Resulting distribution of the polarized flux F_p for the D03 disk model (see Tab. 5.3). The outer left panel shows the polarized flux distribution as a result of scattered stellar radiation under an inclination angle of $i = 45^\circ$ and a wavelength of $\lambda = 730$ nm. The plots show the polarized flux through the center of the disk along the horizontal direction (left) along the vertical direction (middle) and the bisecting line (right). The red lines show the results from the *MC3D* code, the blue ones the results from the *POLARIS* code, and the gray lines show the error between both codes.

Although, *POLARIS* is a completely new line of development, we used the established and well-tested MC code *MC3D* (see Wolf, 2003) as a reference for light scattering and dust heating. Here, we confirm the accuracy of *POLARIS* by comparing the results of the disk models *D03* – *D06* (see Sect. 5.2.2 for a detailed description) with the results of *MC3D*. In order to provide identical test cases for both codes, we converted the standard *MC3D* dust catalog with spherical dust grains in a *POLARIS* database file format. We processed the *MC3D* output of the density distribution to create an octree grid required by *POLARIS*. Since, the dust temperature in low density areas amounts to unrealistically high values and *MC3D* does not control for the sublimation temperature of the applied dust materials we considered cells with a dust density of $n_d < 10^{-20} \text{m}^{-3}$ to be empty. For the MC calculations of the dust temperature distribution T_d and the polarized flux $F_p = P \times F_\lambda$ with scattering we used the disk parameters of Tab. 5.3. The deviation between the results of both codes was quantified with an error of $e = 100|x_1 - x_2| / \max(|x_1|, |x_2|)$ where x stands for dust temperature and polarized flux, respectively.

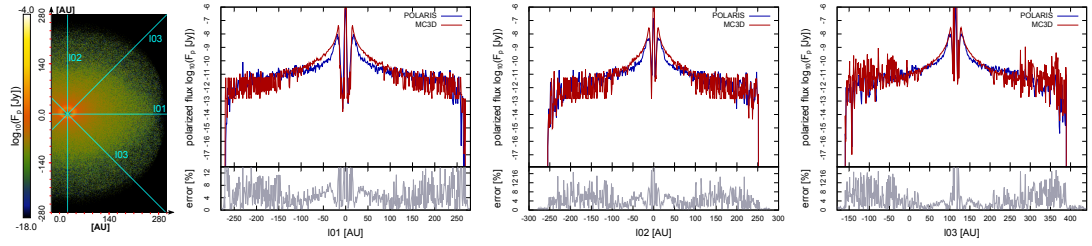


Figure 5.5: The same as Fig. 5.4 for the D06 disk model.

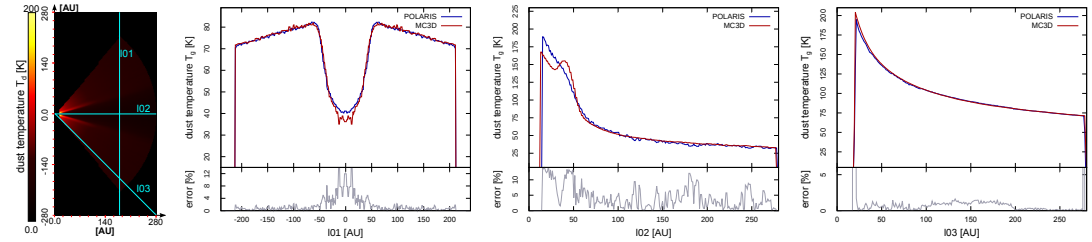


Figure 5.6: The same as Fig. 5.3 for the D06 disk model.

The dust temperature distribution of the disk model *D03* resulting from the *MC3D* code and *POLARIS* code is shown in Fig. 5.3. In the outer regions the temperature distributions match well but the difference in temperature is much higher at the inner edge of the disk. This difference is a result of the available grid geometries implemented in both co-

des. While *MC3D* performed the RT calculations on a spherical grid with smaller cells towards the center, *POLARIS* uses a cartesian octree grid with a constant minimal cell size. The geometrical difference in both coordinate systems results also in a different shaped inner border of the disk. Because of this *POLARIS* overestimates the temperature in the inner regions. For the same reason the dust temperature differs in the *D06* disk model shown in Fig. 5.6.

Finally, we compare the resulting polarized flux in Fig. 5.4 for the *D03* model and in Fig. 5.5 for the *D06* in a distance of 140 pc to the observer. While the overall trend along the selected lines matches quite well for both codes, the region of deviation remains near the inner radii in all disk models. The higher resolution in the center region of *MC3D*'s grid leads to a layer of higher dust density at the inner edge. Subsequently, more light is scattered towards the observer. In comparison to *MC3D*, the synthetic images of the polarized flux calculated with *POLARIS* have a higher signal-to-noise ratio because of the implemented optimizations of the forced first scattering algorithm and the peel of technique (see Sect. 4.4). However, in all test cases, the results of *POLARIS* fit those of *MC3D* well within the inherent limitations of applied grid geometries.

5.2 Analytical models

In this section we aim to model the underlying processes that lead to linear and circular polarization of previously non-polarized light. Here, we investigate the possibility to detect the morphology of the magnetic field with analytical models assuming ideal conditions. Although such models cannot account for a small scale turbulent component in the magnetic field or a complex filamentary density distribution. However, they can reproduce the effects of grain alignment on large scales.

5.2.1 Bok globules

A Bok globule is a relatively compact small cloud with a typical diameter of 0.1 pc - 0.8 pc and a range of masses $10 M_{\odot}$ - $60 M_{\odot}$ (Clemens *et al.*, 1991). Their hallmark is the obscuration of background stars in the UV and visual regime of wavelengths. For this reason most observed Bok globules are closer than 500 pc. More distant objects are more difficult to detect because of foreground stars. A Bok globule is relatively isolated and as such not subject to external disturbances making it a good test object for star formation theories (Yun & Clemens, 1990).

5.2.1.1 The model setup

Model	Alignment	T_g [K]	T_d [K]	Morph.	Mag. field [T]
BE _{const}	PA	2 - 15	X	parallel to z-axis	X
BE _{toro}	IDG	2 - 15	12 - 25	toroidal	$2 \times 10^{-17} - 2 \times 10^{-8}$
BE _{hour}	IDG	2 - 15	12 - 25	hourglass	$2 \times 10^{-17} - 2 \times 10^{-8}$
BE _{heli}	IDG	2 - 15	12 - 25	helical	$2 \times 10^{-17} - 2 \times 10^{-8}$
BE _{dipol}	IDG	2 - 15	12 - 25	dipole	$2 \times 10^{-17} - 2 \times 10^{-8}$
BE _{quad}	IDG	2 - 15	12 - 25	quadrupole	$2 \times 10^{-17} - 2 \times 10^{-8}$

Tabelle 5.2: *Physical parameters of the Bok globule models.* The characteristic radius for the BonnorEbert sphere is $r_c = 1100$ AU. For the PA alignment not all parameters are required. Parameters irrelevant for the radiative transport calculations are marked with an X.

The model setup is similar to that presented in Reissl *et al.* (2014). However, in this section we calculate the dust temperature by a MC RT simulation instead of modeling it with an analytical function.

Assuming an isothermal cloud with spherical symmetry the radial density $\rho(r)$ follows

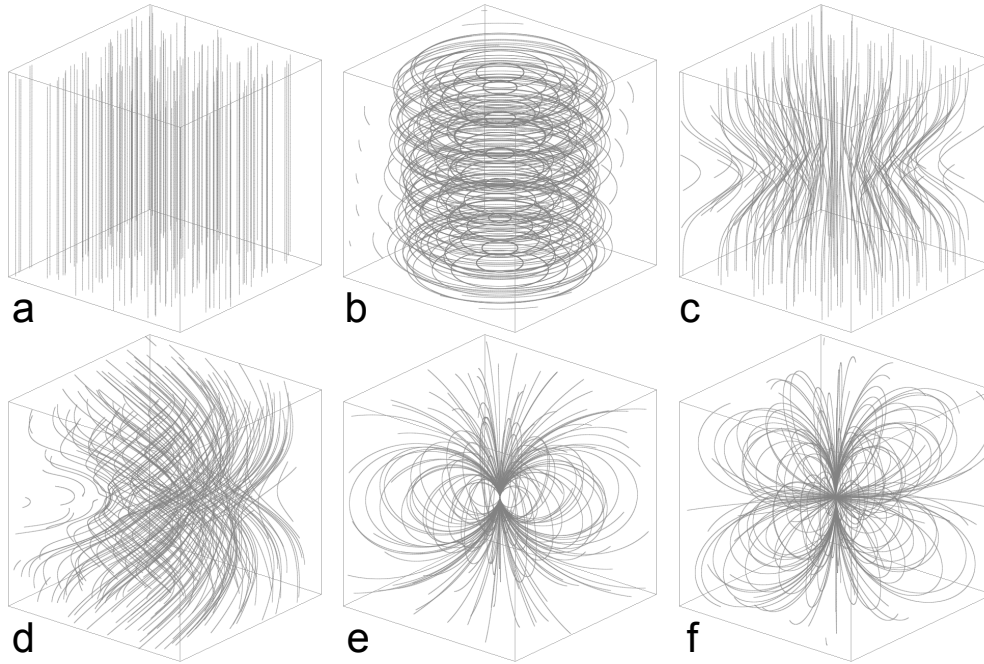


Figure 5.7: 3D plots for the constant (panel a, Eq. 5.2), toroidal (panel b, Eq. 5.4, hourglass (panel c, Eq. 5.3) helical (panel d, Eq. 5.5), dipole (panel e, Eq. 5.6), and quadrupole (panel f, Eq. 5.7) magnetic field morphologies.

a Bonnor-Ebert (Ebert, 1955; Bonnor, 1956) profile and can be modeled with

$$\rho(r) = \rho_0 \frac{r_c^2}{r^2 + r_c^2} \quad (5.1)$$

where r_c is a critical radius controlling the spatial extension of the sphere. In this study we apply a critical radius of $r_c = 1100$ AU and chose the density ρ_0 to result in a total mass of $10 M_\odot$ within the sphere. In order to limit the parameter space we consider just the effects of IDG alignment on the resulting degrees of linear and circular polarization. Since we have just the ISRF as source of radiation in this scenario RAT alignment cannot be considered to contribute significantly to the net-polarization in this section because of a weak overall radiation field. A velocity component of the gas, possible outflows typical for such objects, a pseudo-disk, or newly born stars as additional sources of radiation are also not considered in the following Bok globule models.

Existing models of gravitational collapse and the formation of outflows and disks make predictions of the magnetic field configurations involved. In particular, time-dependent models predict different magnetic field geometries at different ages, and thus we can try to match the observationally determined core classes with particular models to establish

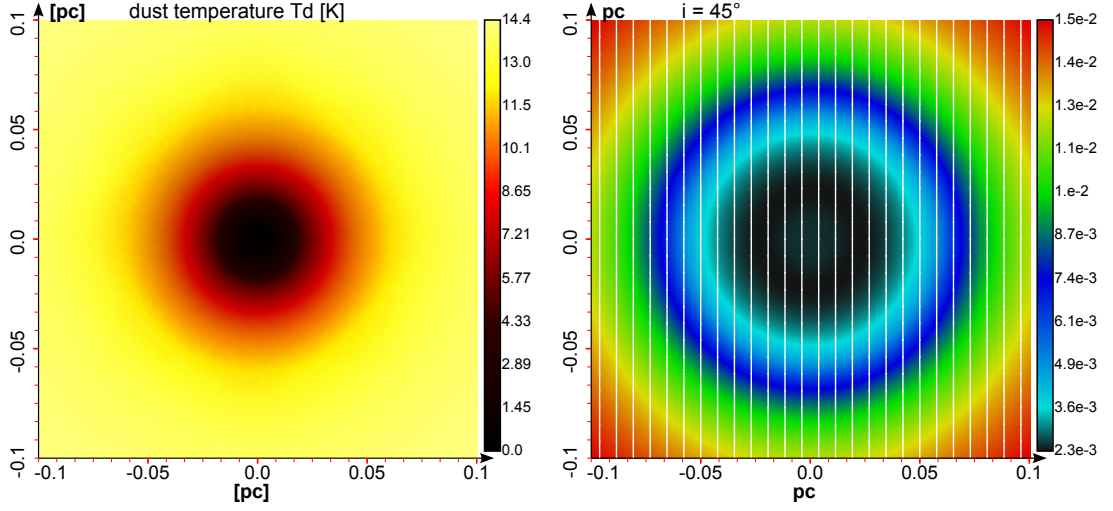


Figure 5.8: *Left panel: Dust temperature distribution in the mid-planes of the Bonnor-Ebert sphere density profile. The temperature was calculated with the ISRF as radiation source. Right panel: Resulting pattern of linear polarization. The pattern is overlaid with polarization vectors for the model BE_{const} at a wavelength of $810 \mu\text{m}$ and with an inclination angle of $i = 45^\circ$.*

rough ages. In younger objects, the predicted magnetic fields are expected to be well ordered and perpendicular to the future disk plane (Tomisaka, 1998) and the field lines are only slightly contracted. Therefore, we consider the grain alignment to be perfect in the simplest model BE_{const} and apply a constant field direction parallel to the z -axis of the model space with:

$$\vec{B}_{\text{const}}(x, y, z) = \begin{pmatrix} 0 \\ 0 \\ 1 \end{pmatrix}. \quad (5.2)$$

Both, theory (see Mestel, 1966; Seifried *et al.*, 2011) and observation (Crutcher, 1999) indicate consistently a strong correlation with $B \propto n_{\text{g}}^{-\kappa}$ between magnetic field strength and density over several orders of magnitude. Here, we assume a scaling parameter B_{κ} and $\kappa = 0.6$ to keep the magnetic field strength between 10^{-8} T in the center and 10^{-17} T at the edges of the model space and the the mass-to-flux ratio consistent with recent observations (Falgarone *et al.*, 2008; Girart *et al.*, 2009; Beuther *et al.*, 2010). The model label and relevant physical parameters are listed in Tab. 5.2 and a 3D plot of all considered magnetic field morphologies is provided in Fig. 5.7.

In older objects an hourglass-shaped magnetic field may occur near the a proto-star as the inflowing gas bends the magnetic field lines by means of ambipolar diffusion

(Tomisaka, 1998). As predicted by the magnetic support models of star formation the magnetic field lines are also expected to be smooth, with a regular structure. Despite available exact physical solutions (e.g. Galli & Shu, 1993) we approximate the hourglass morphology of the magnetic field by means of an analytical function with

$$\vec{B}_{\text{hour}}(x, y, z) = \frac{B_{\kappa}}{\sqrt{1 + (\alpha x z)^2 e^{-2\alpha z^2} + (\alpha y z)^2 e^{-2\alpha z^2}}} \begin{pmatrix} \alpha x z e^{-\alpha z^2} \\ \alpha y z e^{-\alpha z^2} \\ 1 \end{pmatrix} \quad (5.3)$$

where α is a shape parameter to adjust the field geometry. This analytical geometry allows for an accurate and expedient treatment of ambipolar diffusion to demonstrate the effects of different inclination angles to the maps of linear and circular polarization in the model BE_{hour}.

Molecular clouds are observed to rotate (e.g. Goodman *et al.*, 1993) and it is expected for a magnetic field in a rotating cloud to get also bend around the rotation axis. Consequently, the magnetic field direction can obtain a toroidal component as well. This case is considered in the model BE_{toro}. A pure toroidal magnetic field morphology can be modeled by:

$$\vec{B}_{\text{toro}}(x, y, z) = \frac{B_{\kappa}}{\sqrt{x^2 + y^2}} \begin{pmatrix} y \\ -x \\ 0 \end{pmatrix}. \quad (5.4)$$

We assumed the axis of rotation to be parallel to the predominant direction of the hourglass-shaped magnetic field lines in the model BE_{heli} and modeled a helical structure as a normalized superposition of Eq. 5.4 and Eq.5.3:

$$\vec{B}_{\text{heli}}(x, y, z) = \frac{B_{\kappa}}{\left| \vec{B}_{\text{toro}}(x, y, z) + \vec{B}_{\text{hour}}(x, y, z) \right|} \left(\vec{B}_{\text{toro}}(x, y, z) + \vec{B}_{\text{hour}}(x, y, z) \right). \quad (5.5)$$

In order to test the accuracy of polarization measurements in determining the magnetic field morphology we additionally considered a dipole field with

$$\vec{B}_{\text{dipl}}(x, y, z) = \frac{B_{\kappa}}{(x^2 + y^2 + z^2)^{5/2}} \begin{pmatrix} 3xz \\ 3yz \\ 2z^2 - x^2 - y^2 \end{pmatrix} \quad (5.6)$$

for the model BE_{dipl} and a quadrupole field for the model BE_{quad}

$$\vec{B}_{\text{quad}}(x, y, z) = \frac{B_{\kappa}}{2(x^2 + y^2 + z^2)^{7/2}} \begin{pmatrix} -3x(x^2 + y^2 - 4z^2) \\ -3y(x^2 + y^2 - 4z^2) \\ 3z(-3x^2 - 3y^2 + 2z^2) \end{pmatrix}, \quad (5.7)$$

respectively, in this study for comparison.

For the dust we apply the MRN model of Sect. 4.6 with an upper cut of radius of $a_{\max} = 0.25 \mu\text{m}$ typical for the ISM. In a first MC RT simulation, the temperature of all models was calculated considering the ISRF as radiation source (see Sect. 3.2 and Sect. 4.3) to constrain later the impact of IDG grain alignment and different magnetic field morphologies on synthetic polarization maps. The resulting dust temperature T_d varies in the range 2 K – 15 K with the lower temperature in the center and is shown in Fig. 5.8 on the left panel. For the relation between dust temperature and gas temperature we assumed $T_g = T_d + 10 \text{ K}$. This range and distribution of temperatures is within the expectation of both theory (e.g. Keto & Field, 2005; Sipilä *et al.*, 2011) and observation (e.g. Launhardt & Henning, 1997).

5.2.1.2 Results

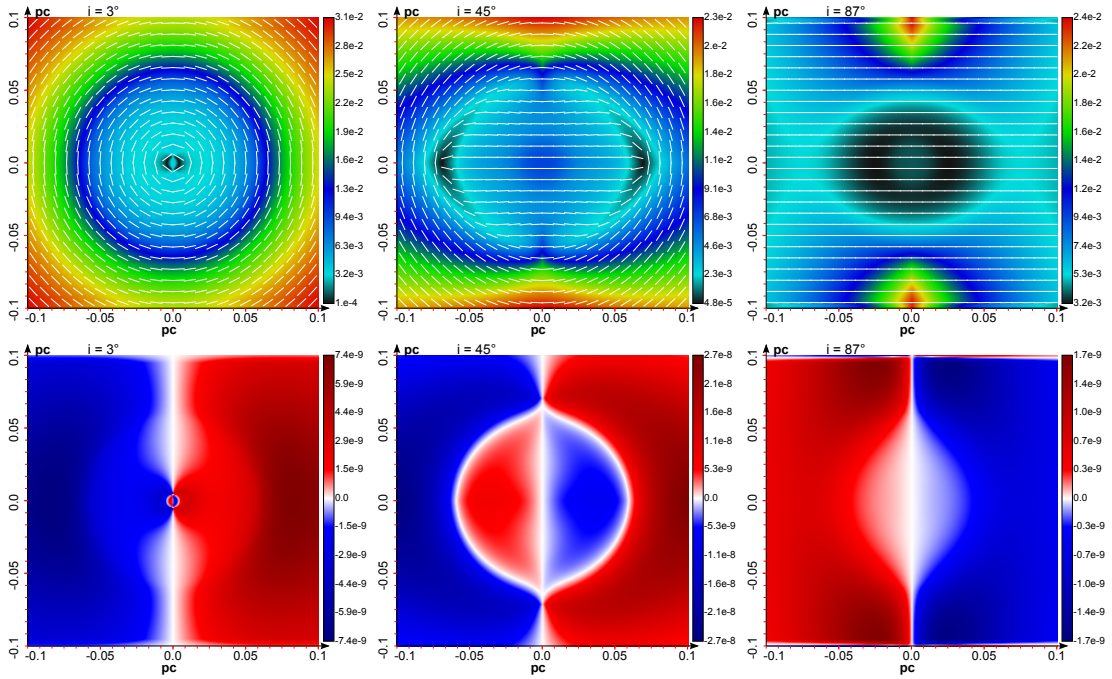


Figure 5.9: Linear polarization (top row) and circular polarization (bottom row) of model BE_{toro} with inclination angles of 3° (left column), 45° (middle column) and 87° (right column) at a wavelength of $810 \mu\text{m}$. We added an offset angle of 90° to the vectors of linear polarization to match the projected magnetic field morphology. The dust particles are aligned according to IDG theory.

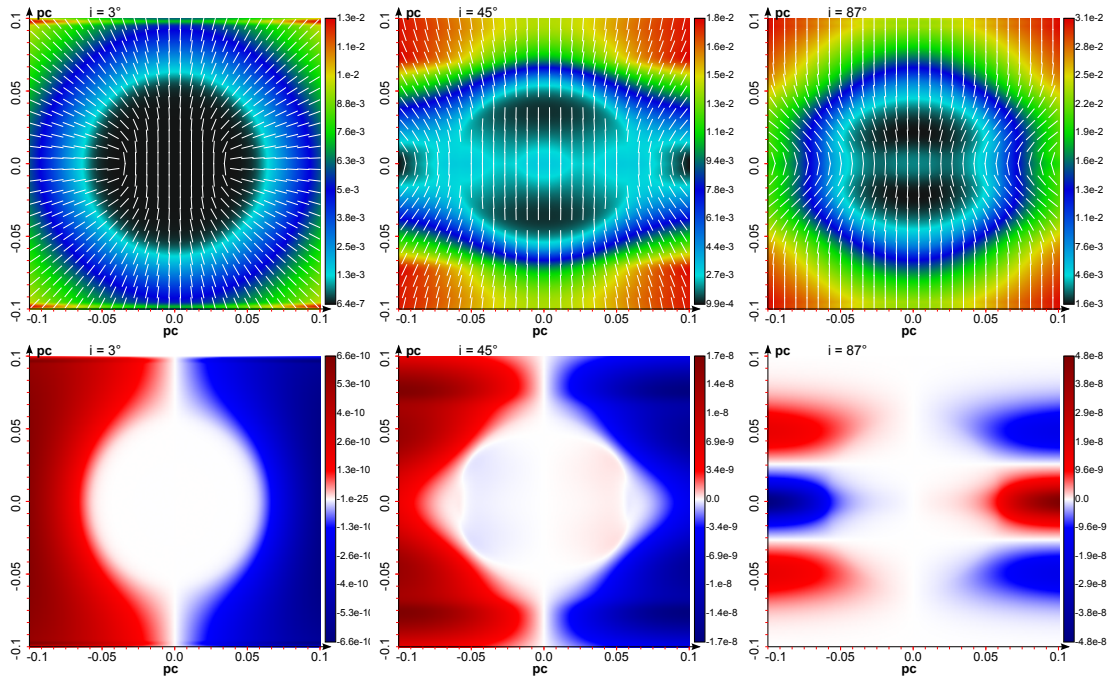


Figure 5.10: Same as Fig. 5.9 for the BE_{hour} model.

We start our investigation with the simplest case of a well ordered and constant magnetic field and PA dust grains in order to test the predictability of this model setup. Here, we apply the morphology of Eq. 5.2. Fig. 5.8 (right panel) shows a selected map of linear polarization for the inclination angle of $i = 45^\circ$ at an exemplary wavelength of $810 \mu\text{m}$. For this wavelength, linear polarization is completely dominated by thermal re-emission. Therefore, the polarization vectors were rotated by 90° to match the projected magnetic field morphology. In this simple case with PA, the vectors of linear polarization follow the expected pattern with a parallel orientation with respect to each other.

In the model BE_{toro} , the direction of the magnetic field lines is always parallel along the line of sight at an inclination angle of 0° as well as 90° . For this reason light can gain no circular polarization at all (see Sect. 4.5.1). However, at inclination close to 0° or 90° we can expect a pattern of circular polarization. Hence, we calculate polarization maps for a range inclination angles of $i \in [3^\circ, 87^\circ]$ for all models. The pattern in the degree of linear polarization in the maps follows the theory of IDG grain alignment. The dominating factor here is dust density. With increasing dust density towards the center the characteristic upper threshold of IDG alignment δ_0 (see Eq.3.16) is pushed beyond the maximal dust grain size. As expected, this results in a low degree of linear polarization in the center region. Since this effect is independent of field morphology, the same holds

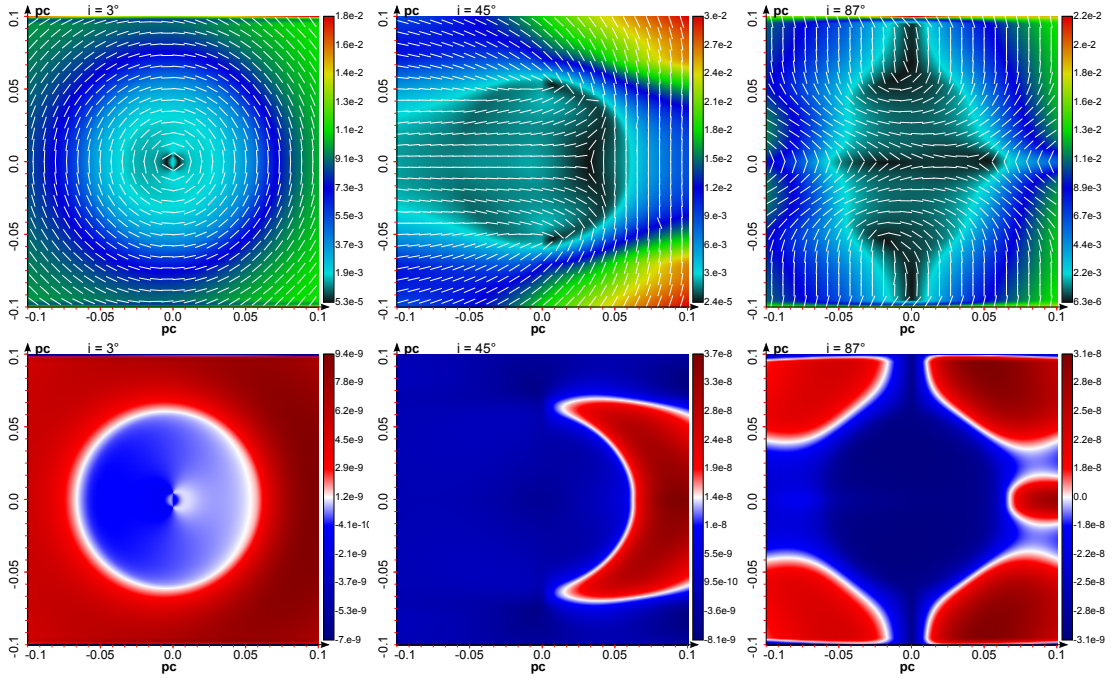


Figure 5.11: Same as Fig. 5.9 for the BE_{heli} model.

for all models.

Figs. 5.10, 5.12 and 5.13 show the degrees of linear and circular polarization for three different inclination angles for the model setups BE_{hour} , BE_{dipl} , and BE_{quad} . With increasing inclination angle the hourglass morphology, dipole morphology, and quadrupole morphology (see Fig. 5.7 c, e, and f), respectively, become apparent. However, for an inclination angle as low as 3° , the underlying field morphology remains ambiguous. In all three configurations the vector field of linear polarization shows a similar radial symmetric pattern. In this case, the magnetic field morphologies would be indistinguishable by measurements of linear polarization alone. In contrast to the ambiguities in the pattern of linear polarization, the maps of circular polarization remain unique for each field morphology, as we show in the right columns in Figs. 5.10, 5.12, and 5.13. Here, we demonstrate that the hourglass, dipole, and quadrupole fields are distinguishable even for observations with low inclination angles because of the unique symmetry axis of each morphology which results in a characteristic pattern of circular polarization.

In Fig. 5.11 we present the degree of circular polarization as well as degree of linear polarization overlaid with the normalized position vectors for the model setup BE_{heli} . The magnetic field morphology in BE_{heli} has no axis symmetry but a point symmetry with respect to the center of the model space. Hence, crossing magnetic field lines along any line of sight and pattern of circular polarization would even be present for inclination

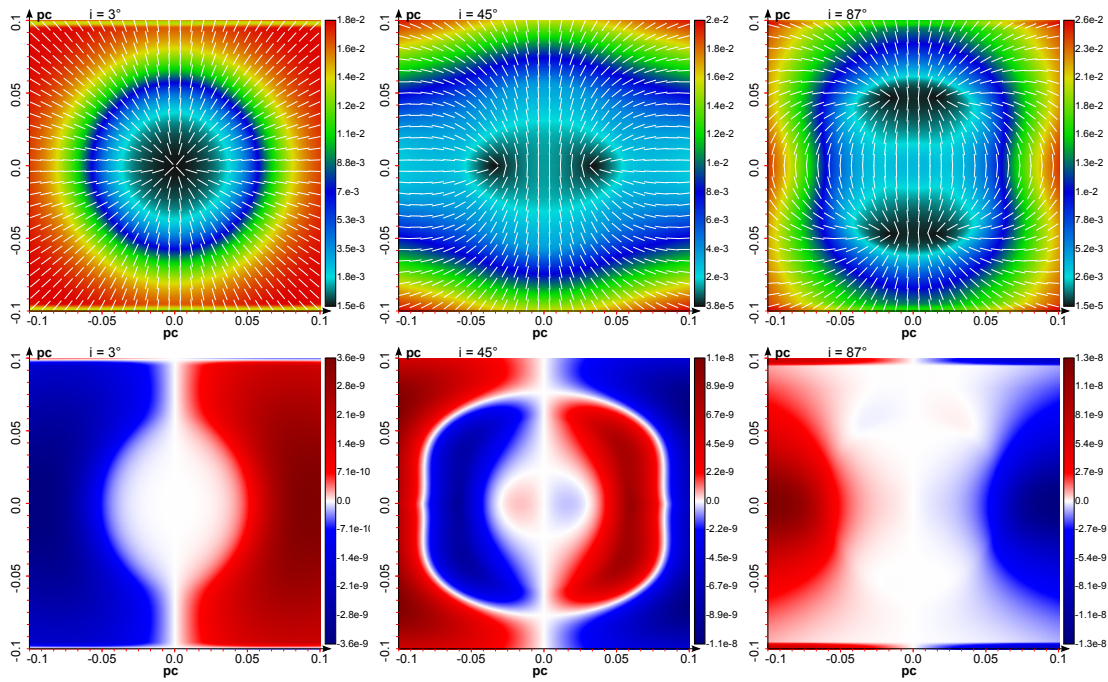


Figure 5.12: Same as Fig. 5.9 for the BE_{dipl} model.

angles of 0° and 90° . Note that the presence of crossing field lines does not necessarily lead to a low degree of linear polarization. As long as the directions of the field lines are not perpendicular to each other, they can still contribute to the net polarization due to dichroic extinction. Furthermore, nearby hot but optically thin regions can also rapidly build up linear polarization because of thermal reemission.

In contrast to other models, the initial symmetric pattern of BE_{heli} in the synthetic linear and circular polarization maps becomes distorted while rotating the model space towards higher inclination angles. Because of its helical symmetry (see Fig. 5.11). We see toroidal patterns in the top rows of Fig. 5.10 similar to those in Fig. 5.11 for low inclination-angles. A similar behavior can be found for high-inclination angles in the model setups BE_{hour} and BE_{heli} , as shown in the bottom rows of Fig. 5.10 and Fig. 5.11. Although the patterns of linear polarization deviate in both cases, the orientation vectors match quite well, which provide the possibility for misinterpretations under realistic observational conditions. Again, unique patterns in circular polarization measurements allow an unambiguous identification of the predicted magnetic field morphology independent of inclination angle.

In Fig. 5.14 we present plots of the mean values of the degree of optical depth, normalized linear polarization and normalized circular polarization over wavelength for different inclination angles. With exception of model BE_{heli} , the plots of all models are

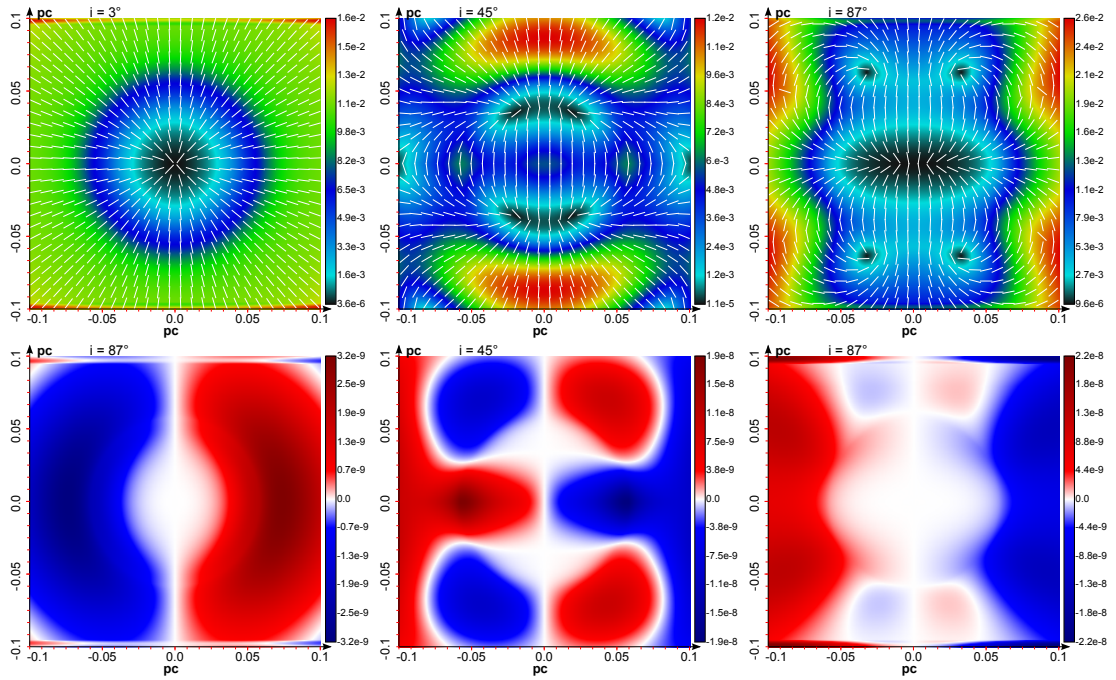


Figure 5.13: Same as Fig. 5.9 for the BE_{quad} model.

quite similar to each other. Hence, we show just the normalized results of BE_{hour} and BE_{heli} for comparison. As expected, the optical depth follows exactly the cross sections of extinction of the dust grain model as presented in Sect. 4.6. The same result can be seen in the mean values of linear and circular polarization. However, the degree of circular polarization for the Model BE_{heli} shows an exceptional behavior. While the minimum and maximum of the mean value shows a symmetrical characteristic for all other models, the model BE_{heli} is asymmetric with respect to $P_c = 0$ as a direct result of the helicity in the magnetic field morphology.

5.2.1.3 Discussion

A polarized emission signal has been detected successfully at a arcsecond scales. The best example is the measurement of polarized dust emission in the proto-stellar system NGC 1333 IRAS 4A as it is presented in Girart *et al.* (2006). This observation reveals an hourglass magnetic field morphology in accordance with the classical prediction of star formation. However, observations of an hourglass shaped magnetic field are quite rare. In this section we reported, that an inclination angle can have an unfavorable influence on observations. Hence, low inclination angles can veil the underlying magnetic field morphology effectively. The number of already observed systems with an

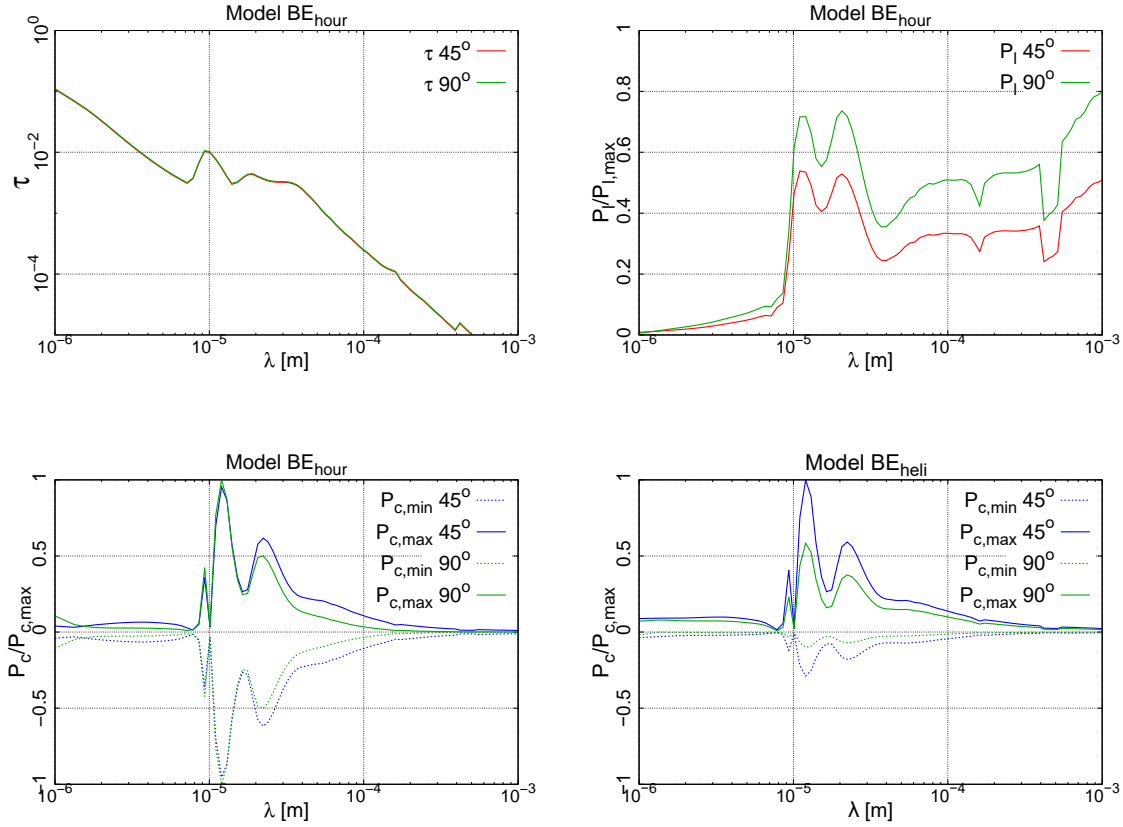


Figure 5.14: Resulting mean values of optical depth τ (top left panel), normalized linear polarization (top right panel), and normalized circular polarization (bottom left panel) over wavelength for different inclination angles for the model BE_{hour}. The normalized circular polarization of model BE_{heli} is in the bottom right panel.

hourglass shaped magnetic field morphology might actually be higher but not identifiable by means of linear polarization alone.

The interpretation of linear polarization measurements are furthermore hindered, by the similarity of polarization pattern resulting from distinct projected magnetic field morphologies. This dilemma of ambiguous measurements of linear polarization can potentially be resolved by complementary measurements of circular polarization in order to identify distinct magnetic field morphologies. Circular polarization measurement as a promising source of additional information was already mentioned in Dolginov & Mitrofanov (1976b). However, the measurement of circular polarization data, so far, is not obtainable by available observational equipment. It remains also unclear whether the

predicted low values of circular polarization in the order of $10^{-8} - 10^{-10}$ as predicted by our models are accessible to observational equipment in the near future.

Dust polarization is not a common feature in MC RT codes. The modeling of observational data is generally performed by an algorithm assuming a constant emissivity per mass unit and optically thin regions (e.g. Fiege & Pudritz, 2000; Tomisaka, 2011). In this approach the degree of linear polarization is far to high. Usually dust grain alignment efficiency as well as the optical properties of the dust grain is approximated by a single parameter to account for actual observation. We demonstrate in this section that lower degrees for the upper limit of linear polarization of $\approx 10\%$ as required by observational data (Girart *et al.*, 1999; Gonçalves *et al.*, 2005; Davidson *et al.*, 2011) can also be achieved by combining a physically well motivated dust grain model and theory of grain alignment with MC RT calculations. In contrast to the common procedure the more realistic approach presented in this thesis would additionally allow to create predictive models concerning questions of dust grain composition and dominant grain alignment theory.

Finally, it needs to be pointed out that the magnetic field strength cannot reliably be determined with the help of MC RT simulations. The huge uncertainties concerning dust grain alignment theory as well as the enormous parameter space of dust properties does not allow for a successful fitting process by means of synthetic polarization data alone.

5.2.2 Circumstellar disks

The magnetic field plays an important role in the formation of stars as well as in the formation and evolution of the circumstellar disk and, subsequently, in the formation of planets. Angular momentum of the gas component of the disk can effectively be transferred outwards by magnetic braking and interstellar outflows allowing for the gas to move towards the center. Hence, to understand circumstellar disk and planet formation, we need to investigate the properties of the underlying magnetic field involved in the formation process. In this section we trace the magnetic field morphology with *POLARIS* in circumstellar disks of different mass.

5.2.2.1 Model setup

α	β	h_0 [AU]	r_0 [AU]	R_{in} [AU]	R_{out} [AU]	M_{disk} [M_{\odot}]	R_* [R_{\odot}]	T_* [K]
1.25	2.6	10	100	25	280	10^{-6} - 10^{-3}	6	4000

Tabelle 5.3: *Parameters of the applied disk models.* We consider different disk masses and refer to the models with a total disk mass of $10^{-3} M_{\odot}$ as D03, with $10^{-4} M_{\odot}$ as D04, with $10^{-5} M_{\odot}$ as D05 and with $10^{-6} M_{\odot}$ as D06, respectively.

In the presence of a magnetic field inside a disk, the dust grains can be expected to be partially aligned with the direction of the magnetic field. Consequently, the field morphology may be investigated by polarization measurements. Here, we model the processes that lead to linear polarization of previously un-polarized radiation from the central star to reveal the morphology of the magnetic field in the polarization signal in the submm regime of wavelengths.

The magnetic field is assumed to be dragged with the rotation of the disk because of ionized gas. Hence, the field morphology can be approximated by a toroidal field on the disk scale (see Tamura *et al.*, 1999). Here, the magnetic field morphology is modeled by the analytical toroidal function of Eq. 5.4 with a magnetic field strength following the relation $B \propto n_{\text{g}}^{-\kappa}$ as introduced in sect. 5.2.1. Consequently, the magnetic field strength is between 10^{-8} T in the center and 10^{-17} T at the edges of the model space. The rotation axis of magnetic field and disk are assumed to be parallel. The dust component is similar to that presented in Sect. 4.6. However, the dust component consists only of astro-silicate as material with an upper cut-off in grain size at $a_{\text{max}} = 2 \mu\text{m}$.

The density distribution of our disk models are parametrized as presented in Shakura & Sunyaev (1973). The model assumes the density distribution to follow

$$n_{\text{g}}(r, z) = n_0 \left(\frac{r_0}{r} \right)^{\alpha} \exp \left(-\frac{1}{2} \frac{z}{h(r)} \right)^2 \quad (5.8)$$

where

$$h(z) = h_0 \left(\frac{r}{r_0} \right)^\beta . \quad (5.9)$$

Here, r and z are cylindrical coordinates, h_0 is the scale height at r_0 , and the quantities α and β are parameters which characterize the radial density profile and the disk flaring. By integrating from R_{in} to R_{out} we adjusted n_0 for the entire disk mass to range between $10^{-3} [M_\odot]$ and $10^{-6} [M_\odot]$.

For the dust heating we consider an offset dust temperature of 10 K within the boundaries of the disk and post-process the temperature with *POLARIS* and a central star as radiation source for all disk models. The offset dust temperature is of minor influence to the following calculations but ensures a non-zero temperature in each cell in the denser regions of the model space allowing to reduce the number of photon packages. The model of Shakura & Sunyaev (1973) assumes the dust to be in thermal equilibrium with the gas ($T_g = T_d$). In this case Eq. 3.18 reaches unity and the IDG Rayleigh reduction factor (see Eq. 4.36) becomes undefined. Subsequently, the IDG mechanism cannot be applied in the disk models. Hence we consider in this section only the effects of grain alignment according to RAT theory and assume a factor of $f_{\text{high-J}} = 0.25$ for the internal alignment. In a second step we apply the RAT mode of *POLARIS* to calculate the anisotropy and overall energy density of the radiation field in the disk as described in Sect. 3.3.2.4 to determine the minimal dust grain radius a_{alg} at which the dust grains start to align. Here we included both, the central star as well as the heated dust in each cell as sources of radiation in the MC RT simulations.

5.2.2.2 Results

Fig. 5.15 shows the resulting layered distribution of the D03 and D05 disk models. The distribution of aligned radii is layered with smaller aligned dust grains starting to align at the disks surface and larger grains towards the center plane. The model with the higher disk mass D03 on the left hand side of Fig. 5.15 shows a distinct distribution of imperfectly aligned dust grains. In contrast to model D03 for model D05 on the right hand side of Fig. 5.15 smaller dust grains are better aligned at the surface of the disk. However, with decreasing mass the alignment of dust grains increases fast towards the center plane and the outer regions. This is a consequence of different dust and stellar contributions to the radiation field as well as a variation in the local dust temperature. The optical depth and, subsequently, the amount of deposited energy by radiation decreases with disk mass.

Therefore, the surface is more efficiently heated in the disks with higher mass. Whe-

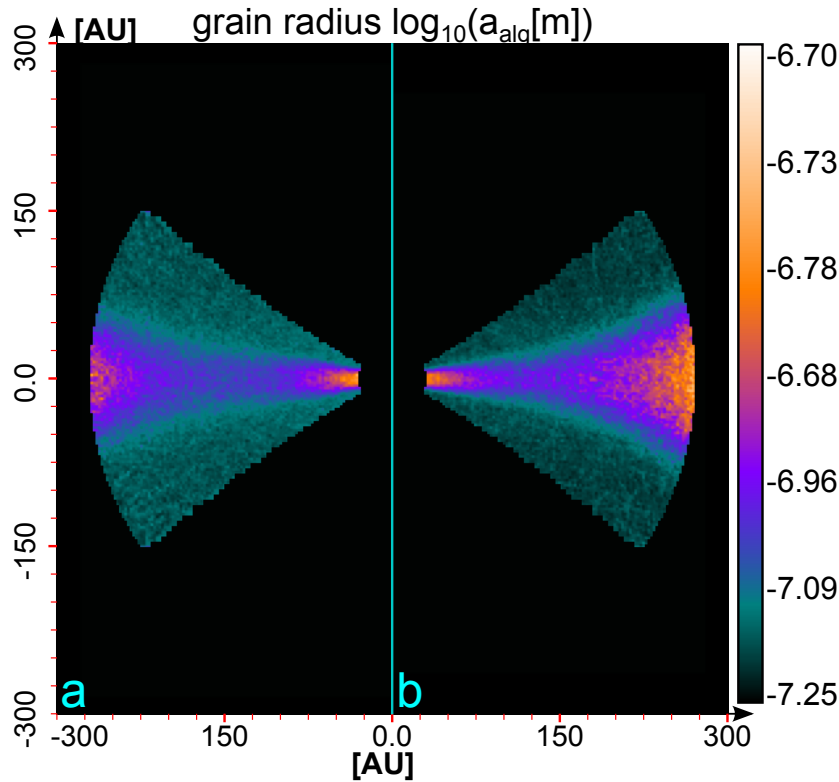


Figure 5.15: Distribution of grain sizes a_{alg} where dust particle start to align to the magnetic field direction \vec{B} according to RAT - theory. The shown plane is perpendicular to the mid-plane of the disks. The disk model D03 with $10^{-3} M_{\odot}$ is on panel *a* and the model D05 with $10^{-5} M_{\odot}$ is on panel *b*. Lower values of a_{alg} result in higher degree of linear polarization.

re as the grain alignment is suppressed near the sublimation radius for all models as a result of high temperatures in this region, the stellar radiation becomes more irrelevant in the outer regions of the disk. Consequently, the D03 model is less influenced by the central star. The radiation in the inner most regions in each disk originates from thermal photons emitted in the hot surface layers and not the star itself. Subsequently, the higher mass model D03 has aligned dust grains in much deeper layers as the lower mass model D06 (see Fig. 5.15). The resulting layered distribution in dust grain alignment is consistent with the results of Hoang & Lazarian (2014).

In Fig. 5.16 we show the effects of thermal dust re-emission dependent on the total disk mass. We compare the resulting polarization maps for the disk models D03 and D05 as a function of inclination angle at an exemplary wavelength of $\lambda = 515 \mu\text{m}$. The pattern and orientation of linear polarization in Fig 5.16 are in good agreement with the predictions by Cho & Lazarian (2005) and Cho & Lazarian (2007). Since all disk models are optically thin at that wavelengths, the synthetic polarization maps appear to be symmetric. The panels of Fig. 5.16 were calculated using the ray-tracing algorithm (see Sect. 4.4). Since lower values of the minimum size of aligned grains a_{alg} are associated with a higher degree of linear polarization (see Eq. 4.42), the D03 disk model shows a more

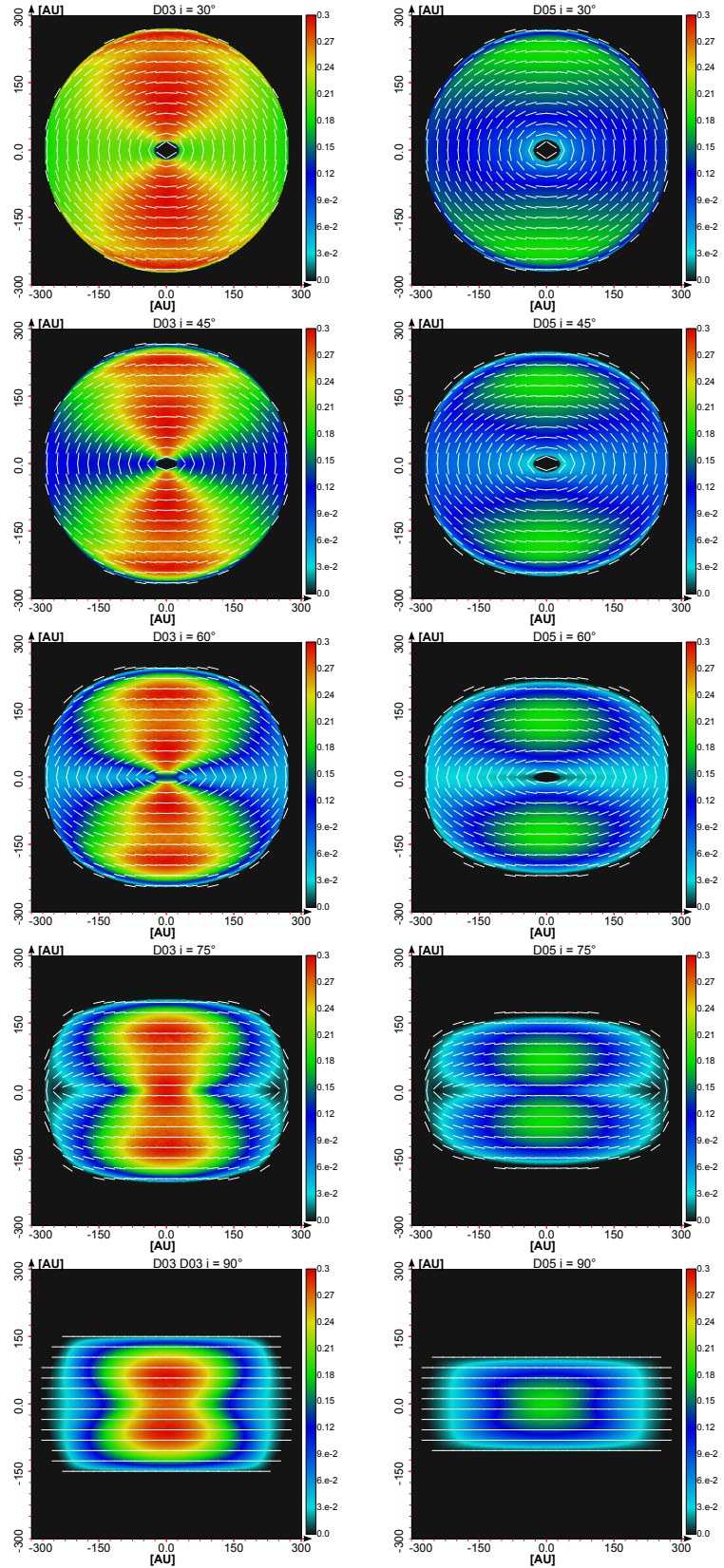


Figure 5.16: Maps with pattern of linear polarization overlaid with normalized orientation vectors at an exemplary wavelength of $\lambda = 515 \mu\text{m}$. We applied an offset of 90° to the orientation vectors to match the projected toroidal magnetic field morphology. The model D03 with $10^{-3} M_\odot$ is on the left column and model D05 with $10^{-5} M_\odot$ is shown on the right column for inclination angles from $i = 30^\circ$ (top row) to $i = 90^\circ$ (bottom row) in steps of 15° .

distinct pattern of linear polarization. A lower degree of linear polarization in low mass disks is consistent with the results shown in Fig. 5.15. This would also hold even if we considered imperfect internal alignment since the internal distribution function for RATs is independent of the local physical conditions of the disk models and just a function of grain geometry (see Sect. 4.42). The pattern in the normalized polarization vectors are identical for all models revealing the projected toroidal magnetic field geometry at all inclination angles since the influence of scattering can be neglected at $\lambda = 515 \mu\text{m}$. However, only for the D03 model the degree of linear polarization ($P_l > 0.5\%$) should be detectable in the entire disk even for low inclination angles.

The pattern of linear polarization have sharp cut offs with no polarization at the borders of the model. This is a result of the applied power-law correlation between density and magnetic field strength ($B \propto n_{\text{gas}}^{-K}$). Hence, the magnetic field satisfies no longer the minimal required field strength (see Eq. 4.5.4) in the thinner disk regions.

5.2.2.3 Discussion

Aligned dust grains as an explanation of polarized radiation in the FIR und submm from disks was already indicated by observations of Tamura *et al.* (1999). However, to what extend the observation of polarized light can reveal the underlying magnetic field morphology is still a matter of debate. Numerical calculations Cho & Lazarian (2007); Hoang & Lazarian (2014) predict that polarized radiation should emerge from the circumstellar disk region because of RAT alignment. In contrast to predictions, observations of circumstellar systems (Hughes *et al.*, 2009) show no detectable degree of linear polarization at all. The overestimation of RAT alignment because of perfect internal alignment in earlier studies (Cho & Lazarian, 2007) cannot account for this finding alone. An internal alignment with a conservative chosen parameter $f_{\text{high-J}} = 0.25$ would still result in a detectable degree of linear polarization. However, $f_{\text{high-J}}$ can still not be analytically determined and might also vary dependent on the predominant local conditions of each disk. Another explanation might be the shape and composition of the dust grains. It can not be expected that an similar amount of non-spherical dust grains that can align is equally present in all circumstantial disks but may vary significantly from disk to disk.

The distribution of grain sizes is also not expected to be equal in the entire disk. Dust grain growth and dust settling are processes that redistribute dust grains of different sizes in the disk (see e.g. Tanaka *et al.*, 2005). As a result of this, larger dust grains are more likely to be present near the disk plane. Thus, such grains have also a higher probability to be aligned by RATs than smaller dust grains located on the disk surface. Dust settling in disks might also help to explain the served low degree of linear polarization and should be considered in forthcoming studies with a more sophisticated dust model.

5.2.3 Cloud model

The question about what effects dominate the grain alignment in the ISM is still a matter of debate. Individual theories of dust alignment make unique predictions concerning the local physical parameters necessary for efficient dust grain alignment (see Sect. 3.3.1). This unique response of each alignment theory should also result in character pattern in the synthetic polarization maps. Therefore we examine the pattern of linear polarization emerging from different grain alignment theories separately in this section. The main focus here lies on the ambiguities associated with different grain alignment theories to infer the underlying magnetic field morphology on a predefined cloud model.

5.2.3.1 Model setup

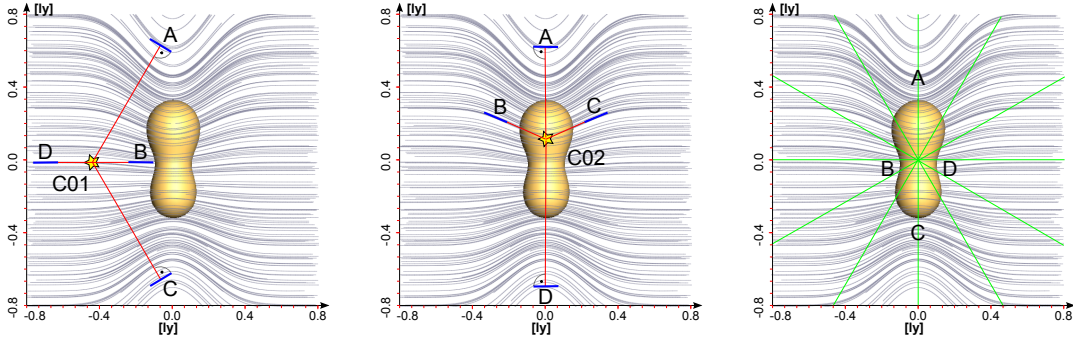


Figure 5.17: Schematic illustration of the cloud models C01 (left panel) and C02 (middle panel). Both models differ only by the position of a single star. The isocontour surface at $\log(n_d) = 3.27 \text{ m}^{-3}$ is in dark yellow. The direction of the common gas stream \vec{v} (right panel) towards the center is in green lines and the analytical hourglass field morphology is shown in grey. Red lines and blue bars indicate the different angles between radiation field and the magnetic field direction. The letters A – D indicate areas with expected characteristic features for RAT and GOLD alignment, respectively.

$n_{g1} [\text{m}^{-3}]$	$R_{c1} [\text{ly}]$	$n_{g2} [\text{m}^{-3}]$	$R_{c2} [\text{ly}]$	$R_* [R_\odot]$	$T_* [\text{K}]$	position of the star [ly]
10^{13}	0.2	10^{12}	0.1	8	6000	C01(-0.53,-0.0,-0.0) C02(0.0,0.0,0.13)

Tabelle 5.4: Table of physical parameter for the applied cloud models.

Our cloud models consist of two spheres following a Bonnor-Ebert density profile (see Eq.5.1) with a distance from core to core of 0.375 ly to each other. The characteristic

radii of the density distribution are 0.1 ly and 0.2 ly, respectively. Density and magnetic field morphology are chosen to be consistent with theoretical models and observation (Launhardt & Henning, 1997; Sipilä *et al.*, 2011) resulting in a total mass of $25 M_{\odot}$ in the model space.

We modeled an hourglass-shaped magnetic field geometry by the analytical function of Eq. 5.3 with its center in the denser sphere as expected by observations (e.g. Girart *et al.*, 1999; Frau *et al.*, 2011). Contrary to Sect. 5.2.1 the magnetic field strength is assumed to be constant with $B_0 = 1.5 \times 10^{-8}$ T. In order to compare calculations performed by *POLARIS* with the expected predictions for the IDG, RAT with that of the GOLD alignment theories, we also assume a supersonic velocity stream \vec{v} with a in-fall direction to the common center of both Bonnor-Ebert spheres. In this section, we also consider the effects of the internal alignment with $f_{\text{high-J}} = 0.5$ for RAT alignment (see Eq. 4.30 and Eq. 4.42). The dust temperature and the radiation field is calculated with a single star as radiation source (see Tab. 5.4). All considered alignment theories are highly dependent on dust temperature and the overall radiation field. Hence, we consider two different configurations concerning the position of the star. In model C01, the star is 0.53 ly away from the common center of both spheres where as in model C02, the star is embedded in the center of the denser Bonnor-Ebert sphere. A schematic illustration of the cloud models is provided in Fig. 5.17. The physical parameters of both cloud models are listed in Tab. 5.4.

An initial sphere temperature of $T_d = 10$ K was used for both cloud models C01 and C02 to correct the temperature according to the method described in Sect. 4.5.6. Here, we assume dust temperature and gas temperature to be correlated by a constant factor with $T_g = 10 \times T_d$. In a final step we applied the RAT mode of *POLARIS* to calculate the distribution of the characteristic grain size a_{alg} where dust grains start to align according to RAT theory. Here, we use both, the heated dust and the star as sources of radiation. With this configuration the models C01 and C02 allow the calculation of the characteristic linear polarization pattern for IDG, RAT, and GOLD alignment mechanism, respectively.

5.2.3.2 Results

Fig. 5.18 shows the ratio of cross sections of partially aligned dust grains and cross sections of PA dust grain in the mid-plane of both models separately for all alignment mechanisms at an exemplary wavelength of $\lambda = 723 \mu\text{m}$. In both cloud models, the surrounding regions of the star are also the regions of highest dust temperature. The IDG mechanism reacts sensible to both values, density and temperature, because of the threshold δ_0 (see Eq. 3.16). Therefore the efficiency of grain alignment is lowest towards the

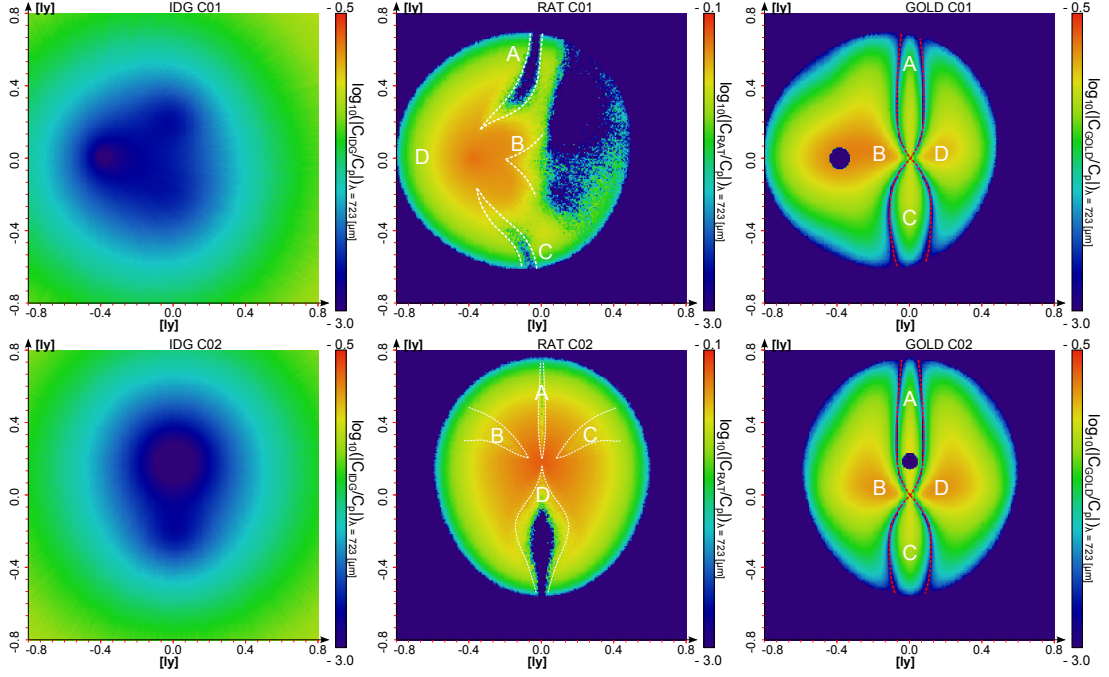


Figure 5.18: Ratio of polarization cross sections $\log_{10}(|C_x/C_p|)_{\lambda=723 \mu\text{m}}$ of imperfectly aligned dust grains C_x to perfectly aligned dust grains C_p in the mid-plane of the model space for the C01 model (top row) and C02 model (bottom row). The x stands for IDG alignment (left columns), RAT alignment (middle columns), and GOLD alignment (right columns). In the middle columns dotted white lines indicate the regions where the alignment efficiency $Q_{\Gamma}(\epsilon)$ is at its minimum. The dotted red lines in the right columns show the transition where GOLD alignment does change the sign of linear polarization.

center of the clouds and near the star (see Fig. 5.18 left panels).

The expected alignment pattern according to RAT theory is contrary to that of the IDG alignment. The emission of heated dust and stellar radiation contribute to the local energy density u_{λ} and the anisotropy parameter can reach a maximum value up to $\gamma_{\lambda} = 0.9$ in close proximity to the star. The characteristic dust grain radius a_{alg} decreases and dust grains with radii above a_{alg} become aligned. Since the process of determining the RAT alignment quantities requires two separate MC simulations (dust heating and calculation of the radiation field), the grain alignment of RATs has an inherent higher amount of noise. This becomes apparent in Fig. 5.18 (middle panel) in the inner cloud regions. Besides the amount of energy density and anisotropy, the grain alignment depends also highly on the RAT alignment efficiency $Q_{\Gamma}(\epsilon)$. This parameter, in turn, depends on the chosen dust grain geometry and has in our dust model of oblate dust grains its minimum

at angles of $\varepsilon = 0^\circ$ and $\varepsilon = 90^\circ$ between radiation and magnetic field direction. This leads to areas of reduced grain alignment indicated by white dotted lines in Fig.5.18 (middle panel). In Fig.5.18 (middle top panel), the low degree of grain alignment in the areas A and C is a direct result of the angle dependency of RAT theory because of $Q_\Gamma(\varepsilon)$. However, the low grain alignment on the left half of the panel is a result of the shielding of this region by the dense cloud cores from stellar radiation and thus the overall energy density \bar{u} remains low. The expected low grain alignment in the area D cannot be found. This is because the overall energy density \bar{u} outweighs the angle dependency in this very thin region. In Fig.5.18 (middle bottom panel), the low degree of grain alignment in the areas $A - D$ follows more clearly the angle between predominant direction of the radiation field and the magnetic field direction. This result is in excellent agreement with the expectations of the model setup shown in Fig. 5.17 and RAT theory.

Since we assume a constant supersonic velocity field, GOLD alignment alone barely depends on temperature and density. However, a dependency exists because of internal alignment (see Eq. 4.39) and the Mach-limit (see Eq. 4.45). As RAT alignment, GOLD alignment is also limited by the local magnetic field strength (see Eq. 4.44). Since the internal alignment mechanism is sensible to high temperatures this manifests itself as a sphere of completely randomized dust grains in the surrounding regions in the regions B (Fig.5.18 top right panel) and A (Fig.5.18 bottom right panel) around the star. By comparing Fig.5.18 (left panels), Fig. 5.19 (left panels), and Eq. 4.38 one can see that the dominant parameter remains the angle α between gas stream \vec{v} and magnetic field direction \vec{B} . The areas of minimal grain alignment appear along the transition where GOLD alignment changes the sign of the Rayleigh reduction factor shown as red lines in Fig.5.18 (middle panel).

Resulting maps of linear polarization for the cloud models C01 and C02 are presented in Fig. 5.19. The normalized orientation vectors of linear polarization have an offset angle of 90° to be parallel with the projected magnetic field direction.

For the IDG mechanism (Fig. 5.19 top row), the center of depolarization moves with the position of the star due to the change of the dust temperature distribution, leading to a nearly rotationally symmetrical pattern for both cloud models .

The polarization pattern for RAT alignment in the middle column of Fig. 5.18 follows the regions of highest radiation. Therefore a high polarization coincides with the position of the star. The degree of linear polarization is reduced in the C01 model along the regions of minimal grain alignment efficiency $Q_\Gamma(\varepsilon)$. The same effect can be detected in the polarization map of the C02 model. However, here this effect is less expressed leading to a butterfly-like pattern of linear polarization in the surrounding area of the star. Both, IDG and RAT alignment mechanisms, resemble the underlying hourglass field morphology. The GOLD alignment in turn can change the alignment angle along the line of sight and this subsequently changes the polarization direction.

A correlation between intensity I and polarization P_l was recognized in Henning *et al.* (2001) following the power-law $P \propto (I/I_{\max})^{-\alpha}$ where α is a fit parameter. This finding is consistent in literature of observations (see Matthews & Wilson, 2002; Lai *et al.*, 2003; Cho & Lazarian, 2005). Since the $P - I$ relation is hyperbolic in nature, one expects to find a flat tail when I/I_{\max} reaches unity making it an ideal test for the different grain alignment theories. Hence, we calculated the increasing depolarization towards lower intensities for our cloud models C01 and C02 making use of the polarization maps of Fig. 5.19. Here, each data point presents a different line of sight. We also calculated the $P - I$ relations for our cloud models rotated by 90° in order to explore a larger data set. The $P - I$ relation of the IDG mechanism shown in Fig. 5.20 (left column) is consistent with observations. Since the anisotropy in radiation and grain alignment is directly correlated and stellar radiation is the dominant source of radiation in both cloud models, the $P - I$ relation in the RAT case is less definitive. In contrast to the IDG alignment the $P - I$ relation of RAT alignment starts with an increase in polarization up to a point of $I/I_{\max} \approx 0.1$ and remains then almost constant at its maximum value. However, the RAT alignment mechanism matches the expected $P - I$ relation curvature in agreement with observations for larger fractions of I/I_{\max} .

The GOLD alignment shows an exceptional behavior. In contrast to observational findings the degree of linear polarization remains constant in the non-rotated case and increases even slightly for the rotated case. Data points show a broader scatter in comparison with other alignment mechanisms.

5.2.3.3 Discussion

The characteristic appearance of each grain alignment theory in the maps of linear polarization is often discussed to account for observational data (see Andersson, 2015, for review). So far, RAT alignment is considered to be the most promising theories of grain alignment. The observational fact that grains are better aligned in close proximity to a bright star is a strong indication of RAT alignment (Matsumura *et al.*, 2011). A direct correlation between grain alignment and the direction as well as the strength of the radiation field was also confirmed next to the star HD 97300 in the Chamaeleon I star-forming region by Andersson & Potter (2010) and Andersson *et al.* (2011). This observational findings are in accordance with the results of the synthetic linear polarization maps calculated with RAT alignment presented in this section.

The velocity dependent flip in the orientation of polarization vectors is characteristic for GOLD alignment and can help to determine areas with supersonic gas streams by observations. From the observational point of view a flip in polarization angles was reported along the direction of molecular outflows (e.g. Rao *et al.*, 1998; Cortes *et al.*, 2006). However, the rather unusual pattern of linear polarization as presented in this section

cannot be confirmed by observations so far. This may be a result of the limited set of parameters of the considered cloud models. The two main limiting factors are velocity and magnetic field strength (see Eq. 4.38 and Eq. 4.44) which were assumed to be constant for simplicity. Recent progress on the field of mechanical grain alignment also indicated that the dust grain alignment may also be efficient in sub-sonic environments (Lazarian & Hoang, 2007).

The IDG alignment has also still its place to account for the observed alignment of small dust grains (Clayton *et al.*, 1992; Hoang *et al.*, 2014). The maximum values in linear polarization are in good agreement with observation (Gonçalves *et al.*, 2005; Davidson *et al.*, 2011) for all the applied alignment mechanisms. Taking the maximal degree of linear polarization as a measurement of the prevailing alignment mechanism the polarization is clearly dominated IDG in the outer parts followed by RAT near the star. Higher linear polarization degrees can easily be achieved for RATs by increasing the free parameter $f_{\text{high-J}}$ and the upper cut off a_{max} in the grain size distribution of the applied dust models. However, exact values of these parameters are currently speculative. In contrast to the IDG and RAT alignment, models considering GOLD alignment holds the lowest degree of linear polarization indicating that the observable net polarization of the cloud would lack any flip in polarization angles. This is also consistent with the behavior of the calculated $P - I$ relations. Both RAT and GOLD alignment show an unexpected distribution of linear polarization. This uncertainty and the deviations in calculated $P - I$ relations may be resolved with more sophisticated models from dedicated MHD simulations by forthcoming parameter studies.

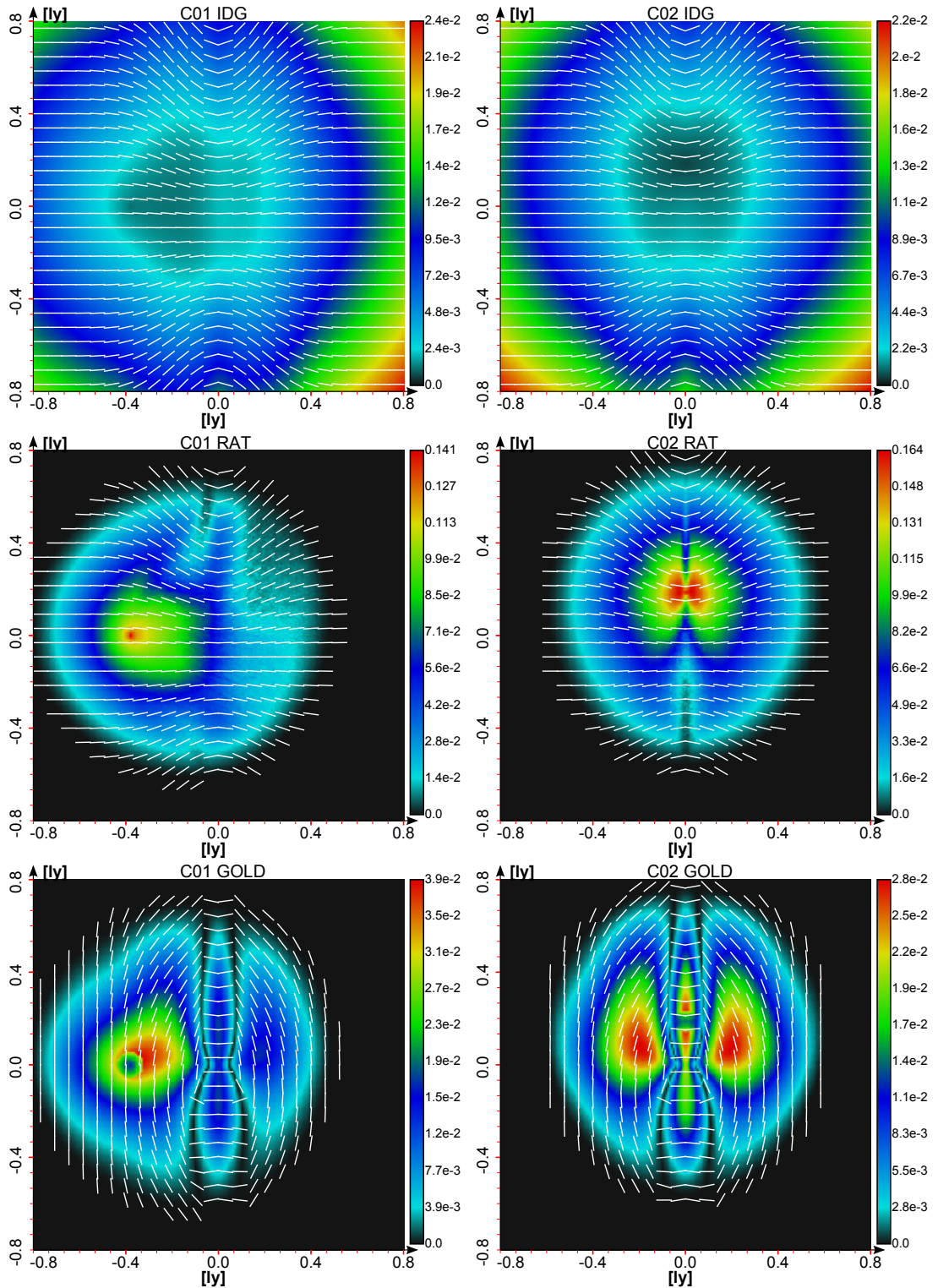


Figure 5.19: Maps with pattern of linear polarization overlaid with normalized orientation vectors at an exemplary wavelength of $\lambda = 723 \mu\text{m}$. We applied an offset of 90° to the orientation vectors to match the projected hourglass magnetic field morphology. The cloud model C01 is on the left column and the model C02 is on the right column for dust grains aligned with the IDG mechanism (top row), RAT mechanism (middle row), and GOLD mechanism (bottom row).

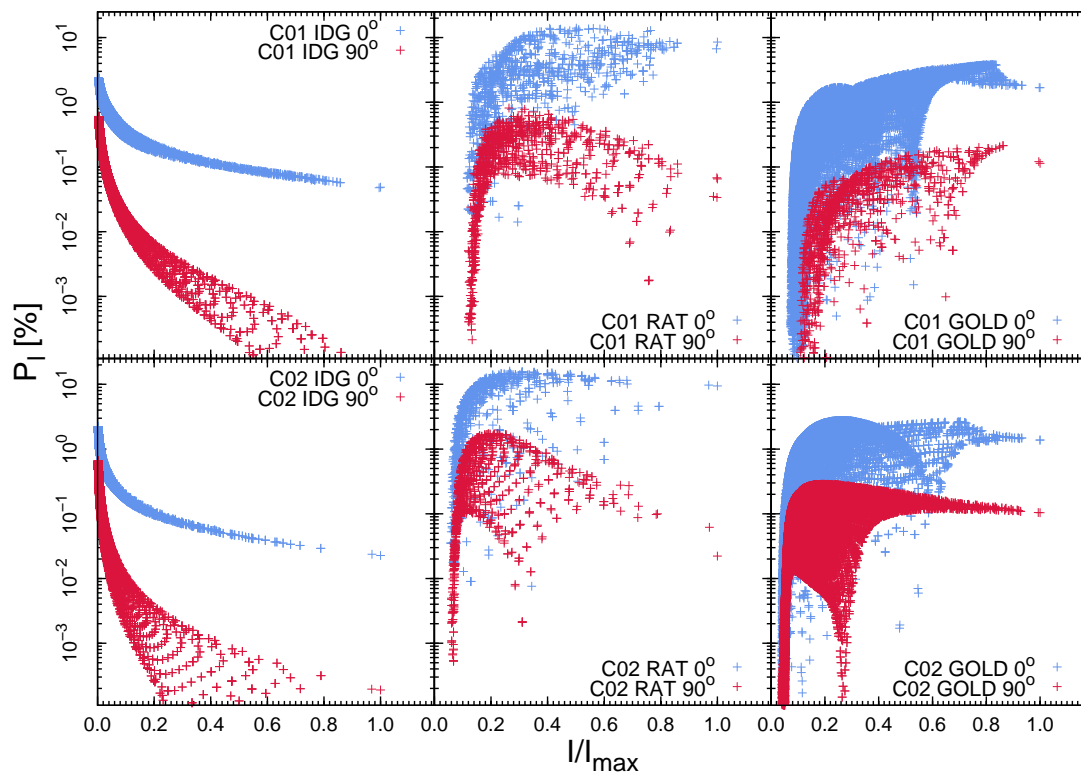


Figure 5.20: Plots of the degree of linear polarization of the C01 model (top row) and C02 model (bottom row) as a function of normalized intensity ($P-I$ relation). The results with IDG alignment (left column), RAT alignment (middle column), and GOLD alignment (right column). Blue crosses represent the original models C01 and C02 where as red crosses are the models rotated by 90° .

5.3 MHD outflow simulation

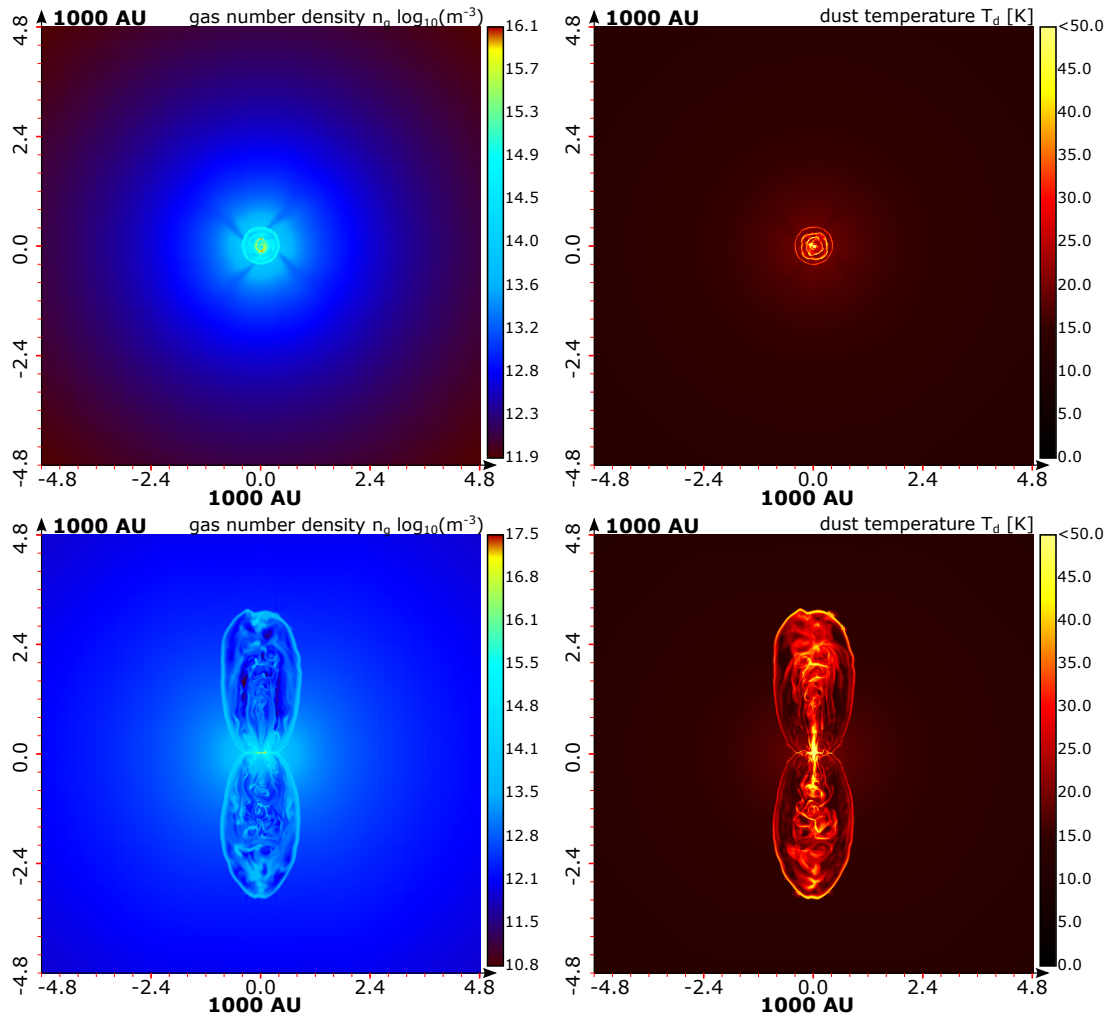


Figure 5.21: Plots of the gas number density (left column) and the adjusted dust temperature (right column) in two planes parallel (top row) and perpendicular (bottom row) to the disk of the MHD outflow simulation.

With the expected resolution of upcoming equipment (Brown *et al.*, 2004, e.g.), the coverage of cloud cores and disks reaches observable scales where effects such as rotation and turbulence become increasingly relevant. The well ordered large scale magnetic field lines are expected to be rather unordered on smaller scales e.g. in molecular outflows ejected from a proto-planetary disk. Outflows and jets seem to be a natural

consequence in the early stage of star formation. One proposed mechanism to account for outflows is the acceleration of gas by a gradient of magnetic pressure in the outflow lobes. The magnetic field morphology in this scenario is expected to possess a strong toroidal component (e.g. Tomisaka, 1998). This toroidal component is a remnant of the rotating collapsing molecular cloud. However, from an observational point of view it needs to be verified that such a toroidal field morphology would actually be detectable in the interior of outflow lobes. The magnetic field morphology in the ambient environment represents a possible source of ambiguity. Here, it is expected from non-ideal MHD considerations that ions couple directly to the magnetic field, leading to ambipolar diffusion. Subsequently, the surrounding magnetic field is hourglass shaped and therefore perpendicular orientated with respect to the toroidal component along the line of sight. However, the constraints on how to probe the complex magnetic field structures around the outflow lobes are yet unclear.

With regards to this additional level of complexity analytical models are of minor use. In order to study the magnetic field morphology with synthetic polarization measurements we apply the *POLARIS* code in the following sections to a more realistic scenario. MHD simulations of collapsing molecular clouds have proven to reproduce the complex internal density and magnetic field morphologies of outflow environments (Banerjee *et al.*, 2006) and the formation of circumstellar disks (Duffin & Pudritz, 2011) as they were expected by observations.

Hence, we focus on the post-processing of a particular MHD outflow simulation as presented in Seifried *et al.* (2011) simulated with different initial dust grain parameters and observational conditions. The MHD simulation started as a collapsing magnetized and rotating cloud and a mass of $100 M_{\odot}$ in a cube with a side length of 0.25 pc and an initially uniform magnetic field with a strength of 1.32×10^{-8} T (see Seifried *et al.*, 2011, for a detailed description). The simulation was performed with the astrophysical code *FLASH* (Fryxell *et al.*, 2000). In this simulation the core was magnetically supercritical and the magnetic field provided marginally support against the collapse. We took a snapshot after a simulation time of 5000 yr. At this point an accretion disc of about 2800 AU in diameter has formed. The disk ejects two collimated outflows with a height of 3200 AU in the surrounding medium (see Fig.5.21). As expected, in the interior of the outflow lobes a predominant magnetic field morphology is toroidal (see Fig.5.22). The field lines, however, are locally turbulent because of shocks in the outflow lobes.

5.3.1 Post-processing of the MHD outflow data

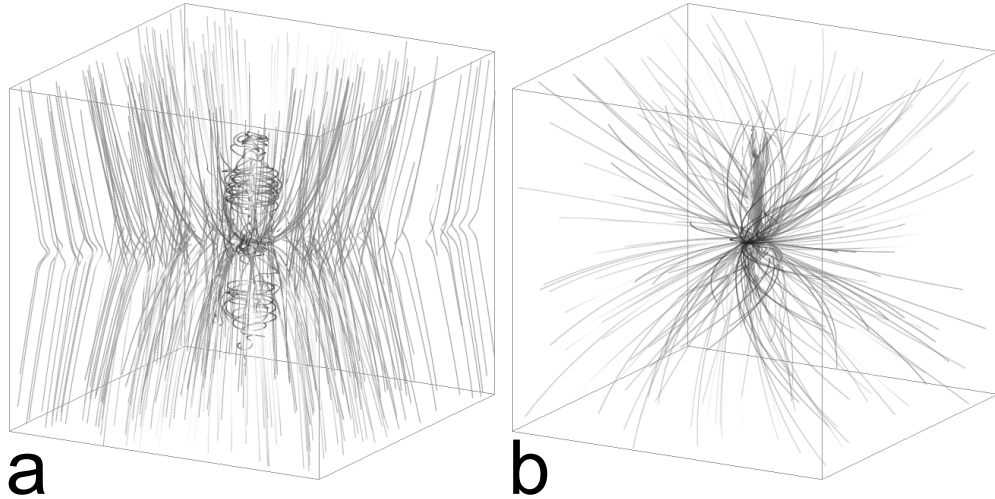


Figure 5.22: 3D plots of the magnetic field morphology (panel a) and the velocity field (panel b) of the MHD outflow simulation.

At that simulation time of 5000 yr six proto-stars have formed and the accretion disk starts to fragment. We considered three proto-stars as point sources for the adjustment of the initial dust temperature and calculated the radiation field to determine the RAT alignment efficiency. However, three proto-stars were in close proximity (< 10 AU) to each other and were handled as a single diffuse source (see Sect. 4.3) in order to decrease time required to perform the MC RT simulations. We considered also the additional contribution to luminosity resulting from gas accretion towards the proto-stars. For the considered parameters of the model, the contribution of scattering to the net-polarization is minuscule. Hence, scattering can be ignored for the calculation of polarization maps. As dust model we apply the typical parameters presented in Sect. 4.6 with a variable upper cut of radius of $a_{\max} \in [0.2 \mu\text{m}, 2.0 \mu\text{m}, 200 \mu\text{m}]$. For the considered IDG alignment we assume ferromagnetic inclusions in the dust grain material in order to get a detectable polarization signal (see Sect. 3.4).

5.3.2 The choice of dust grain alignment theory

Outflow environments in general provide the conditions sufficient for IDG, RAT, and GOLD alignment theories to be effective. Consequently, the interplay of several grain alignment mechanisms simultaneously at work might cloak the toroidal magnetic field component from observation. In this section we start the investigation similar to the MC RT simulations presented in Sect. 5.2.3. Here, the characteristic pattern of linear polarization were also calculated considering the grain alignment theories separately in a regime of wavelengths of $1 \mu\text{m} - 3 \text{mm}$ with fixed inclination angle of 90° between the outflow axis and the line of sight. Later, we combine all alignment theories in an additional MC RT simulation in order to constrain the optimal observational conditions dependent on grain alignment theory.

5.3.2.1 Polarization pattern resulting from GOLD alignment

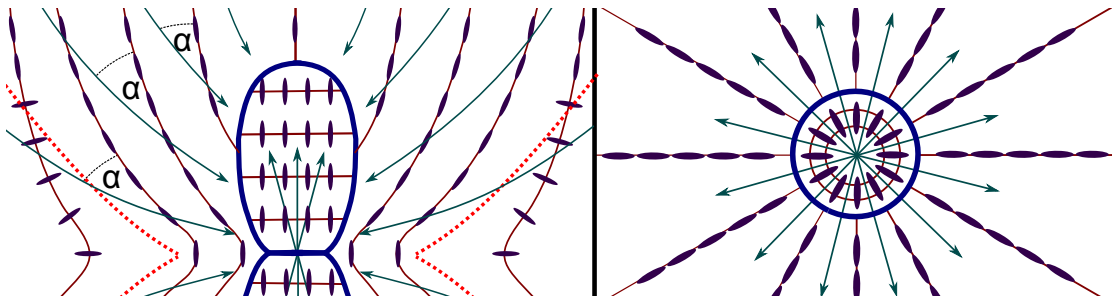


Figure 5.23: Schematic illustration of the expected dust grain (blue ellipses) alignment behavior according to GOLD alignment in the center plane perpendicular (left panel) and parallel (right panel) to the symmetry axis of the outflow lobes (dark blue). The angle α is defined to be between magnetic field direction (dark red) and the velocity field (dark green) of the gas. The contour of the critical value of α_0 where dust grains start to align with their longer axis parallel to the magnetic field is indicated by a red dotted line.

As indicated by observations (e.g. Rao *et al.*, 1998) non-spherical dust grains may not necessarily align with their minor axis parallel to the local magnetic field. As a possible explanation mechanical alignment is discussed where gas streams can cause grain alignment to flip dependent on the angle α between velocity and magnetic field.

A schematic illustration of the expected grain alignment behavior is shown in Fig. 5.23. In the outer regions, in-falling gas with an angle $\alpha < 54.7^\circ = \alpha_0$ (see Sect. 4.38) forces the dust grains to align with their major axis parallel to the magnetic field direction. From this point on the grain alignment axis is the minor one towards the rotation plane of the disk. However, for the presented configuration this limit is also never passed in

the interior of the outflow lobes since velocity field and magnetic field direction always cross at angles below α_0 .

The resulting polarization maps in a regime of wavelengths between $\lambda_{\min} = 20 \mu\text{m}$ and $\lambda_{\max} = 2 \text{mm}$ are shown in Fig. 5.25. For shorter wavelengths polarization is completely a result of dichroic extinction and the 90° flip in the origination of the polarization vectors is completely explained by the applied *GOLD* alignment. Starting at λ_{\min} we determined the wavelengths at which thermal remission contribute to the polarization pattern. As shown in Fig. 5.25 in the outer left map at a wavelength of $\lambda = 34.6 \mu\text{m}$ the polarization vector starts to rotate at the outer edges. However, the polarization of the outflow lobes and the disk remains unaffected. With increasing wavelength the rotation of polarization vectors wanders towards the center and reaches the distinct border of the outflows at $\lambda = 40.5 \mu\text{m}$. This trend continues up to $\lambda = 80.9 \mu\text{m}$ where even the polarization pattern of the disk is completely a result of dust re-emission. While the degree of linear polarization P_l is still slightly decreasing towards longer wavelengths the pattern in the polarization vectors remain almost fixed from $\lambda_{\min} = 632 \mu\text{m}$ on.

5.3.2.2 Polarization pattern resulting from RAT and IDG alignment

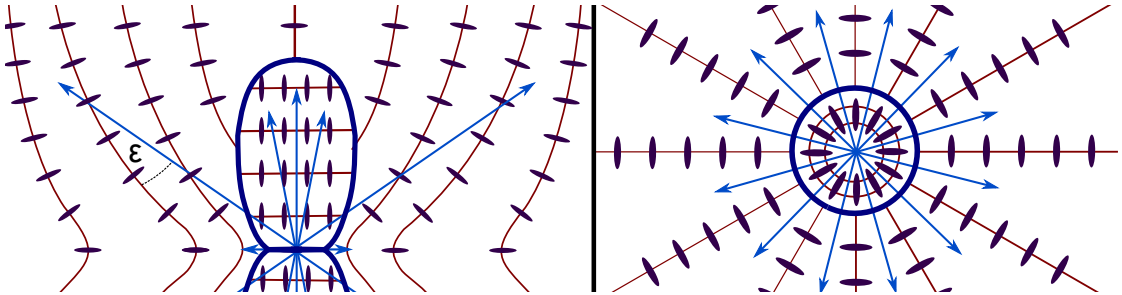


Figure 5.24: The same as in Fig. 5.23. The angle ε is defined to be between the predominant direction of the radiation (blue lines) and the magnetic field lines (dark red).

For the parameter set provided by the MHD simulation both IDG and RAT alignment theory predict globally a similar behavior with regard of the preferential axis of grain alignment. In Fig. 5.24 an illustration of expected grain alignment is shown. It needs to be emphasized that the Rayleigh reduction factors of IDG and RAT is locally not necessarily comparable. The maps of linear polarization calculated with IDG and RAT alignment theory are shown in Fig. 5.26 and Fig. 5.27, respectively.

The wavelength at which thermal re-emission starts to emerge in the polarization maps is for both IDG and RAT alignment at a wavelength of $\lambda = 40 \mu\text{m}$. The effect of flipping polarization vectors reaches the outflow lobes at $\lambda = 49.5 \mu\text{m}$ for the IDG, at $\lambda = 53.1 \mu\text{m}$ for RATs, and thermal dust re-emission dominates the entire polarization

outside the lobes at $\lambda = 107 \mu\text{m}$ for IDG alignment and at $\lambda = 86.7 \mu\text{m}$ for the case of RAT alignment, respectively. Even in the inner disk region linear polarization is completely due to thermal re-emission at a wavelength $\lambda = 551 \mu\text{m}$ for the IDG and for RAT at $\lambda = 420 \mu\text{m}$.

5.3.2.3 Polarization calculations with combined grain alignment

In order to improve the predictive capability of this investigation, we consider also the effects of combined dust grain alignment as it is presented in Sect. 5.3.2.3. The resulting maps of linear polarization as a function of wavelength are shown in Fig. 5.28. The general trend is similar to that of the single components. The first appearance of flipped polarization vectors because of thermal re-emission starts at a wavelength of $\lambda = 40 \mu\text{m}$ and spreads towards the outflow lobes at $\lambda = 65.6 \mu\text{m}$. At $\lambda = 141 \mu\text{m}$ the polarization maps are completely due to light re-emitted by the dust grains and the polarization vectors stop to change their orientation pattern at a wavelength of $\lambda = 392 \mu\text{m}$.

5.3.2.4 Comparison

The orientation angle χ of linear polarization (see Sect. 2.1.3) follows the expected behavior for the transition from extinction to dust re-emission independent of applied grain alignment theory. With increasing wavelength this transition starts at the outer edges of the model space and continues to spread towards the center regions.

Mechanical alignment can additionally flip the polarization angle. As shown in Fig. 5.25 the orientation of linear polarizations flips with decreasing distance to the plane of the disk and the center (see also Fig. 5.23). Near the critical angle of α_0 the dust grains are minimally aligned and linear polarization is at its lowest value. This would provide an opportunity to trace the angle between magnetic field and gas velocity by following the lanes of minimal polarization if we just would consider mechanical alignment alone. Combined alignment calculations, however, do not support that GOLD contributes to the overall polarization process in its characteristic manner.

In the maps considering IDG and RAT alignment the orientation of the polarization vectors can be expected to have a qualitatively similar pattern. The IDG alignment is highly suppressed in high density and temperature regions (see Sect. 3.3.2.1) and would allow no conclusion about the underlying magnetic field morphology near the disk region. For the IDG alignment the degree does not significantly contribute to the net polarization in the post-processed MDH data. Despite the consideration of ferromagnetic inclusions in the dust material the maximal degree of linear polarization is of the order of a few per cent. Since RAT alignment depends also on the alignment efficiency $Q_{\Gamma}(\varepsilon)$ (see Eq. 3.32) one could also expect to detect this characteristic in the resulting polarization pattern similar to the results of Sect. 5.2.3.

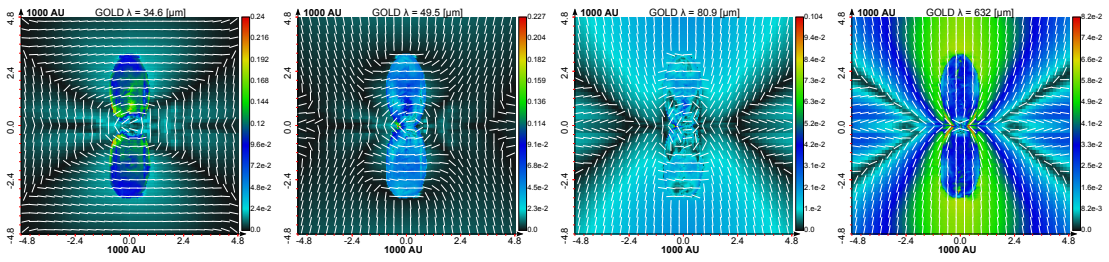


Figure 5.25: Resulting maps of the degree of linear polarization P_l (color coded) overlaid with normalized orientation vectors considering GOLD alignment at four distinct wavelengths λ .

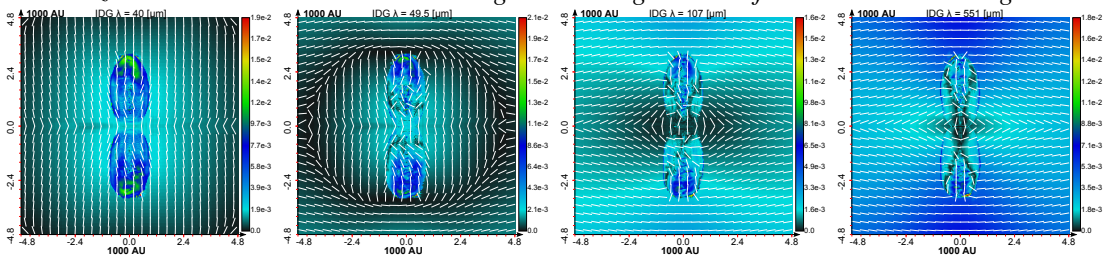


Figure 5.26: The same as Fig. 5.25 considering IDG alignment.

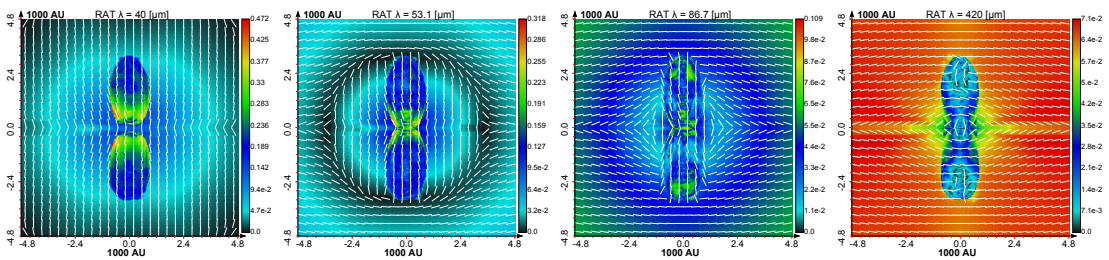


Figure 5.27: The same as Fig. 5.25 considering RAT alignment.

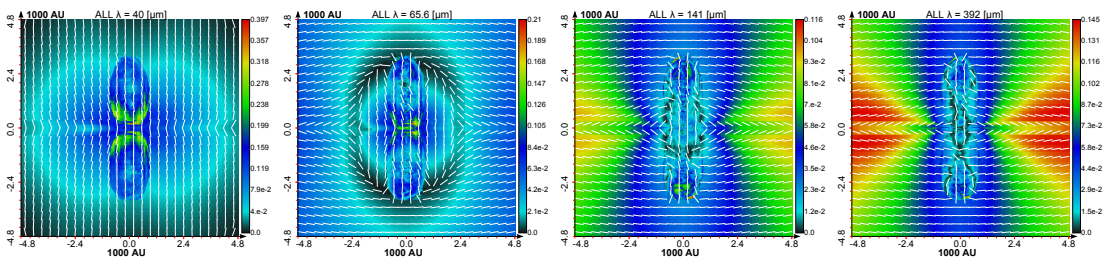


Figure 5.28: The same as Fig. 5.25 considering a combination of all three alignment mechanisms.

However, in this MHD simulation such an angle-dependent effect could just occur outside the outflow lobes. Here, the low gas density, dust temperature, and the overall radiation field are more dominant than the angle-dependency of $Q_{\Gamma}(\varepsilon)$. Therefore, the expected characteristic angle-dependency of RAT alignment cannot be seen. In the effort of combined alignment mechanisms dust grains are mostly aligned by RATs. However, by comparing Fig. 5.25 and Fig. 5.27 the pattern at longer wavelengths reveals that GOLD alignment still contributes to the degree of linear polarization in a characteristic manner other than a flip in the orientation angle. While in Fig. 5.27 at a wavelength of $\lambda = 420 \mu\text{m}$ the outer regions are highly polarized, the degree of polarization is reduced by GOLD alignment in Fig. 5.28 from a wavelength of $\lambda = 141 \mu\text{m}$ on. However, this effect seems not to affect the orientation of the polarization vectors. The degree of circular polarization reaches maximal values in the order of $\pm 10^{-3} - \pm 10^{-2}$ (see Fig. 5.34) in the MHD outflow environment much higher than that found in Sect. 5.2.1. This may allow to measure circular polarization complementary to linear polarization in future observation mission in order to constrain the 3D magnetic field morphology. However, in contrast to Sect.5.2.1, the magnetic field is much more turbulent. Consequently, the analysis and interpretation of actually observed circumstance polarization maps may be more inconclusive even in combination with sophisticated MC RT modeling.

5.3.2.5 Impact of inclination angle

In this section we aim to investigate the dependence of linear polarization pattern as a function of the inclination towards the observer. Interpretation of polarization measurements are also limited by projection effects. For a line of sights parallel to the minor axis of the grain the dust appears also to be spherical to the passing radiation independent of grain alignment and linear polarization becomes completely suppressed (see Reissl *et al.*, 2014, for details).

Fig. 5.29 shows polarization maps for GOLD alignment for three different inclination angles i starting at $i = 0^\circ$ (face-on of the disk) in steps of 30° for a fixed wavelength of $\lambda = 1.3 \text{ mm}$. As illustrated in Fig. 5.23 the dust grain above the outflow lobes are preferentially aligned with their major axis to the direction of the magnetic field. It is impossible to disentangle the contribution from the interior and the regions outside of the lobe and the toroidal-shaped field morphology remains hidden. The same for higher inclination angles. Taking the flips in the vector of polarization into account the vector orientation match exactly the projected hourglass-field of the surrounding medium .

In Fig. 5.30 we show the exact same configurations but for the IDG alignment. In this scenario the dust grain above the outflow lobes are aligned with their minor axis parallel to the magnetic field direction. Here, the direction of linear polarization is completely a result of the interior of the outflow lobes and the disk component.

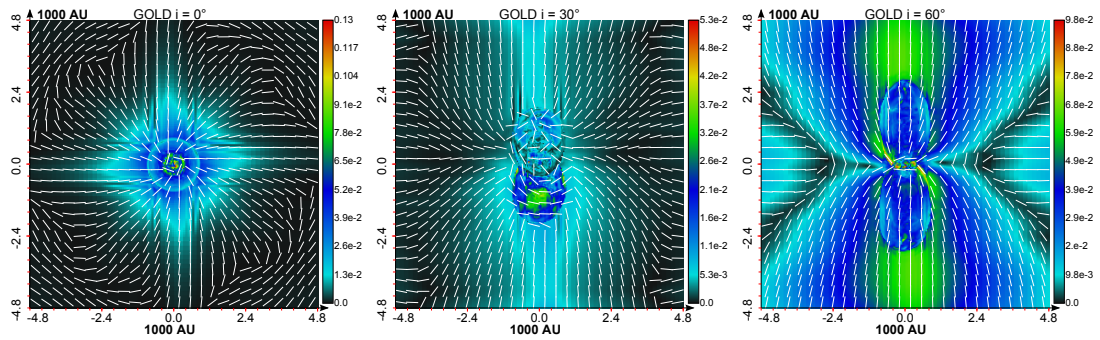


Figure 5.29: Resulting maps of the degree of linear polarization P_l (color coded) overlaid with normalized orientation vectors considering GOLD alignment at a wavelength of $\lambda = 1.3$ mm and three inclination angles i .

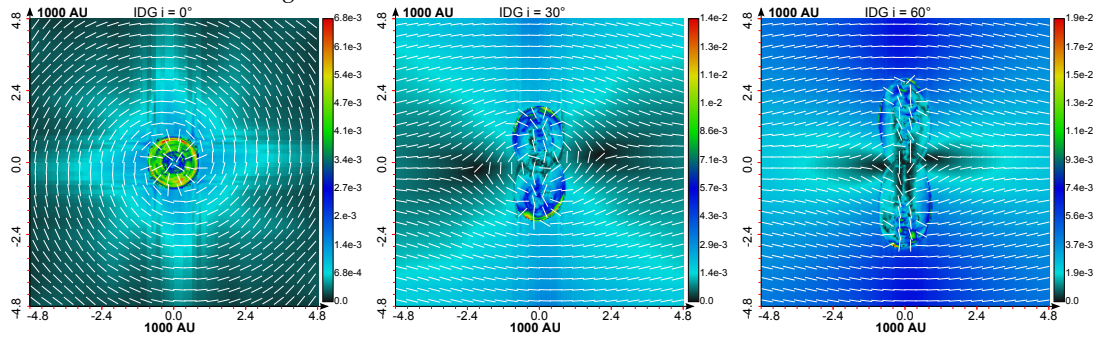


Figure 5.30: The same as Fig. 5.29 considering IDG alignment.

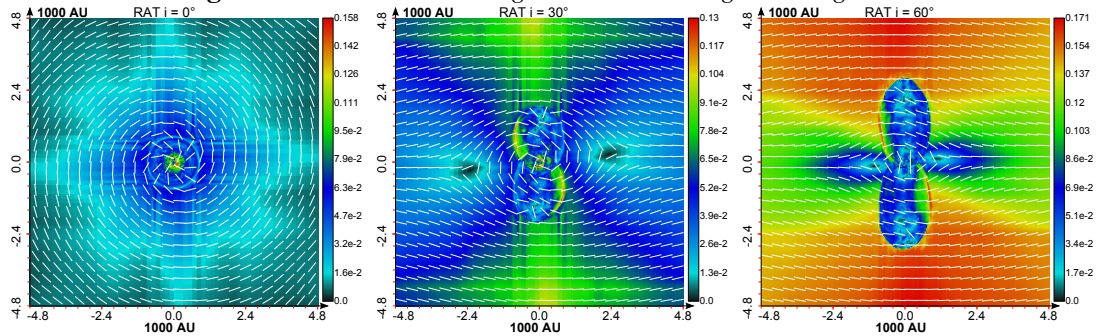


Figure 5.31: The same as Fig. 5.29 considering RAT alignment.

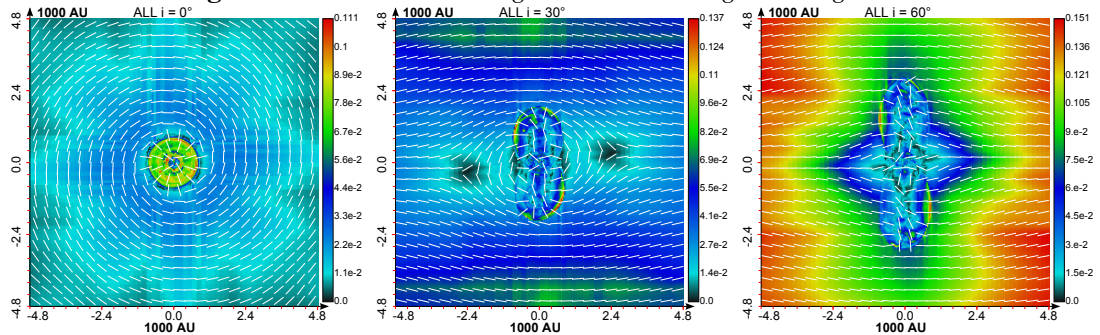


Figure 5.32: The same as Fig. 5.29 considering a combination of all three alignment mechanisms.

For an inclination angle of $i = 0^\circ$ the toroidal morphology of the magnetic field can unambiguously be identified. With increasing inclination angle the contributions from the outer magnetic field start to dominate the overall orientation of the linear polarization. For an inclination of $i = 30^\circ$ (see middle panel of Fig. 5.30, Fig. 5.31, and Fig. 5.32) the polarization pattern already resembles the projected hourglass morphology. The toroidal component of the magnetic field, however, remains apparent close to the symmetry axis and tips of the outflows.

In Fig. 5.31 we show the resulting linear polarization maps considering RAT alignment. For an inclination angle of $i = 0^\circ$ the results are qualitatively the same as the ones for IDG alignment. The magnetic field morphology of the inside of the outflow lobes and the surrounding regions can clearly be identified. However, with increasing inclination angle the contributions of the surrounding hourglass shaped magnetic field becomes even faster dominant than for IDG alignment. Here, just the tips of the outflow lobes match the toroidal magnetic field component. Linear polarization rapidly builds up in regions with magnetic field lines parallel to each other along the LOS since the direction of preferential axis of extinction and thermal re-emission of the dust remains constant. As a result of this projection effect the degree of linear polarization becomes enhanced in the surface of the outflow lobes where a transition between hourglass shaped magnetic field morphology to a toroidal field occurs (see Fig. 5.31 middle panel and right panel). The opposite effect occurs in regions with a high amount of crossing field lines along the line of sight. This effect becomes apparent in Fig. 5.31 where two holes of minimum of linear polarization (middle panel) and two extra lobes (right panel), respectively, appear perpendicular to the symmetry axis of the outflow lobes. Here, these extra holes are not a result of dust density or temperature distribution but a projection effect and an indicator of the underlying field morphology (Reissl *et al.*, 2014).

The same effect can be observed for the polarization maps with IDG alignment in Fig. 5.30 and in Fig. 5.32. Since, RAT alignment contributes the most to linear polarization in polarization maps with combined grain alignment theories, the dependency on inclination angle is quite similar. In contrast to pure RAT alignment the toroidal component remains apparent at the tops and near the symmetry axis of the outflow lobes. Due to the influence of mechanical alignment the lobes in the degree of linear polarization appear to be more edgy (Fig. 5.32 right panel). However, the orientation of linear polarization matches the projected magnetic field geometry. A flip in the orientation is not observable independent of inclination angle.

5.3.2.6 Line of sight analysis

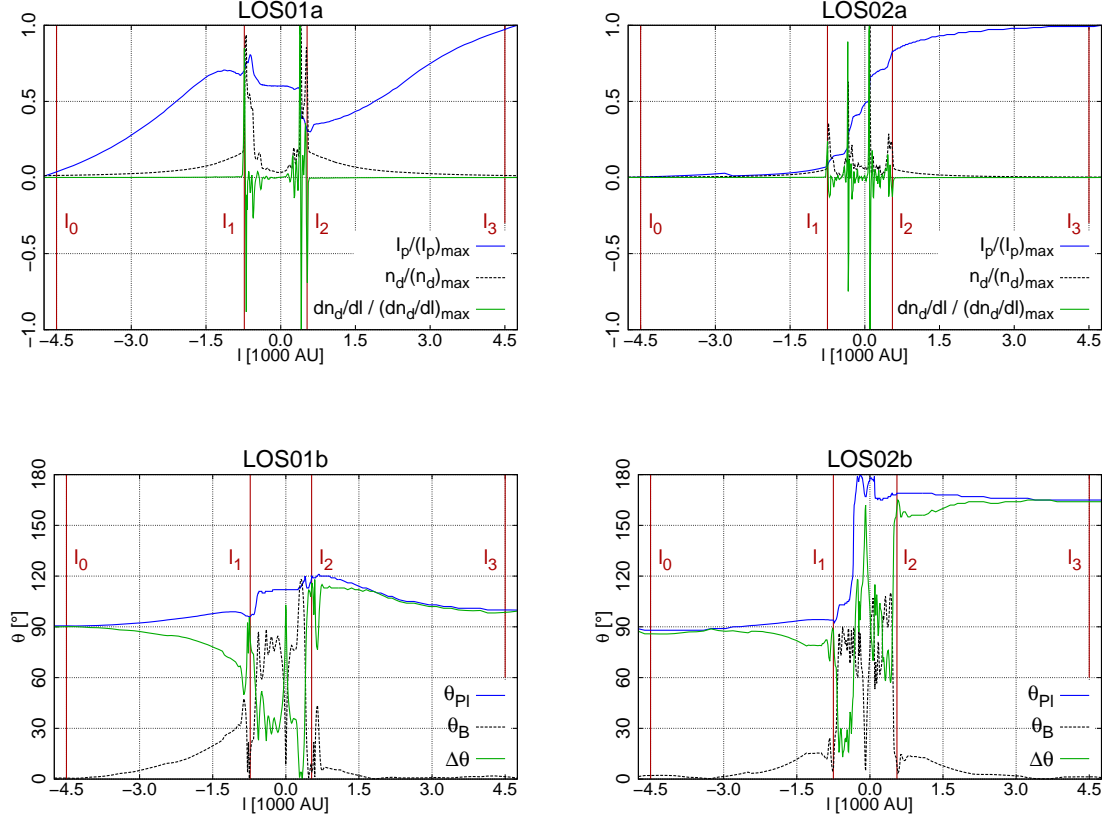


Figure 5.33: Physical quantities along the two exemplary line of sights LOS01 and LOS01. The top row shows the normalized values of polarized intensity I_p (blue), dust number density n_d (green), and its first derivative dn_d/dl (dotted black). Note, that the polarized intensity I_p is plotted as a cumulative value. The bottom row shows the orientation angles of linear polarization θ_{PI} (blue), magnetic field θ_B direction (dotted black), and their difference $\Delta\theta$ (green).

In contrast to observations, MC RT simulations allow to trace different rays through the grid and subsequently to determine the actual origin of polarization. All the synthetic polarization maps of Figs. 5.25 - 5.28 and Figs. 5.29 - 5.32 remain still ambiguous regarding the actually traced magnetic field component. Hence, we implemented an heuristic algorithm to analyze the polarization status of the light along the line of sight l .

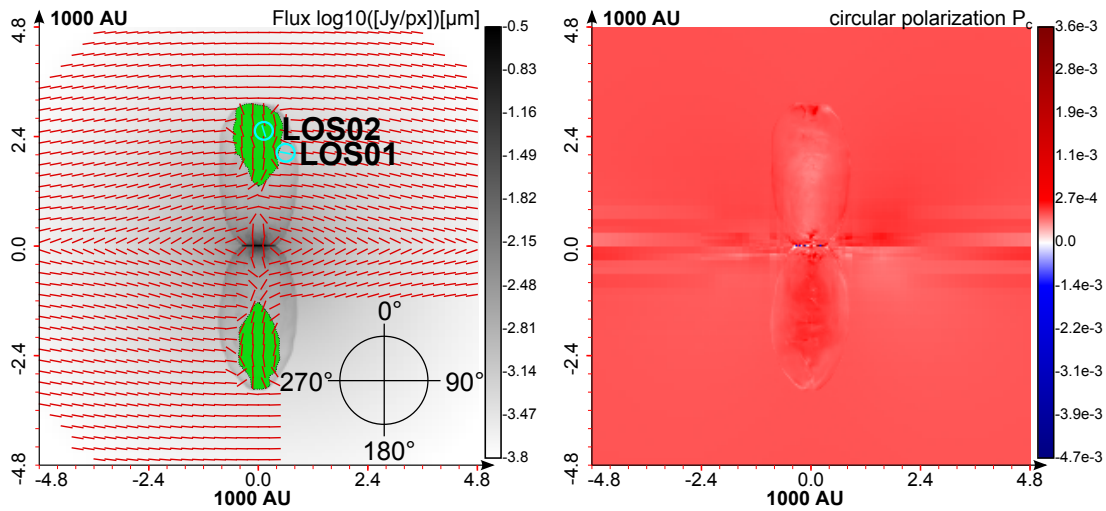


Figure 5.34: Flux map (left panel) overlaid with vectors of linear polarization and map of circular polarization (right panel) of the post-processed MHD outflow simulation. The maps are calculated for a wavelength of $\lambda = 1.3$ mm. Green regions in the flux map indicate a positive detection of the toroidal magnetic field component by the line of sight analysis. The selected line of sights (blue circles) correspond to the plot in Fig.5.33.

As a first step we have to distinguish between the areas inside and outside the outflow lobe. This can be done by a simple analysis of the characteristic slope of the number density along the line of sight. The criterion for the penetration of the outflow lobe is when the first derivative of the dust number density is $\frac{dn_d(l)}{dl} > 10$ for the first time. A similar criterion determines the end of the outflow lobe with the last occurrence of $\frac{dn_d(l)}{dl} < -10$.

Since we want to exclude possible contribution from the conditions at the borders arising because of numerical reasons we start the analysis at ± 4.5 AU. With this simple but effective heuristic we can distinguish between three regions along the line of sight, the first outside region from l_0 to l_1 , the inside region from l_1 to l_2 , and the second outside region from l_2 to l_3 . Once, the borders of the three different areas are known, the origin of linear polarization can be determined. The first criterion is the increase or decrease in polarized intensity $I_p(l)$ accumulated along the line of sight. Here it is sufficient to compare just the values of $I_p(l_0)$, $I_p(l_1)$, $I_p(l_2)$, and $I_p(l_3)$, respectively, at the borders of each area to determine the area with the largest increase. The second criterion is the resulting polarization angle with respect to the magnetic field direction characteristic for each area. Although the magnetic field direction in the outflow lobes is not well ordered and it appears rather regular in projection and can therefore be assumed to be perpendicular to the projected magnetic field direction in both outside regions.

Finally, the origin of polarization is assigned to the interior of the outflow lobes when first: The largest increase in polarized intensity is inside the outflow lobe, and second: The orientation vector of linear polarization deviates from the projected toroidal field by $\pm 23^\circ$. The exact definition of polarization angle and projected magnetic field direction is shown in Fig. 5.34 (left panel). Since the alignment of angular momentum \vec{J} parallel or anti-parallel results in the same orientation of the polarization vector, the angle of linear polarization can switch by 180° . However, this has no influence on the analysis. Here it needs to be emphasized, that this heuristic is fine tuned to probe the outflow lobes in this particular MHD simulation. The parameters of the heuristic are optimized by proper testing to minimize the false positive results. Consequently, the areas in the polarization maps where linear polarization originates from the inside of the outflow lobes can be identified with a high precision. However, the number of positive detections might actually be larger near the borders. The manual evaluation of 50 line of sights for three different inclination angles shows that the accuracy of the correct detection of the origin of linear polarization is larger than 90 %.

Fig. 5.33 shows the results of two exemplary lines of sight. In the first case (*LOS01*) the polarized intensity I_p emerges in the first outer area and has its maximum at the border of the outflow lobe and remains constant throughout the interior and reaches its maximum at the border of the grid. The orientation angle θ_{pl} remains at a value of roughly 90° with respect to the magnetic field orientation θ_B and gets slightly increased near the border of the outflow lobe. In the interior the polarization angle remains almost constant and trends back to 90° as the radiation propagates towards the border of the model space. In this case the interior of the outflow lobe is of minor influence to linear polarization with respect to degree and orientation and the line of sight *LOS01* clearly does not probe the toroidal component of the magnetic field morphology. In the second case (*LOS02*), I_p remains marginal until the border of the outflow lobe. Here, the large increase in polarized intensity coincides clearly with the number density n_d . The amount of I_p does slightly increase until the order of the model space. The orientation angle θ_{pl} remains at around 90° . However, in the center of the outflow lobe the value of θ_{pl} jumps by 90° and matches now the toroidal field component. In this case the resulting linear polarization allows to probe the interior of the magnetic field component (see also Fig.5.22 left panel). Areas of positive detection of the line of sight analysis are green colored in Fig.5.34 (left panel) and Fig.5.35.

5.3.2.7 Grain size dependency

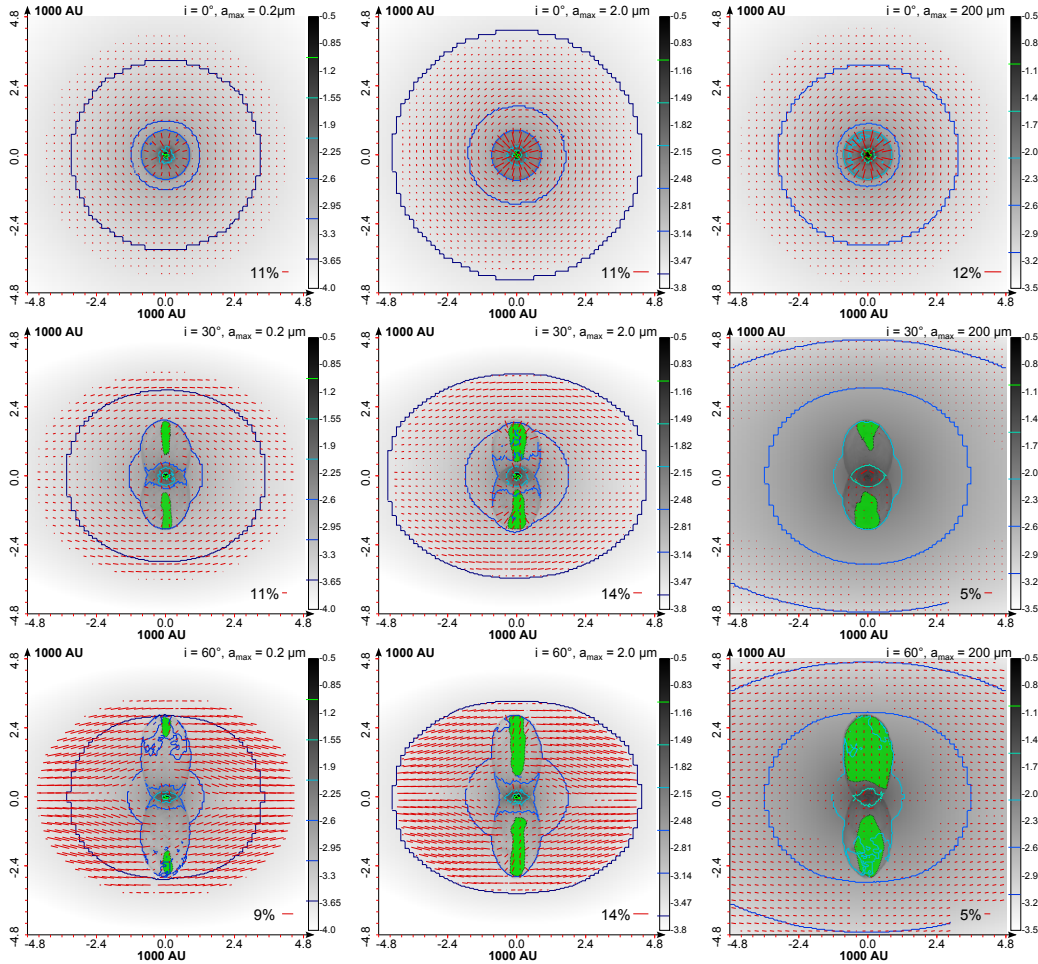


Figure 5.35: Flux maps (color coded) at a wavelength of $\lambda = 1.3$ mm overlaid with vectors of linear polarization considering a combination of all three alignment mechanisms (see Sect. 5.3.2.3) for an inclination angle of $i = 0^\circ$ (top row), $i = 30^\circ$ (middle row), and $i = 60^\circ$ (bottom row) and with maximal dust grain radii of $a_{\max} = 250$ nm (left column), $a_{\max} = 2$ μm (middle column), and $a_{\max} = 200$ μm (right column). The length of the vectors depends on the degree of linear polarization. For the flux an upper cut off of $F_{\max} = -0.5$ [$\log_{10}(Jy/px)$] was applied for better comparison. The contour lines show constant flux from $2F_{\max}$ (green) to $7F_{\max}$ (dark blue) in steps of F_{\max} .

Dust grains in the ISM are very likely to have a size distribution from $a \approx 10$ nm to $a \approx 100$ nm. However, all the data show clear evidence that grains in proto-planetary disks and outflow differ significantly from grains in the diffuse ISM. Grain growth in

the disk is expected to enrich the surrounding environment along the outflow lobes with dust grain sized of up to 1 mm (e.g. Sahai *et al.*, 2006). In this section, we will now bring the effects of combined dust grain alignment mechanisms and inclination angle together and review how grain size alters the pattern of linear polarization. The sizes of dust grains cannot be expected to be evenly distributed in all regions since larger dust grains are forged in the disk. However, we apply here a simpler dust model with constant size parameter throughout the model space. As described in Sect.4.6, the optical quantities of dust grain sizes up to an upper cut-off radius of $a_{\max} = 2$ mm where already pre-calculated. With this data we determined the influence of dust grain sizes in the synthetic intensity and polarization maps by repeating the post-processing of the MHD data for the calculation pipeline as described in Sect. 5.3.1 for two additional distinct cut-off radii of $a_{\max} = 250$ nm and $a_{\max} = 200$ μ m. Furthermore, we also performed the line of sight analysis introduced in Sect. 5.3.2.6 to the results of both additional simulations.

With exception of the disk regions the resulting dust temperature distribution differs only by a few Kelvin between the simulations with different cut-off radii. The resulting maps of flux overlaid with the vectors of linear polarization are shown in Fig. 5.35 for three different inclination angles and maximal cut-off radii. The linear polarization was calculated taking all three classes of grain alignment into account (see Sect. 5.3.2.3). For the Flux we assumed a distance of 100 pc between the object of interests and the observer. All maps were overlaid with green areas showing the results of the line of sight analysis where the toroidal field component dominates the polarization. The maps in Fig. 5.35 (left column) were calculated with the standard MRN model with an upper cut off $a_{\max} = 250$ nm. In this model MC RT calculations showed that the maximum size of RAT alignment (see Sect. 3.3.2.4) exceeded the upper cut of radius in a considerable amount of cells ($a_{\text{alg}} \geq a_{\max}$). One could expect a lower degree of linear polarization, however, due to the lack of larger dust grains the mode with $a_{\max} = 250$ nm is optically thinner compared to the other models with larger cut off radii. This results in less extinction and consequently flux and polarization remains similar to the model with $a_{\max} = 2$ μ m shown in Fig. 5.35 (middle column). The model with $a_{\max} = 200$ μ m is shown in Fig 5.35 (right column). Dust grains of maximal size are quite rare in the dust mixture because of the standard MRN power-law size distribution (see Sect. 4.6). However, the higher re-emission cross sections C_{abs} of larger dust grains compensate their lower abundance (see Fig. 4.9 upper right panel). This results in a higher flux for the model with $a_{\max} = 200$ μ m compared to the other models by a factor of ≈ 2 . Additionally, with increasing cut-off radii the polarization along the line of sight becomes also rapidly dominated by larger dust grains. However, in the range of wavelengths where $\lambda \approx a$ the cross section of re-emitted polarization has the lowest values of ΔC_{abs} (see Fig. 4.9 lower right panels) compared to smaller dust grain sizes. Consequently, the ma-

ximal degree of linear polarization is reduced for the model with $a_{\max} = 200 \mu\text{m}$. The overall pattern of linear polarization vectors seems to be independent of the cut-off radius. The trend with increasing inclination angle is similar to that described in Sect. 5.3.2.5. Here, lower inclination angles are also more suitable to distinguish the hourglass magnetic field morphology in the outer regions from the toroidal field in the outflow lobes.

5.3.2.8 Discussion

Observations of polarized thermal dust re-emission in star forming regions (Lai *et al.*, 2002; Cortes & Crutcher, 2006; Cortes *et al.*, 2008) generally indicate a smooth magnetic field morphology. Considering the available spatial resolution, however, contributions because of turbulence might be averaged out and the magnetic field morphology appears on such scales more well ordered as it actually is. Indeed, observations of nearby star forming regions (Rao *et al.*, 1998; Cortes & Crutcher, 2006) reveal abrupt changes in the orientation angles of the polarization vectors and show the contribution of turbulence to the polarization along the line of sight on smaller scales. The possibility of mechanical alignment is suggested in Rao *et al.* (1998) as an alternative explanation to turbulence. This can not be supported by the results of Sect. 5.3.2.3. The MC RT simulations show only a marginal contribution of GOLD alignment to the net polarization. The same holds for IDG alignment. In this outflow environment, the grain alignment by RAT theory is clearly the most dominant factor. This holds even though the applied method of combining the dust grain alignment mechanisms allows just for qualitatively statements. None of the applied grain alignment theories can account for the unordered small scale structure of linear polarization vectors. Hence, it follows that the vectors of linear polarization directly map the actual twists in the magnetic field morphology along the line of sight. Here, it needs to be emphasized, that this just holds for this particular post-processed MHD outflow simulation as described in Sect. 5.3. As the results of similar simulations might reveal, mechanical alignment can indeed flip the orientation of polarization in different circumstances.

Additionally, the resulting synthetic maps of intensity and polarization of the post-processed MHD outflow simulation are limited by the assumed distribution of dust grain sizes. In order to improve the accuracy of the modeling in this section, the dust grain sizes should not be evenly distributed in the entire model space. As stated in Sect. 5.3.2.7 larger dust grains are most likely to be more common near the disk region. This has consequences to the results of the line of sight analysis. As it was demonstrated in Sect. 5.3.2 and Sect. 5.3.2.4, the dominant mechanism of grain alignment are RATs. With smaller dust grains near the tips of the outflow lobes and the surrounding medium, the contribution to the net polarization in such areas would decrease. Consequently, the green areas

in Fig.5.35 where the toroidal field component would definitely be detectable would shrink at the tips of the outflow lobes.

Although the direction of polarization vectors remains unaltered by GOLD alignment, a flip in the orientation angle can be observed for shorter wavelengths. By comparison of the calculated maps of linear polarization in Figs. 5.25 - 5.28 at a wavelength of roughly $100 \mu\text{m}$ one can falsely conclude that the orientation of linear polarization would allow to trace the toroidal field morphology in the outflow lobes. However, up to a wavelength of $\lambda \approx 100 \mu\text{m}$ this is completely a result of the interplay of dichroic extinction and thermal re-emission. The resulting pattern of linear polarization is completely dominated by the magnetic field in the surrounding medium. By rotating polarization vectors accordingly they would perfectly match the projected hourglass-shaped magnetic field in the outer regions. This is consistent with the findings of the line of sight analysis. The toroidal field component is just detectable close to the symmetry axis of disk and the tips of the outflow lobes in the far-IR and the sub-mm. This finding has a larger impact to observations such as the findings of Chapman *et al.* (2013). Here, they report a strong correlation between the direction of the magnetic field lines in low-mass cores and the bipolar outflows. However, as shown in this section, the origin of the polarization remains ambiguous at best and cannot be simply concluded by observations alone. In order to claim a correlation it requires a MC RT modeling to ensure that the observed wavelengths are actually suitable to probe the regions of interest in the first place.

Chapter 6

Conclusive remarks

6.1 Summary and Conclusions

In the present thesis, the polarization effects caused by partially aligned dust grains were studied to evaluate their potential and accuracy as a technique to trace the magnetic field morphology in the ISM and, subsequently, to improve our knowledge about the physical processes involved in the star-formation process. For this reason we simulated and evaluated synthetic multi-wavelength maps of intensity as well as linear and circular polarization of several astrophysical systems associated with star formation. With the help of this maps we constrained the parameters on multiple scales that would allow to infer the underlying magnetic field morphology. The ambiguities inherent in this approach are manifold.

First of all, the RT problem has to be solved in astrophysical environments where the physical quantities span several orders of magnitude. This cannot be done by means of an analytical approach. In chapter 2 we described the basic RT equations and introduced the MC approach as a tool to solve the RT problem independent of complexity. Since, we focused on the concepts particularly related to the MC simulation for heating and scattering on spherical dust grains.

In chapter 3 we dealt with the major source of ambiguity, the dust component of the ISM itself. Here, the parameters of the dust component, such as size distribution and composition of the dust grains are not well constrained. Additionally, the alignment efficiency of dust grains cannot be well calculated by a single consistent theory. Furthermore, we presented in this chapter the standard model of interstellar dust and the available theories of dust grain alignment considered in this thesis. Based on the standard model, we created a dust grain database for non-spherical dust grains ranging over multiple orders of dust grain sizes as well as wavelengths. This database allows for MC RT heating and polarization calculations of partially aligned dust grains.

A tool suitable to perform MC RT simulations considering the full range of polarization effects of non-spherical dust grains was not available so far. In chapter 4 we merge the standard concepts of MC RT simulations as they were presented in chapter 2 for spherical dust grains with the physics of non-spherical dust grains as well as the three major classes of grain alignment theories of chapter 3. Here, we focus on the adjustments of standard MC techniques and the mathematical approximations to perform MC RT simulations in reasonable times scales. This efforts resulted in the *POLARIS* code capable of simulating the physics of partially aligned dust grains in order to create synthetic intensity and polarization maps. Finally, this made it possible to evaluate the potential of multi-wavelength continuum polarization measurements on multiple scales to deduce the morphology of magnetic fields in regions with ongoing star-formation.

In chapter 5 we perform MC RT simulations with analytical input models and post-process data from sophisticated MHD simulations. However, in a first step we establish the reliability of the *POLARIS* code to perform accurate dust heating and polarization calculations in section 5.1 and investigate open questions related to MC RT simulations with non-spherical dust grains. The results of creating polarization maps from analytical models can be summarized as follows:

- The post-processing of data resulting from MHD simulations requires to consider both sources of dust heating, the heating because of compression and that of radiative heating. Otherwise vital information of gas density structure or the newly born stars emerging in the MHD simulation gets lost in the resulting synthetic intensity maps.
- For the adjustment of the dust temperature as the first step of the post-processing pipeline, the alignment of the dust grains is of minor relevance. Hence, it can be neglected in dust heating simulations. Furthermore, the resulting 3D dust temperature distribution is also independent of chosen phase function. Consequently, MC RT dust heating calculations can be performed most efficiently with the less time consuming HG phase function and randomly aligned dust grains.
- The comparison of the *POLARIS* code with the well established MC RT code *MC3D* shows that both codes produce similar results within limitations characteristic of each code. However, this limitations are a result of different grid geometries and optimization techniques.

Once the accuracy of the *POLARIS* code was established, we started the investigation of magnetic field morphology within a controlled environment density and magnetic field morphologies modeled by analytical functions. Here, we conclude that:

- Under low inclination angles different field morphologies can appear similar in the resulting synthetic maps of linear polarization.

- Characteristic pattern of circular polarization emerge from distinct magnetic field morphologies. This allows to distinguish between different field morphologies even under low inclination. Hence, the complimentary measurement of circular polarization can provide a source of additional information in future observations.
- The orientation vectors of linear polarization are also dependent on wavelength. We probe different regions along the line of sight. Each area dominates the resulting net polarization dependent on density and temperature as well as magnetic field strength and grain alignment efficiencies. For this reason observations of distinct wavelengths are insufficient to determine the underlying magnetic field morphology. However, continuum dust polarization measurements on multiple scales seem to allow to determine the morphology of the magnetic field in certain astrophysical environments such as Bog globules.
- The potential of aligned dust grains to detect the magnetic field morphology in circumstellar disks is more ambiguous. Theoretical models predict a detectible degree of linear polarization should emerge from such an environment. Although our MC RT modeling shows similar results to that of the theoretical predictions, observations of selected disks do not agree with this findings. This hints that additional physical processes, such as dust settling, must additionally taken into account.
- As MC RT simulations within an artificial cloud environment as input showed synthetic polarization maps are highly dependent on the considered dust grain alignment theory. Since a consistent theory of dust grain alignment is still missing this adds an additional source of ambiguity in the modeling of synthetic polarization maps because each theory alters the polarization pattern in a unique way.

Finally in chapter 5.3.1 we created synthetic polarization maps with data from sophisticated MHD outflow simulations as input data for the *POLARIS* code. With this approach we overcome the artificial nature of the analytical models. The main focus here was to constrain the parameters necessary to probe the magnetic field morphology in the interior of the outflow lobes. The results of this approach can be summarized as follows:

- An additional source of ambiguity is inherent in the polarization of aligned dust grains itself. The competing mechanism of dichroic extinction and thermal re-emission. With increasingly longer wavelengths, the transition between the regimes of wavelengths dominated by dichroic extinction and thermal re-emission manifests itself in a flip of the orientation angles of 90° in linear polarization. Additionally, areas where these transition takes place are depolarized and the magnetic field morphology is no longer accessible by observations.

- The alignment of dust grains does not result in polarization when the line of sight is parallel to the magnetic field direction. This effect is independent of considered dust grain alignment theory and wavelength. However, this fact is of advantage in this particular case of the post-processed molecular outflows MHD simulation because it allowed to probe the interior of the outflow lobes under certain inclination angles.
- Artificial polarization maps have been calculated considering different grain alignment theories. This maps revealed that polarization in this particular outflow environment is clearly dominated by RAT alignment theory. Possible flips in the orientation of polarization vectors as predicted by observation as a result of GOLD alignment do not appear. However, this holds just true for the investigated MHD simulation and might not hold in general.
- The observability of the interior of the outflow lobes depends also on the maximal size of the dust grain composition. A dust grain composition with larger dust grains lead to higher intensity but lower polarization and vice versa for a smaller maximal dust grain size.
- Under an observational point of view the best conditions to probe the interior of the outflow lobes is under an inclination angle of 0° - 60° for a wavelength regime starting in the FIR ($\approx 600\mu m$) to the sub-mm. Ideally the system posses a MRN dust grain size distribution with an upper cut-off in the order of $\approx 1\mu m$.

6.2 Outlook

In this thesis the utility and the parameters of dust grains partially aligned with the magnetic field direction have been constrained to determine the magnetic field morphology in many astrophysical systems in the ISM. However, the potential of this kind of approach especially in combination with further numerical techniques is far from being exhausted.

Size distribution, shapes, and composition of the dust grains are not well constrained. Furthermore, the dust grains are far more complex structured than it could have been considered in the dust grain model applied in this thesis. This grain model needs further improvement in order to increase the accuracy of the MC RT simulations. A more sophisticated model would include layered dust grains with ice mantles (Greenberg, 1978) and a porous structure (e.g. Zubko *et al.*, 1998). Such multi-layered structures could be modeled by the *DDSCAT* code (Draine & Flatau, 2013; Kirchschrager & Wolf, 2014) and should be considered in upcoming studies in order to take care of the actual

fractal nature of the dust grain shapes. This requires also a treatment of dust grain alignment away from the analytical solutions applied in this thesis towards parametrized approaches as they were presented e.g. in Lazarian & Hoang (2007), Hoang & Lazarian (2007), and Hoang *et al.* (2014) for RAT, GOLD, and IDG alignment, respectively. Such a parametrization would also allow to include pinwheel torques (see Sect. 3.4) as proposed by Hoang *et al.* (2015) to complete the picture of dust grain alignment theories in our MC RT simulations. The ratio of atomic to molecular hydrogen required by pinwheel torques can easily be delivered by state of the art multi-gas-phase MHD simulations (e.g. Walch *et al.*, 2015).

As it was demonstrated in this thesis, the tracing of the magnetic field morphology with aligned dust grains has its limitations and ambiguities (see chapter 5). In order to overcome these limitations, the numerical methods applied in this thesis can be combined with additional emission, absorption, and polarization effects in MC RT simulations. The Zeeman effect provides such an opportunity to study the magnetic field e.g. of stars (Rosén *et al.*, 2015; Lehmann *et al.*, 2015) by light polarization. Additional information to constrain the physical parameters of the ISM can be achieved by including the characteristic line emission and absorption of molecules in the ISM. The consideration of both effects in MC RT simulations can complete our efforts to increase the accuracy to model and interpret available observational data. The proof of concept that the Zeeman effect can be calculated by RT simulations was presented in Larsson *et al.* (2014) and the line radiative transfer is already a common feature in RT MC codes (e.g. Ober *et al.*, 2015).

With the advent of next generation observational equipment such as the Submillimeter Array (SMA) polarimeter (Marrone & Rao, 2008), the Atacama Large Millimeter Array (ALMA) (Brown *et al.*, 2004), and the high-resolution Airborne Wideband Camera-plus instrument of the Airborne Stratospheric Observatory For Infrared Astronomy (HAWC+/SOFIA) (Dowell *et al.*, 2013), observations by means of dust polarization measurement can resolve even small-scale structures in the order of ≈ 0.1 arcsec. This would allow to compare actual observational data with the high-resolution continuum synthetic polarization maps presented in this thesis. Finally, the synthetic intensity and polarization maps require a further post-processing to mimic the influence of observational equipment. In the simplest case this means binning the synthetic data to the instrumental resolution followed by proper convolution of the data by the characteristic point spread function. For some equipment such as ALMA, a software package developed for this purpose is already publicly available (see e.g. Petry & CASA Development Team, 2012, for details). This would be the final step to bridge the gap between synthetic data and actual observations. Hence, in future we can extract further information from observational data by modeling of synthetic polarization maps and, subsequently, this will reveal new phenomena related to the star formation process itself.

Bibliography

- Aannestad, P. A. & Greenberg, J. M. 1983: *Interstellar polarization, grain growth, and alignment*, ApJ, 272, 551
- Aannestad, P. A. & Purcell, E. M. 1973: *Interstellar Grains*, ARA&A, 11, 309
- Abbas, M. M., Craven, P. D., Spann, J. F., Tankosic, D., LeClair, A., Gallagher, D. L., West, E. A., Weingartner, J. C., Witherow, W. K., & Tielens, A. G. G. M. 2004: *Laboratory Experiments on Rotation and Alignment of the Analogs of Interstellar Dust Grains by Radiation*, ApJ, 614, 781
- Andersson, B.-G. 2015: *Interstellar Grain Alignment: Observational Status*, in Astrophysics and Space Science Library, Vol. 407, Astrophysics and Space Science Library, ed. A. Lazarian, E. M. de Gouveia Dal Pino, & C. Melioli, 59
- Andersson, B.-G., Pintado, O., Potter, S. B., Straižys, V., & Charcos-Llorens, M. 2011: *Angle-dependent radiative grain alignment. Confirmation of a magnetic field - radiation anisotropy angle dependence on the efficiency of interstellar grain alignment*, A&AS, 534, A19
- Andersson, B.-G. & Potter, S. B. 2010: *Observations of Enhanced Radiative Grain Alignment Near HD 97300*, ApJ, 720, 1045
- Baes, M., Verstappen, J., De Looze, I., Fritz, J., Saftly, W., Vidal Pérez, E., Stalevski, M., & Valcke, S. 2011: *Efficient Three-dimensional NLTE Dust Radiative Transfer with SKIRT*, ApJ, 196, 22
- Banerjee, R., Pudritz, R. E., & Anderson, D. W. 2006: *Supersonic turbulence, filamentary accretion and the rapid assembly of massive stars and discs*, MNRAS, 373, 1091
- Barnett, S. J. 1917: *Magnetization by Rotation*, Phys. Rev
- Bastien, P., Jenness, T., & Molnar, J. 2005: *A Polarimeter for SCUBA-2*, in Astronomical Society of the Pacific Conference Series, Vol. 343, Astronomical Polarimetry: Current

- Status and Future Directions, ed. A. Adamson, C. Aspin, C. Davis, & T. Fujiyoshi, 69
- Bethell, T. J., Chepurnov, A., Lazarian, A., & Kim, J. 2007: *Polarization of Dust Emission in Clumpy Molecular Clouds and Cores*, ApJ, 663, 1055
- Beuther, H., Vlemmings, W. H. T., Rao, R., & van der Tak, F. F. S. 2010: *Magnetic Field Structure in a High-mass Outflow/Disk System*, ApJ, 724, L113
- Bevington, P. R. 1969, Data Reduction and Error Analysis for the Physical Sciences, 1st edn. (McGraw Hill), 40
- Bjorkman, J. E. & Wood, K. 2001: *Radiative Equilibrium and Temperature Correction in Monte Carlo Radiation Transfer*, ApJ, 554, 615
- Bohren, C. F. & Huffman, D. R. 1983, Absorption and scattering of light by small particles
- Bonnor, W. B. 1956: *Boyle's Law and gravitational instability*, MNRAS, 116, 351
- Boulanger, F., Cox, P., & Jones, A. P. 2000: *Course 7: Dust in the Interstellar Medium*, in *Infrared Space Astronomy, Today and Tomorrow*, ed. F. Casoli, J. Lequeux, & F. David, 251
- Bradley, J. P. 1994: *Chemically Anomalous, Preaccretionally Irradiated Grains in Interplanetary Dust From Comets*, Science, 265, 925
- Brown, R. L., Wild, W., & Cunningham, C. 2004: *ALMA - the Atacama large millimeter array*, Advances in Space Research, 34, 555
- Cashwell, E. & Everett, C. 1959, A Practical Manual on the Monte Carlo Method for Random Walk Problems (Oxford,UK: Pergamon Press)
- Chandrasekhar, S. & Fermi, E. 1953: *Magnetic Fields in Spiral Arms.*, ApJ, 118, 113
- Chapman, N. L., Davidson, J. A., Goldsmith, P. F., Houde, M., Kwon, W., Li, Z.-Y., Looney, L. W., Matthews, B., Matthews, T. G., Novak, G., Peng, R., et al. 2013: *Alignment between Flattened Protostellar Infall Envelopes and Ambient Magnetic Fields*, ApJ, 770, 151
- Cho, J. & Lazarian, A. 2005: *Grain Alignment by Radiation in Dark Clouds and Cores*, ApJ, 631, 361

- Cho, J. & Lazarian, A. 2007: *Grain Alignment and Polarized Emission from Magnetized T Tauri Disks*, ApJ, 669, 1085
- Clayton, G. C., Anderson, C. M., Magalhaes, A. M., Code, A. D., Nordsieck, K. H., Meade, M. R., Wolff, M. J., Babler, B., Bjorkman, K. S., Schulte-Ladbeck, R. E., Taylor, M., et al. 1992: *The first spectropolarimetric study of the wavelength dependence of interstellar polarization in the ultraviolet*, ApJ, 385, L53
- Clayton, G. C., Wolff, M. J., Allen, R. G., & Lupie, O. L. 1995: *Ultraviolet interstellar linear polarization. 2: The wavelength dependence*, ApJ, 445, 947
- Clayton, G. C., Wolff, M. J., Sofia, U. J., Gordon, K. D., & Misselt, K. A. 2003: *Dust Grain Size Distributions from MRN to MEM*, ApJ, 588, 871
- Clemens, D. P., Yun, J. L., & Heyer, M. H. 1991: *BOK globules and small molecular clouds - Deep IRAS photometry and (C-12)O spectroscopy*, ApJ, 75, 877
- Cortes, P. & Crutcher, R. M. 2006: *Interferometric Mapping of Magnetic Fields: G30.79 FIR 10*, ApJ, 639, 965
- Cortes, P. C., Crutcher, R. M., & Matthews, B. C. 2006: *Interferometric Mapping of Magnetic Fields: NGC 2071IR*, ApJ, 650, 246
- Cortes, P. C., Crutcher, R. M., Shepherd, D. S., & Bronfman, L. 2008: *Interferometric Mapping of Magnetic Fields: The Massive Star-forming Region G34.4+0.23 MM*, ApJ, 676, 464
- Crutcher, R. M. 1999: *Magnetic Fields in Molecular Clouds: Observations Confront Theory*, ApJ, 520, 706
- Crutcher, R. M., Hakobian, N., & Troland, T. H. 2008: *Response to the Mouschovias-Tassis Comments on "Testing Magnetic Star Formation Theory"*, ArXiv e-prints: 0808.1150
- Crutcher, R. M., Nutter, D. J., Ward-Thompson, D., & Kirk, J. M. 2004: *SCUBA Polarization Measurements of the Magnetic Field Strengths in the L183, L1544, and L43 Prestellar Cores*, ApJ, 600, 279
- Crutcher, R. M., Wandelt, B., Heiles, C., Falgarone, E., & Troland, T. H. 2010: *Magnetic Fields in Interstellar Clouds from Zeeman Observations: Inference of Total Field Strengths by Bayesian Analysis*, ApJ, 725, 466

- Das, H. K., Voshchinnikov, N. V., & Il'in, V. B. 2010: *Interstellar extinction and polarization - a spheroidal dust grain approach perspective*, MNRAS, 404, 265
- Davidson, J. A., Novak, G., Matthews, T. G., Matthews, B., Goldsmith, P. F., Chapman, N., Volgenau, N. H., Vaillancourt, J. E., & Attard, M. 2011: *Magnetic Field Structure Around Low-mass Class 0 Protostars: B335, L1527, and IC348-SMM2*, ApJ, 732, 97
- Davis, Jr., L. 1955: *Theories of interstellar polarization*, Vistas in Astronomy, 1, 336
- Davis, Jr., L. & Greenstein, J. L. 1951: *The Polarization of Starlight by Aligned Dust Grains.*, ApJ, 114, 206
- Debye, P. 1909: *Der Lichtdruck auf Kugeln von beliebigem Material*, Annalen der Physik, 30, 57
- DeVoe, H. 1964: *Optical properties of molecular aggregates. I. Classical model of electronic absorption and refraction*, J. Chem. Phys, 41, 393
- Dolginov, A. Z. 1974: *Alignment of interstellar and interplanetary grains*, SOVAST, 18, 33
- Dolginov, A. Z. & Mitrofanov, I. G. 1976a: *Orientation of cosmic dust grains*, Ap&SS, 43, 291
- Dolginov, A. Z. & Mitrofanov, I. G. 1976b: *Possibility of studying the interplanetary magnetic field on the basis of circular polarization of zodiacal light*, Akademiia Nauk SSSR Izvestiia Serii Fizicheskoi, 40, 484
- Dowell, C. D., Staguhn, J., Harper, D. A., Ames, T. J., Benford, D. J., Berthoud, M., Chapman, N. L., Chuss, D. T., Dotson, J. L., Irwin, K. D., Jhabvala, C. A., et al. 2013: *HAWC+: A Detector, Polarimetry, and Narrow-Band Imaging Upgrade to SOFIA's Far-Infrared Facility Camera*, in American Astronomical Society Meeting Abstracts, Vol. 221, American Astronomical Society Meeting Abstracts, 345.14
- Draine, B. T. 1988: *The discrete-dipole approximation and its application to interstellar graphite grains*, ApJ, 333, 848
- Draine, B. T. 2003: *Scattering by Interstellar Dust Grains. I. Optical and Ultraviolet*, ApJ, 598, 1017
- Draine, B. T. & Flatau, P. J. 1994: *Discrete-Dipole Approximation For Scattering Calculations*, J. Opt. Soc. Am. A, 11, 1491

- Draine, B. T. & Flatau, P. J. 2013: *User Guide for the Discrete Dipole Approximation Code DDSCAT 7.3*, ArXiv e-prints
- Draine, B. T. & Li, A. 2001: *Infrared Emission from Interstellar Dust. I. Stochastic Heating of Small Grains*, ApJ, 551, 807
- Draine, B. T. & Li, A. 2007: *Infrared Emission from Interstellar Dust. IV. The Silicate-Graphite-PAH Model in the Post-Spitzer Era*, ApJ, 657, 810
- Draine, B. T. & Malhotra, S. 1993: *On graphite and the 2175 Å extinction profile*, ApJ, 414, 632
- Draine, B. T. & Weingartner, J. C. 1996: *Radiative Torques on Interstellar Grains. I. Superthermal Spin-up*, ApJ, 470, 551
- Draine, B. T. & Weingartner, J. C. 1997: *Radiative Torques on Interstellar Grains. II. Grain Alignment*, ApJ, 480, 633
- Duffin, D. F. & Pudritz, R. E. 2011: *Discs, outflows, and feedback in collapsing magnetized cores*, in IAU Symposium, Vol. 270, Computational Star Formation, ed. J. Alves, B. G. Elmegreen, J. M. Girart, & V. Trimble, 291–295
- Dullemond, C. P. 2012: *RADMC-3D: A multi-purpose radiative transfer tool*, Astrophysics Source Code Library
- Ebert, R. 1955: *Über die Verdichtung von H I-Gebieten. Mit 5 Textabbildungen*, ZAp, 37, 217
- Elmegreen, B. G. 2000: *Star Formation in a Crossing Time*, ApJ, 530, 277
- Ercolano, B., Barlow, M. J., Storey, P. J., & Liu, X.-W. 2003: *MOCASSIN: a fully three-dimensional Monte Carlo photoionization code*, MNRAS, 340, 1136
- Falgarone, E., Puget, J. L., & Perault, M. 1986: *Fragmented molecular complexes: The role of the magnetic field in feeding internal supersonic motions*, in Interstellar Processes: Abstracts of Contributed Papers, ed. D. J. Hollenbach & H. A. Thronson, Jr., 165
- Falgarone, E., Troland, T. H., Crutcher, R. M., & Paubert, G. 2008: *CN Zeeman measurements in star formation regions*, A&A, 487, 247
- Ferrière, K. M. 2001: *The interstellar environment of our galaxy*, Reviews of Modern Physics, 73, 1031

- Fiege, J. D. & Pudritz, R. E. 2000: *Polarized Submillimeter Emission from Filamentary Molecular Clouds*, ApJ, 544, 830
- Fixsen, D. J. 2009: *The Temperature of the Cosmic Microwave Background*, ApJ, 707, 916
- Frau, P., Galli, D., & Girart, J. M. 2011: *Comparing star formation models with interferometric observations of the protostar NGC 1333 IRAS 4A. I. Magnetohydrodynamic collapse models*, A&A, 535, A44
- Fryxell, B., Olson, K., Ricker, P., Timmes, F. X., Zingale, M., Lamb, D. Q., MacNeice, P., Rosner, R., Truran, J. W., & Tufo, H. 2000: *FLASH: An Adaptive Mesh Hydrodynamics Code for Modeling Astrophysical Thermonuclear Flashes*, ApJS, 131, 273
- Galli, D. & Shu, F. H. 1993: *Collapse of Magnetized Molecular Cloud Cores. II. Numerical Results*, ApJ, 417, 243
- Girart, J. M., Beltrán, M. T., Zhang, Q., Rao, R., & Estalella, R. 2009: *Magnetic Fields in the Formation of Massive Stars*, Science, 324, 1408
- Girart, J. M., Crutcher, R. M., & Rao, R. 1999: *Detection of Polarized CO Emission from the Molecular Outflow in NGC 1333 IRAS 4A*, ApJ, 525, L109
- Girart, J. M., Rao, R., & Marrone, D. P. 2006: *Magnetic Fields in the Formation of Sun-Like Stars*, Science, 313, 812
- Gold, T. 1952: *The alignment of galactic dust*, MNRAS, 112, 215
- Gonçalves, J., Galli, D., & Walmsley, M. 2005: *Polarized dust emission of magnetized molecular cloud cores*, A&A, 430, 979
- Goodman, A. A., Benson, P. J., Fuller, G. A., & Myers, P. C. 1993: *Dense cores in dark clouds. VIII - Velocity gradients*, ApJ, 406, 528
- Greenberg, J. M. 1968, *Interstellar Grains* (the University of Chicago Press), 221
- Greenberg, J. M. 1978, *Interstellar dust*, ed. J. A. M. McDonnell, 187–294
- Hall, J. S. 1949: *Observations of the Polarized Light from Stars*, Science, 109, 166
- Hall, J. S. & Mikesell, A. H. 1949: *Observations of polarized light from stars.*, AJ, 54, 187

- Harries, T. 2014: *TORUS: Radiation transport and hydrodynamics code*, Astrophysics Source Code Library
- Henning, T., Wolf, S., Launhardt, R., & Waters, R. 2001: *Measurements of the Magnetic Field Geometry and Strength in Bok Globules*, *ApJ*, 561, 871
- Henry, L. G. & Greenstein, J. L. 1941: *Diffuse radiation in the Galaxy*, *ApJ*, 93, 70
- Hildebrand, R. H. & Dragovan, M. 1995: *The Shapes and Alignment Properties of Interstellar Dust Grains*, *ApJ*, 450, 663
- Hiltner, W. A. 1949: *Polarization of Radiation from Distant Stars by the Interstellar Medium*, *Natur*, 163, 283
- Hoang, T. & Lazarian, A. 2007: *Radiative Torque Alignment: Essential Physical Processes*, in *Bulletin of the American Astronomical Society*, Vol. 39, American Astronomical Society Meeting Abstracts #210, 187
- Hoang, T. & Lazarian, A. 2009: *Grain Alignment Induced by Radiative Torques: Effects of Internal Relaxation of Energy and Complex Radiation Field*, *ApJ*, 697, 1316
- Hoang, T. & Lazarian, A. 2014: *Grain alignment by radiative torques in special conditions and implications*, *MNRAS*, 438, 680
- Hoang, T., Lazarian, A., & Andersson, B.-G. 2015: *Modelling grain alignment by radiative torques and hydrogen formation torques in reflection nebula*, *MNRAS*, 448, 1178
- Hoang, T., Lazarian, A., & Martin, P. G. 2014: *Paramagnetic Alignment of Small Grains: A Novel Method for Measuring Interstellar Magnetic Fields*, *ApJ*, 790, 6
- Hong, S. S. 1985: *Henry-Greenstein representation of the mean volume scattering phase function for zodiacal dust*, *A&A*, 146, 67
- Hughes, A. M., Wilner, D. J., Cho, J., Marrone, D. P., Lazarian, A., Andrews, S. M., & Rao, R. 2009: *Stringent Limits on the Polarized Submillimeter Emission from Protoplanetary Disks*, *ApJ*, 704, 1204
- Ivezic, Z., Groenewegen, M. A. T., Men'shchikov, A., & Szczerba, R. 1997: *Benchmark problems for dust radiative transfer*, *MNRAS*, 291, 121
- Jones, R. V. & Spitzer, Jr., L. 1967: *Magnetic Alignment of Interstellar Grains*, *ApJ*, 147, 943

- Juvela, M. 1999: *Monte Carlo Radiative Transfer Calculations with Clumpy Cloud Models*, in *The Physics and Chemistry of the Interstellar Medium*, ed. V. Ossenkopf, J. Stutzki, & G. Winnewisser, 220
- Kaplan, S. A. & Pikel'Ner, S. B. 1970, *Matter in space - The interstellar medium*.
- Keto, E. & Field, G. 2005: *Dark Cloud Cores and Gravitational Decoupling from Turbulent Flows*, *ApJ*, 635, 1151
- Kim, S.-H. & Martin, P. G. 1995: *The size distribution of interstellar dust particles as determined from polarization: Spheroids*, *ApJ*, 444, 293
- Kirchschrager, F. & Wolf, S. 2014: *Effect of dust grain porosity on the appearance of protoplanetary disks*, *A&A*, 568, A103
- Klessen, R. S., Ballesteros-Paredes, J., Li, Y., & Mac Low, M.-M. 2004: *Gravoturbulent Star Cluster Formation*, in *Astronomical Society of the Pacific Conference Series*, Vol. 322, *The Formation and Evolution of Massive Young Star Clusters*, ed. H. J. G. L. M. Lamers, L. J. Smith, & A. Nota, 299–308
- Krumholz, M. R., Klein, R. I., & McKee, C. F. 2007: *Radiation-Hydrodynamic Simulations of Collapse and Fragmentation in Massive Protostellar Cores*, *ApJ*, 656, 959
- Lai, S.-P., Crutcher, R. M., Girart, J. M., & Rao, R. 2002: *Interferometric Mapping of Magnetic Fields in Star-forming Regions. II. NGC 2024 FIR 5*, *ApJ*, 566, 925
- Lai, S.-P., Girart, J. M., & Crutcher, R. M. 2003: *Interferometric Mapping of Magnetic Fields in Star-forming Regions. III. Dust and CO Polarization in DR 21(OH)*, *ApJ*, 598, 392
- Larsson, R., Buehler, S. A., Eriksson, P., & Mendrok, J. 2014: *A treatment of the Zeeman effect using Stokes formalism and its implementation in the Atmospheric Radiative Transfer Simulator (ARTS)*, *J. Quant. Spectrosc. Radiat. Transfer*, 133, 445
- Launhardt, R. & Henning, T. 1997: *Millimetre dust emission from northern BOK globules*, *A&A*, 326, 329
- Lazarian, A. 1994: *Gold-Type Mechanisms of Grain Alignment*, *MNRAS*, 268, 713
- Lazarian, A. 1995: *Mechanical Alignment of Suprathermally Rotating Grains*, *ApJ*, 451, 660

- Lazarian, A. 1996: *Mechanical Alignment of Suprathermal Grains*, in Astronomical Society of the Pacific Conference Series, Vol. 97, Polarimetry of the Interstellar Medium, ed. W. G. Roberge & D. C. B. Whittet, 425
- Lazarian, A. 1997: *Gold Alignment and Internal Dissipation*, ApJ, 483, 296
- Lazarian, A. 2007: *Tracing magnetic fields with aligned grains*, J. Quant. Spectrosc. Radiat. Transfer, 106, 225
- Lazarian, A. & Hoang, T. 2007: *Subsonic Mechanical Alignment of Irregular Grains*, ApJ, 669, L77
- Lazarian, A. & Roberge, W. G. 1997a: *Barnett Relaxation in Thermally Rotating Grains*, ApJ, 484, 230
- Lazarian, A. & Roberge, W. G. 1997b: *Cosmic rays and grain alignment*, MNRAS, 287, 941
- Lehmann, L. T., Künstler, A., & Carroll, T. A. 2015: *Magnetic field measurements of ϵ Eridani from Zeeman broadening*, Astronomische Nachrichten, 336, 258
- Lucas, P. W., Fukagawa, M., Tamura, M., Beckford, A. F., Itoh, Y., Murakawa, K., Suto, H., Hayashi, S. S., Oasa, Y., Naoi, T., Doi, Y., et al. 2004: *High-resolution imaging polarimetry of HL Tau and magnetic field structure*, MNRAS, 352, 1347
- Lucy, L. B. 1999: *Computing radiative equilibria with Monte Carlo techniques*, A&A, 344, 282
- Marrone, D. P. & Rao, R. 2008: *The submillimeter array polarimeter*, in Society of Photo-Optical Instrumentation Engineers (SPIE) Conference Series, Vol. 7020, Millimeter and Submillimeter Detectors and Instrumentation for Astronomy IV, 70202B
- Martin, P. G. 1971: *On interstellar grain alignment by a magnetic field*, MNRAS, 153, 279
- Martin, P. G. 1974: *Interstellar polarization from a medium with changing grain alignment.*, ApJ, 187, 461
- Martin, P. G. 1995: *On the value of GEMS (glass with embedded metal and sulphides)*, ApJ, 445, L63
- Martin, P. G. 2007: *On Predicting the Polarization of Low Frequency Emission by Diffuse Interstellar Dust*, in EAS Publications Series, Vol. 23, EAS Publications Series, ed. M.-A. Miville-Deschênes & F. Boulanger, 165–188

- Martin, P. G. & Angel, J. R. P. 1976: *Systematic variations in the wavelength dependence of interstellar circular polarization*, ApJ, 207, 126
- Mathis, J. S. 1986: *The alignment of interstellar grains*, ApJ, 308, 281
- Mathis, Rumpl, & Nordsieck. 1977: *The size distribution of interstellar grains*, ApJ, 217, 425
- Matsumura, M., Kameura, Y., Kawabata, K. S., Akitaya, H., Isogai, M., & Seki, M. 2011: *Correlation between Interstellar Polarization and Dust Temperature: Is the Alignment of Grains by Radiative Torques Ubiquitous?*, PASJ, 63, L43
- Matthews, B. C. & Wilson, C. D. 2002: *Magnetic Fields in Star-forming Molecular Clouds. V. Submillimeter Polarization of the Barnard 1 Dark Cloud*, ApJ, 574, 822
- McKee, C. F. & Ostriker, E. C. 2007: *Theory of Star Formation*, A&A Rev., 45, 565
- McKee, C. F. & Ostriker, J. P. 1977: *A theory of the interstellar medium - Three components regulated by supernova explosions in an inhomogeneous substrate*, ApJ, 218, 148
- Mestel, L. 1966: *The magnetic field of a contracting gas cloud. I, Strict flux-freezing*, MNRAS, 133, 265
- Mie, G. 1908: *Beiträge zur Optik trüber Medien, speziell kolloidaler Metallösungen*, Annalen der Physik, 330, 377
- Min, M., Dullemond, C. P., Dominik, C., de Koter, A., & Hovenier, J. W. 2009: *Radiative transfer in very optically thick circumstellar disks*, A&A, 497, 155
- Moskalenko, I. V., Porter, T. A., & Strong, A. W. 2006: *Attenuation of Very High Energy Gamma Rays by the Milky Way Interstellar Radiation Field*, ApJ, 640, L155
- Mouschovias, T. C. & Ciolek, G. E. 1999: *Magnetic Fields and Star Formation: A Theory Reaching Adulthood*, in NATO ASIC Proc. 540: The Origin of Stars and Planetary Systems, ed. C. J. Lada & N. D. Kylafis, 305
- Myers, P. C. 1987: *Observations of molecular cloud structure and internal motions*, in Astrophysics and Space Science Library, Vol. 134, Interstellar Processes, ed. D. J. Hollenbach & H. A. Thronson, Jr., 71–86
- Niccolini, G., Lopez, B., & Dutrey, A. 2001: *Monte Carlo radiative transfer in dusty media*, in SF2A-2001: Semaine de l’Astrophysique Française, ed. F. Combes, D. Barret, & F. Thévenin, 65

- Novak, G., Chuss, D. T., Davidson, J. A., Dotson, J. L., Dowell, C. D., Hildebrand, R. H., Houde, M., Kirby, L., Krejny, M., Lazarian, A., Li, H.-b., et al. 2004: *A polarimetry module for CSO/SHARC-II*, in Society of Photo-Optical Instrumentation Engineers (SPIE) Conference Series, Vol. 5498, Z-Spec: a broadband millimeter-wave grating spectrometer: design, construction, and first cryogenic measurements, ed. C. M. Bradford, P. A. R. Ade, J. E. Aguirre, J. J. Bock, M. Dragovan, L. Duband, L. Earle, J. Glenn, H. Matsuhara, B. J. Naylor, H. T. Nguyen, M. Yun, & J. Zmuidzinas, 278–289
- Ober, F., Wolf, S., Uribe, A. L., & Klahr, H. H. 2015: *Tracing planet-induced structures in circumstellar disks using molecular lines*, A&A, 579, A105
- Petry, D. & CASA Development Team. 2012: *Analysing ALMA Data with CASA*, in Astronomical Society of the Pacific Conference Series, Vol. 461, Astronomical Data Analysis Software and Systems XXI, ed. P. Ballester, D. Egret, & N. P. F. Lorente, 849
- Purcell, E. M. 1969: *On the alignment of interstellar dust*, Physica, 41, 100
- Purcell, E. M. 1975, Interstellar grains as pinwheels (Field, G. B. and Cameron, A. G. W.), 155–167
- Purcell, E. M. 1979: *Suprathermal rotation of interstellar grains*, ApJ, 231, 404
- Purcell, E. M. & Pennypacker, C. R. 1973: *Scattering and Absorption of Light by Nonspherical Dielectric Grains*, ApJ, 186, 705
- Rao, R., Crutcher, R. M., Plambeck, R. L., & Wright, M. C. H. 1998: *High-Resolution Millimeter-Wave Mapping of Linearly Polarized Dust Emission: Magnetic Field Structure in Orion*, ApJ, 502, L75
- Reissl, S., Wolf, S., & Seifried, D. 2014: *Tracing the ISM magnetic field morphology: the potential of multi-wavelength polarization measurements*, A&A, 566, A65
- Roberge, W. G. & Lazarian, A. 1999: *Davis-Greenstein alignment of oblate spheroidal grains*, MNRAS, 305, 615
- Robitaille, T. 2013: *Three-dimensional dust continuum radiative transfer with HYPERRION*, in Protostars and Planets VI Posters, 1
- Robitaille, T. P. 2010: *On the modified random walk algorithm for Monte-Carlo radiation transfer*, A&AS, 520, A70

- Rosén, L., Kochukhov, O., & Wade, G. A. 2015: *First Zeeman Doppler Imaging of a Cool Star Using all Four Stokes Parameters*, ApJ, 805, 169
- Sahai, R., Young, K., Patel, N. A., Sánchez Contreras, C., & Morris, M. 2006: *A Massive Bipolar Outflow and a Dusty Torus with Large Grains in the Preplanetary Nebula IRAS 22036+5306*, ApJ, 653, 1241
- Seifried, D., Banerjee, R., Klessen, R. S., Duffin, D., & Pudritz, R. E. 2011: *Magnetic fields during the early stages of massive star formation - I. Accretion and disc evolution*, MNRAS, 417, 1054
- Shakura, N. I. & Sunyaev, R. A. 1973: *Black holes in binary systems. Observational appearance.*, A&A, 24, 337
- Sharma, S. K. & Roy, A. K. 2008: *On the Validity of Phase Functions Used in Calculations of Electromagnetic Wave Scattering by Interstellar Dust*, ApJ, 177, 546
- Sipilä, O., Harju, J., & Juvela, M. 2011: *On the stability of non-isothermal Bonnor-Ebert spheres*, A&A, 535, A49
- Sorrell, W. H. 1995: *Interstellar polarization and magnetic alignment of pinwheel dust grains - II. Grain alignment efficiency*, MNRAS, 273, 187
- Spitzer, Jr., L. & McGlynn, T. A. 1979: *Disorientation of interstellar grains in suprathermal rotation*, ApJ, 231, 417
- Steinacker, J., Bacmann, A., & Henning, T. 2006: *Ray Tracing for Complex Astrophysical High-opacity Structures*, ApJ, 645, 920
- Steinacker, J. & Henning, T. 2003: *Detection of Gaps in Circumstellar Disks*, ApJ, 583, L35
- Tamura, M., Hough, J. H., Greaves, J. S., Morino, J.-I., Chrysostomou, A., Holland, W. S., & Momose, M. 1999: *First Detection of Submillimeter Polarization from T Tauri Stars*, ApJ, 525, 832
- Tanaka, H., Himeno, Y., & Ida, S. 2005: *Dust Growth and Settling in Protoplanetary Disks and Disk Spectral Energy Distributions. I. Laminar Disks*, ApJ, 625, 414
- Tang, Y.-W., Ho, P. T. P., Koch, P. M., & Rao, R. 2010: *High-angular Resolution Dust Polarization Measurements: Shaped B-field Lines in the Massive Star-forming Region Orion BN/KL*, ApJ, 717, 1262

- Tomisaka, K. 1998: *Collapse-Driven Outflow in Star-Forming Molecular Cores*, ApJ, 502, L163
- Tomisaka, K. 2011: *Origin of Molecular Outflow Determined from Thermal Dust Polarization*, PASJ, 63, 147
- van de Hulst, H. C. 1981, Light scattering by small particles
- van Zadelhoff, G.-J., Dullemond, C. P., van der Tak, F. F. S., Yates, J. A., Doty, S. D., Ossenkopf, V., Hogerheijde, M. R., Juvela, M., Wiesemeyer, H., & Schöier, F. L. 2002: *Numerical methods for non-LTE line radiative transfer: Performance and convergence characteristics*, A&A, 395, 373
- Voshchinnikov, N. V. & Das, H. K. 2008: *Modelling interstellar extinction and polarization with spheroidal grains*, J. Quant. Spectrosc. Radiat. Transfer, 109, 1527
- Walch, S., Girichidis, P., Naab, T., Gatto, A., Glover, S. C. O., Wunsch, R., Klessen, R. S., Clark, P. C., Peters, T., Derigs, D., & Baczynski, C. 2015: *The SILCC (Simulating the LifeCycle of molecular Clouds) project - I. Chemical evolution of the supernova-driven ISM*, MNRAS, 454, 238
- Weingartner, J. C. & Draine, B. T. 2000: *Dust Grain Size Distributions and Extinction in the Milky Way, LMC, and SMC*, in Bulletin of the American Astronomical Society, Vol. 32, American Astronomical Society Meeting Abstracts, 1466
- Weingartner, J. C. & Draine, B. T. 2003: *Radiative Torques on Interstellar Grains. III. Dynamics with Thermal Relaxation*, ApJ, 589, 289
- Whitney, B. A. 2011: *Monte Carlo radiative transfer*, Bulletin of the Astronomical Society of India, 39, 101
- Whitney, B. A. & Wolff, M. J. 2002: *Scattering and Absorption by Aligned Grains in Circumstellar Environments*, Apj, 574, 205
- Wolf, S. 2003: *MC3D-3D continuum radiative transfer, Version 2*, CPC, 150, 99
- Wolf, S., Henning, T., & Stecklum, B. 1999: *Multidimensional self-consistent radiative transfer simulations based on the Monte-Carlo method*, A&A, 349, 839
- Wolf, S. & Voshchinnikov, N. V. 2004: *Mie scattering by ensembles of particles with very large size parameters*, Computer Physics Communications, 162, 113
- Yun, J. L. & Clemens, D. P. 1990: *Star formation in small globules - Bart BOK was correct*, ApJ, 365, L73

- Yusef-Zadeh, F., Morris, M., & White, R. L. 1984: *Bipolar reflection nebulae - Monte Carlo simulations*, ApJ, 278, 186
- Zubko, V. G., Krelowski, J., & Wegner, W. 1998: *The size distribution of dust grains in single clouds. II - The analysis of extinction using inhomogeneous grains*, MNRAS, 294, 548

Acknowledgments

This thesis would not have been possible without the support and contributions of colleagues, friends, and my family.

Especially, I would like to thank Prof. Dr. Sebastian Wolf. His supervision, useful discussions, and permanent support helped to improve not just my thesis but also my skills and knowledge immensely. Thanks to Gesa Bertrand for her guidance during my starting time at the CAU. We also wish to thank the colleagues Daniel Seifried for providing MHD data, Florian Kirchschrager and Robert Brauer for assistance with DDSCAT and the dust grain database, Jan Philipp Ruge and Gesa Bertrang for fruitful discussions about disk models and grain alignment, Florian Ober and Peter Scicluna for their contributions to radiative transfer concepts and dust heating algorithms. We also wish to thank the students Yong Kyung OH and Jan Thiel to serve as code testers.

Special thanks goes to Alexander Schmidt for his permanent encouragement and proofreading of my thesis. Finally, I thank the DFG under contract *WO 857/11-1*.

Curriculum Vitae

Name: Stefan Reißl
Born: 25.07.1981, Garmisch-Partenkirchen
Marital Status: single
Citizenship: german

Education

1998 - 2002	Apprenticeship as Television engineer, Garmisch Partenkirchen - Certificate of apprenticeship
2003 - 2005	Upper vocational schools (BOS Technik, Munich) - General qualification for university entrance
2005 - 2007	Technische Universität München - Intermediate diploma in Physics
2007 - 2011	Ludwig-Maximilian University (LMU), Munich - Diploma in Physics, Exam focus: Astrophysics and Plasma physics - Diploma Thesis: „Modeling the Andromeda Galaxy in 3D with dust component“
2012 - 2015	Ph.D. Student, Institute of Theoretical Physics and Astrophysics (ITAP) of Kiel University Workgroup „Star and Planet Formation“

Erklärung

Hiermit erkläre ich, dass ich diese Dissertation unter Anleitung von Prof. Dr. Sebastian Wolf und, sofern nicht ausdrücklich anders gekennzeichnet, selbstständig erstellt habe. Sie wurde unter Einhaltung der Regeln guter wissenschaftlicher Praxis und Verfahrensweisen der Deutschen Forschungsgesellschaft erstellt. Diese Dissertation wurde noch nicht im Rahmen eines Dissertationsverfahrens vorgelegt. Teile dieser Arbeit wurden in *Astronomy & Astrophysics* eingereicht und zur Veröffentlichung akzeptiert unter: Reissl *et al.* (2014).

Kiel, Januar 2016

Stefan Reißl